A unified seismicity catalogue for the Sea of Marmara Region, Turkey, and subsequent studies regarding repeating earthquakes and the local stress field

Dissertation

zur Erlangung des akademischen Grades

Dr. rer. nat.
im Fach Geophysik

vorgelegt am
Fachbereich Geowissenschaften
der
Freien Universität Berlin

von
Dipl. Phys. Christopher Wollin

Berlin, den 11.11.2018

Eidesstattliche Erklärung:

Ich erkläre hiermit an Eides statt, dass ich die vorliegende Dissertation selbstständig und nur unter Verwendung der angegebenen Quellen und Hilfsmittel angefertigt habe.

Berlin, den 11.11.2018

Referent:	Prof. Dr. Marco Bohnhoff
Korefrerent:	Prof. Dr. Frederik Tilmann

Tag der Disputation: 14.02.2019

Freie Universität Berlin
Fachbereich Geowissenschaften
Intitut für Geologische Wissenschaften
Malteserstr. 74 – 100
12249 Berlin

Abstract

The North Anatolian Fault Zone (NAFZ) in the Sea of Marmara, Turkey, is likely to host a major earthquake (magnitude $M > 7$) in the coming decades. This exposes one of Europe's largest metropolitan areas, Istanbul, to substantial risk. The thesis at hand contributes to the description of the seismotectonic setting in the area, a prerequisite for a comprehensive seismic hazard assessment.

As the extended water body in the area has inhibited continuous seismic near-fault recordings, this long term study covering a decade of seismic activity (2006–2016) aggregates different land based, permanent seismic networks for joint analysis including the two largest, national seismic networks. With such optimized azimuthal coverage and a consistent waveform-processing scheme, a refined earthquake catalogue with 6812 hypocentre locations is obtained. The development and regional adjustment of the involved automatized timing (picking) and iterative inversion of seismic P- and S-wave onsets are explained in detail. Newly calculated moment magnitudes indicate completeness down to $M_c = 2.1$. As part of this thesis, the new catalogue serves as input for a search of highly similar earthquakes (repeaters) and a segmented investigation of the stress field where waveform cross-correlation and direct inversion of first-motion polarities are the employed methods, respectively.

The earthquake distribution distinguishes the northern branch of the NAFZ as the more active fault strand and spares several aseismic patches there. The latter are interpreted as locked fault segments where their contours are further sharpened by a catalogue of 4407 relatively relocated earthquakes. Repeating earthquakes in the western half of the Sea of Marmara indicate that the fault segments there accommodate the far-field deformation by partial creep. For the same fault segment the stress-field inversion indicates a normal faulting regime.

Adjacent, in the east and west offshore the Ganos Mountains and the Princes' Islands, respectively, it is framed by strike-slip regimes. This spatial variation of the orientation of the largest and intermediate principal stresses as well as most of the newly calculated single focal mechanisms are in agreement with large scale transtension. It is found for other seismically active areas off the northern fault branch too and it is characterized by a least compressive principal stress that has almost constant N35°E trend on average and a subhorizontal plunge.

The transtensional setting with a combination of normal and strike-slip stress regimes implies that both faulting types could be involved during the expected major earthquake. Its nucleation seems more likely within locked fault patches and less likely at segments displaying creep. As the latter are situated on the farer end of the fault zone, the hazard from a rupture directed towards Istanbul is relaxed.

Zusammenfassung

Die Nordanatolische Verwerfungszone auf Höhe des Marmarameeres in der Türkei wird in den kommenden Jahrzehnten mit großer Wahrscheinlichkeit ein Starkbeben ($M > 7$) generieren. Dies stellt ein erhebliches Risiko für die Region Istanbul als eines der größten und dichtesten Siedlungsgebiete Europas dar. Die hier vorgelegte Doktorarbeit ist ein Beitrag zur Beschreibung der regionalen Seismotektonik, welche unerlässlich für eine umfassende Bewertung der seismischen Gefährdung ist.

Da der ausgedehnte Wasserkörper des Marmarameeres im Untersuchungsgebiet keine kontinuierlichen seismischen Aufzeichnungen nahe der Verwerfung ermöglicht, vereint diese Langzeitstudie (2006–2016) verschiedene landgestützte, permanent aufzeichnende seismische Netzwerke zur einheitlichen Auswertung, einschließlich der beiden größten nationalen Netzwerke. Mit dieser optimierten azimutalen Abdeckung sowie einer konsistenten Verarbeitung der Wellenformen wurde ein vereinheitlichter Erdbebenkatalog mit 6812 Hypozentren erstellt. Die Entwicklung und Einstellung der Computeralgorithmen zur automatisierten Bestimmung und iterativen Inversion von Ankunftszeiten der aufgezeichneten P- und S-Wellen werden im Detail beschrieben. Neu berechnete Momenten-Magnituden ergeben eine Vollständigkeit des Katalogs bis $M_c = 2.1$. Der neue Katalog wurde als Grundlage für zwei weitere Studien im Rahmen dieser Doktorarbeit herangezogen, welche Sequenzen von hoch ähnlichen Erdbeben und die segmentierte Auflösung des Spannungsfeldes untersuchen. Dabei dienten die Kreuzkorrelation von Wellenformen und die direkte Inversion von Erstausschlägen als methodische Werkzeuge.

Die Verteilung der Erdbeben zeichnet den nördlichen Ast der Nordanalotlischen Verwerfungszone als den aktiveren aus, wobei mehrere aseismische Bereiche hervortreten. Letztere werden als verhakte Verwerfungssegmente interpretiert wobei ihre Kontur durch einen Katalog von 4407 relativ relokalisierten Erdbeben geschärft wird. Sequenzen von hochähnlichen Erdbeben in der westlichen Hälfte des Verwerfungsastes deuten daraufhin, dass die Fernfelddeformation an dieser Stelle durch partielle Kriechbewegung verarbeitet wird. Für dieses Verwerfungssegment zeigt eine Spannungsfeldinversion ein Abschiebungsregime auf.

Die angrenzenden Segmente im Osten und Westen, seewärts des Ganosgebirges und vor den Prinzeninseln, sind durch Blattverschiebungsregime gekennzeichnet. Sowohl diese räumliche Variation der Orientierung der größten und mittleren Hauptspannungen als auch die neu berechneten Herdflächenmechanismen einzelner Erdbeben anderseits stimmen mit einem großflächig transtensiven Spannungsfeld überein. Dieses wird auch in anderen seismisch aktiven Bereichen abseits des nördlichen Verwerfungsastes nachgewiesen und ist durch die kleinste Hauptspannung charakterisiert, welche für alle Segmente fast konstant nach N35°E streicht und fast horizontal einfällt.

Die für die Region charakteristische transtensive Krustenspannung mit benach-

barten Abschiebungs- und Blattverschiebungsregimen impliziert, dass beide Typen von Bruchmechanismen bei dem überfälligen Starkbeben eine Rolle spielen könnten. Dessen Risskeimbildung in verhakten Verwerfungsbereichen erscheint wahrscheinlicher als in solchen mit kriechender Deformation. Da letztere am weiter entfernten Ende der Verwerfung zu finden sind, verringert dies die Gefahr einer Rissausbreitung in Richtung Istanbul.

Publications forming parts of this thesis

1. M. Bohnhoff, **C. Wollin**, D. Domigall, L. Küperkoch, P. Martínez-Garzón, G. Kwiatek, G. Dresen and P. E. Malin (2017a); Repeating Marmara Sea earthquakes: indication for fault creep, In: *Geophysical Journal International*, Volume 210, Issue 1, Pages 332–339, https://doi.org/10.1093/gji/ggx169

2. **C. Wollin**, M. Bohnhoff, P. Martínez-Garzón, L. Küperkoch and C. Raub (2018a). "A Unified Earthquake Catalogue for the Sea of armara Region, Turkey, Based on Automatized Phase Picking and Travel-Time Inversion: Seismotectonic Implications". In: *Tectonophysics*. https://doi.org/10.1016/j.tecto.2018.05.020

3. **C. Wollin**, M. Bohnhoff, V. Vavryčuk and P. Martínez-Garzón (2018b). "Stress Inversion of Regional Seismicity in the Sea of Marmara Region, Turkey". In: *Pure and Applied Geophysics*. https://doi.org/10.1007/s00024-018-1971-1

Contributions of the author(s) In publication 1) (Bohnhoff et al. 2017a) I, the author of this thesis, provided the earthquake catalogue as well as the phase picks on whose basis earthquakes and waveform portions were selected for cross-correlation. I also supervised Dorina Domigal on methodological accounts. The core MATLAB®-scripts used to perform the waveform cross-correlation and to create the figures were programmed by me. I also contributed to the writing of the manuscript.

In publication 2) and 3), (Wollin et al. 2018a,b) I functioned as main author and as such sectioned and wrote major parts of the manuscript as well as merged all of the written contributions of my co-authors. The interpretation of the results was a collaborative effort where Marco Bohnhoff served as main supervisor. In both publications, I produced all of the figures. In publication 2) (Wollin et al. 2018a) my main contributions were the automatic determination of the seismic phase onsets, the absolute earthquake hypocentres and the focal mechanisms. Patricia Martínez-Garzón performed the relative relocation of absolute hypocentre locations, Christina Raub calculated the moment magnitudes and Ludger Küperkoch supervised the initial application of his automatic picking algorithm as well as the manual reference picking. In publication 3), Václav Vavryčuk conceptualized the calculation of a synthetic first-motion polarity distribution.

I prepared all Figures in the three publications using the Generic Mapping Tool (GMT) (Wessel et al. 2013) and MATLAB®, except Figures 3 and 4 in Bohnhoff et al. (2017a) which were prepared by Dorina Domigal (corresponding to Figures 5.3, 5.4 and 5.5 in this thesis).

Contents

[a]These chapters/sections are exerpts or contain content from the peer-reviewed publications listed prior to the table of contents.

1. General introduction

. . . if one can describe the whole of humanity's knowledge with an expanding spherical surface.

Prof. Dr. E. Sedlmayr,
Introduction to Astronomy
and Astrophysics

1.1. Preface

During my second field trip to Turkey in the framework of the GONAF project in Yalova, Peter E. Malin compared the installation of a borehole seismometer to the placing of a satellite in Earth's orbit. "If something goes wrong, the instrument is usually lost." His exclamation was certainly provoked by a reflection about the inaccessibility and isolation of certain realms, like the interior of the Earth and outer space. I tried to imagine how far humanity had reached into each of these, i.e. 10 km during the German Continental Deep Drilling Programme (KTB) in one, and 143 astronomical units with *Voyager 1* in the other extreme. Nevertheless, it amazed me that our observational instruments could still see far beyond these modest distances and even grant us some sophisticated knowledge about the composition of "The Origin of the World"[1]. In 1936, Inge Lehmann interpreted recordings of elastic body waves concluding that the Earth's center of mass – the origin of a geocentric coordinate system – is surrounded by a solid core. And on the other hand, the record of an almost isotropic cosmic microwave background indicates that the universe as known today originated from a highly condensed hydrogen plasma. Yet, Peter's exclamation also disillusioned me because it brought home the implausibility that we, i.e. humankind, would ever be able to probe these origins beyond the radiation which they transmit or reflect.

During my third field trip to Turkey earlier this year I tried to explain to Peter my newly confirmed skepticism towards a "Journey to the Center of the Earth"[1] or to "a galaxy far, far away"[1]. While ferrying across the Sea of Marmara from the Princes' Islands to Istanbul, I introduced him to the concept of model solar systems (or "planet paths") which are installed at numerous places to visualize the vast extent of our solar system. In the city of Bonn for instance, a model sun of 1 m diameter positioned near the old parliament building, scales the solar system down to fit it into an extended walk along the river Rhine. I proposed to Peter to scale down Earth to the size of a rubber balloon (that had a diameter equal to the height of this page) and to calculate the corresponding thickness of its crust by rule of proportion.[2] It turned out

[1] Titles to or quotes from pieces of art that are otherwise not related to this work: "Der Ursprung der Welt" by Gustave Courbet or Liv Strömquist, "Journey to the Center of the World" by Jules Verne, "a galaxy far, far away" from *Star Wars, a New Hope*.

[2] The idea to this specific model was laid during my working placement as a teacher at the *Anna-Seghers Oberschule* in Berlin-Adlershof. In the compulsory optional subject *Science and Technology*, the pupils were given the task to design a model solar system (or planet-path) for Berlin: the balloon-sized earth ($\varnothing =\sim 30cm$) travelled on an orbit of ~ 3.44 km radius around the sphere of the TV-tower ($\varnothing =\sim 32m$) at Berlin-Alexanderplatz, thus passing approximately at the height of the Oberbaumbrücke between Berlin Friederichshain and Kreuzberg, for instance. At this scale, the speed of light corresponds to 25 km/h, i.e. a fast bicyclist, and after a 40 year long journey *Voyager 1* would have covered a distance equal to approximately twice the diameter of our solar system and would be reaching my home town in the Rhineland.

that the largest elevations and depressions on the planet would approximately correspond to twice the thickness of this sheet of paper, the average continental crust to approximately the width of a grain of sand, the rupture plane of the 2004 Indian Ocean earthquake to the previous text marker line and the surface extent of the Sea of Marmara to little more than the size of this capital 'S'.

However, the next day I was awed by the sight from the tip of the Armutlu Pensinsula. Between us and the city of Istanbul which could only vaguely be distinguished on the horizon, the Sea of Marmara seemed insurmountable. I was quite pleased with our achievement to locate micro-earthquakes along the North Anatolian Fault under this mass. Their rupture surface approximately corresponds to the size of a soccer field and in my imagination I placed a stadium somewhere half way across the sea – it looked quite small. But it put into perspective the monstrous amount of energy that would be released if the underground should shift by one man's length along a line stretching along my entire field of vision.

1.2. Motivation[a]

Monitoring seismicity along active hazardous faults requires adequate seismic networks to reliably determine the spatial distribution of hypocentres, characterize the fault-zone geometry and subsequently discriminate active from inactive fault strands. Major onshore transform faults such as the San Andreas Fault in California, most parts of the North Anatolian Fault Zone (NAFZ) in Turkey, or the Dead Sea Transform in the Near East provide good preconditions for near-fault monitoring and subsequent hazard and risk estimates for nearby population centres such as e.g. the Los Angeles metropolitan region or the San Francisco bay area. In contrast, the Marmara section of the NAFZ in northwestern Turkey represents a ∼140 km long fault that runs offshore below the Sea of Marmara. The extended water body makes the fault inaccessible for conventional seismographs and the same holds true for geodetic (GPS) or remote sensing campaigns (InSAR). Near-fault observation of seismicity as well as the measurement of the response of the ocean floor to tectonic forcing can only be achieved with ocean bottom equipment which however allows for limited observational time periods only. Permanent seismological observation under low noise conditions is only possible from the shore lines.

There is wide consensus that the Marmara section of the NAFZ is late in its seismic cycle and can be expected to produce a magnitude $M > 7$ earthquake during the next decades, (e.g. Parsons 2004; Bohnhoff et al. 2016b; Murru et al. 2016). This seismic hazard translates into very high risk, because the fault is co-located with the Istanbul metropolitan region with its 15 or more million inhabitants. Consequently, one of the most pressing issues is to image

[a]The first two paragraphs are based on the introduction of Wollin et al. (2018a).

the geometry of the offshore Marmara fault segments and determine their faulting regimes as a prerequisite to improve and optimize hazard and risk assessment for the region. To achieve this, a reliable hypocentre catalogue with lowest possible but regionally consistent magnitude of completeness is needed. However, due to the absence of near-fault stations along the most part of the Marmara section, this is a challenging task and can only be achieved through optimizing both, the azimuthal station coverage throughout the region and the picking accuracy for the arrival times of the different body waves.

Despite the challenge to accurately locate earthquake hypocentres along the offshore segment of the North Anatolian Fault in the Sea of Marmara, a consistent earthquake catalogue allows for the measurement of several geologic parameters otherwise not directly accessible but also crucial for the assessment of the seismic hazard in the region, for instance, the characteristics of the stress field prevailing in earth's crust which is responsible for the activation of the bulk of natural as well as induced seismic events. Stress-field parameters of the crust can only be measured in situ during drilling campaigns which usually sample the crust pointwise penetrating it by to no more than a few kilometres depth (on average ~ 3 km and at the most ~ 10 km for instance during the SAFOD and KTB experiments, respectively, e.g. Brudy et al. 1997; Bohnhoff et al. 2004; Hickman et al. 2004). However, inversion for the stress tensor is possible for any remote and inaccessible volume if it is seismically active (Wallace 1951; Bott 1959; McKenzie 1969; Vavryčuk 2015; Hardebeck et al. 2018) where its knowledge for an area where a major earthquake is expected, may narrow down the types of faulting to anticipate. In the Sea of Marmara, historical tsunamis are documented (Yalçıner et al. 2002) and it is essential to estimate the potential for effective vertical mass movements offshore, as induced by an earthquake with substantial normal faulting components for example. Such would be capable of displacing the water column and thus inducing a subsequent tsunami wave exposing the densely inhabited coastal areas to substantial risk from flooding.

Another important parameter characterizing a fault zone is its rate of deformation in response to the tectonic forcing. Fault segments accommodating the surrounding deformation by partial or full creep are less likely to initiate the rupture process of a major earthquake. In consequence, a rupture directivity away from the creeping segment seems less probable. On land, GPS measurements as well as InSAR campaigns can infer locked or creeping faults where local deformation is or is not in agreement with the far field deformation, respectively (Lisowski et al. 1991; Cakir et al. 2014). As the North Anatolian Fault runs offshore in the Sea of Marmara both methods are of limited accuracy here (Reilinger et al. 2006; Ergintav et al. 2014). Besides the tedious installation of acoustic ranging experiments (Sakic et al. 2016, which in the Sea of Marmara have sampled a comparatively small part part of the fault system so far), micro earthquakes repeatedly activating the same fault patch and thus

radiating a highly similar wave field, have been identified as indicative for fault creep in the seismogenic crust elsewhere (Nadeau et al. 2004). However, an efficient search for similar waveforms of different earthquakes, requires accurately located earthquakes as well as accurately timed seismic phase onsets. For the city of Istanbul, which lies parallel to one third of the unruptured but overdue Marmara segment, directivity effects of the major earthquake expected have substantial impact on the risk assessment as a rupture directed towards the city would imply substantial increase in the peak ground acceleration (Oglesby et al. 2008; Ansal et al. 2009; Spagnuolo et al. 2016).

In the years from 2009 until mids of 2016 two major seismological services maintained separate seismograph networks in Turkey, namely the Disaster and Emergency Management Presidency of Turkey (AFAD) and the Kandilli Observatory and Earthquake Research Institute (KOERI). Both institutions worked independently from one another in analysing the recorded waveforms as well as locating and indexing earthquake locations. Thus, joint (re-)evaluation of the waveforms contains large potential to improve the previous earthquake locations. In order to use these as well as other intermediate results such as seismic phase readings for further studies as outlined above, a unified and consistent processing is even mandatory. However, the dataset to be analysed amounts to over half a million three-component recordings, making manual reprocessing a labour intensive task impossible to realize in the short term.

Although manual inspection of seismograms widely remains the preferred procedure to analyse individual earthquakes (mainly because the generalization capabilities of an experienced analyst are much better), recent studies have shown, that automatic timing of P- and S-phase onsets yield competitive results (e.g. Diehl et al. 2009b; Sippl et al. 2013; Ross et al. 2014). One main advantage of the algorithmic procedure is the possibility to analyse large datasets consistently where the results from a group of individual analysts may statistically differ from one another. In this thesis the approach of Küperkoch et al. (2010, 2012) was adapted who propose an automatic P- and S-phase picking algorithm and successfully apply it to seismograms recorded in the Aegean Sea.

In summary, the aim of this work is to characterize parameters of the seismotectonic setting in the Sea of Marmara region on the basis of automated data analysis. Algorithms are proposed for the analysis of seismic recordings, i.e. the timing of P- and S-phases, and for their iterative travel-time inversion to earthquake hypocentres. A clustering algorithm is used to segment seismicity which is a prerequisite for an effective search for repeating earthquakes as well as for performing a local stress-tensor inversion. The results of this work describe a decade of seismic fault-zone activity and shed light on the properties of different fault segments regarding (1) the absorption of large scale tectonic deformation as well as (2) the underlying stress-field.

1.3. Outline

This thesis is based on three publications placed in peer-reviewed journals, Wollin et al. (2018a,b) and Bohnhoff et al. (2017a). The content of the papers has been adapted to fit joint publication here. Since all three papers apply seismological methods to the same area of study, the Sea of Marmara region, the separate introductions of each paper to the tectonic setting are subsumed in Chapter 2. The most important intermediate result of this study are the timed (or picked) phase onsets of P- and S-waves. They form the basis for the hypocentre determination via travel time inversion and indicate the waveform intervals to be cross-correlated in search of similar waveforms. The first-motion polarity of P-wave onsets is the crucial measurement to determine focal mechanism as well as the local stress field. Chapter 3 describes the methods applied to time (or pick) the phase arrivals as accurate as possible. Apart from a description of the automatic picking algorithm developed in the course of this study, Chapter 3 also includes the algorithm's evaluation against carefully picked manual reference phases. The parameters involved in tuning the picking algorithm are presented in the appendix of the thesis via the comparison of two different applications to regional and local seismicity.

In Chapter 4, two new unified earthquake catalogues are presented, one of absolute and one of relatively relocated hypocentre locations in the Sea of Marmara. Both sets of locations are based on automatically determined P- and S-phase onsets. Together with newly calculated fault mechanism, the catalogues are interpreted with respect to the seismic activity of different fault segments and compared to the previously published catalogue. Chapter 5 and 6 build upon these results and present the observation of repeating earthquakes in the western Marmara segment and a stress-field inversion of different seismic activity spots of local scale, respectively. As the study regarding the repeating earthquakes (Bohnhoff et al. 2017a) was based on a preliminary version of the new and consistent earthquake catalogue (spanning four years from 2006–2010 only), the original paper also contained methodological accounts on the picking procedure. These were dropped in this thesis in order to obtain a continuous narration. Instead, results were amended from the search for repeating earthquakes which was extended to the entire time interval that is covered by the new earthquake catalogue (2006–2016). Chapter 7 jointly summarizes the results of the three publications, relates them to work of other authors which was published most recently or not consulted so far. Finally, an outlook for possible subsequent research is given.

2. Tectonic Setting and Data[a]

> In St. Jago, the capital of the kingdom of Chili, at the moment of the great earthquake of 1647 in which many thousands lost their lives, a young Spaniard called Jerónimo Rugera was standing beside one of the pillars in the prison to which he had been committed on a criminal charge, and was about to hang himself. . . .
>
> *The Earthquake in Chili*, Heinrich von Kleist (1807)

[a] The here presented introduction into the geographic area of study and its seismotectonic setting was combined from the corresponding introductions of two research articles (Wollin et al. 2018a,b).

2.1. The North Anatolian Fault Zone (NAFZ) in the Istanbul-Marmara region

The NAFZ is one of the largest plate-bounding transform faults on Earth and its regional seismotectonic setting was extensively studied since it was first reported in the late 1940s (Ketin 1948). The fault zone separates the Anatolian and Eurasian plates extending for approximately 1200 km between the Karliova triple junction in Eastern Anatolia and the Gulf of Saros Northern Aegean (e.g. Barka 1992; Şengör et al. 2005; Bohnhoff et al. 2016b). Westward movement of Anatolia has developed in the framework of the northward moving Arabian plate (Reilinger et al. 2006; Bulut et al. 2012). It is also connected to the southward rollback of the Hellenic subduction zone, where the African lithosphere is subducted below the Aegean (Flerit et al. 2004; Bohnhoff et al. 2005). The NAFZ generally exhibits a right-lateral strike-slip fault over most of its extent. Except for the Ganos bend (Janssen et al. 2009), no substantial thrust components have been identified from focal mechanisms of larger earthquakes during the 20th century. The average slip rate along the NAFZ as determined from GPS is 20–25 mm/yr with increasing values towards the west (Reilinger et al. 2006). The pure strike-slip system along the bulk of the NAFZ east of the Sea of Marmara turns into a transtensional setting in NW Turkey due to the rollback of the Hellenic subduction zone that started a few million years ago and that resulted in the opening of the Sea of Marmara as a large pull-apart structure (Şengör et al. 2005; Le Pichon et al. 2015). This transtensional system still evolves and is currently further progressing towards the east resulting in the younger and thus smaller pull-apart structures at the eastern tip of the Sea of Marmara (Cinarcik Basin) (Le Pichon et al. 2001; Karabulut et al. 2002; Acarel et al. 2014) and further inland along the 1999 Izmit rupture (Akyazi Plain) (Bohnhoff et al. 2006; Bulut et al. 2007b; Najdahmadi et al. 2016).

The NAFZ forms a single main fault strand along most of its part from eastern Anatolia to the Bolu region. Approximately 150 km east of the city of Izmit the fault splits into two major branches known as the northern and southern NAFZ strands in northwestern Turkey (Le Pichon et al. 2014). Most of the NAFZ deformation in northwestern Turkey occurs along the northern fault strand below the Sea of Marmara, here named ‘Marmara Section’ (Reilinger et al. 2006; Hergert et al. 2010; Ergintav et al. 2014) (Fig. 2.1).

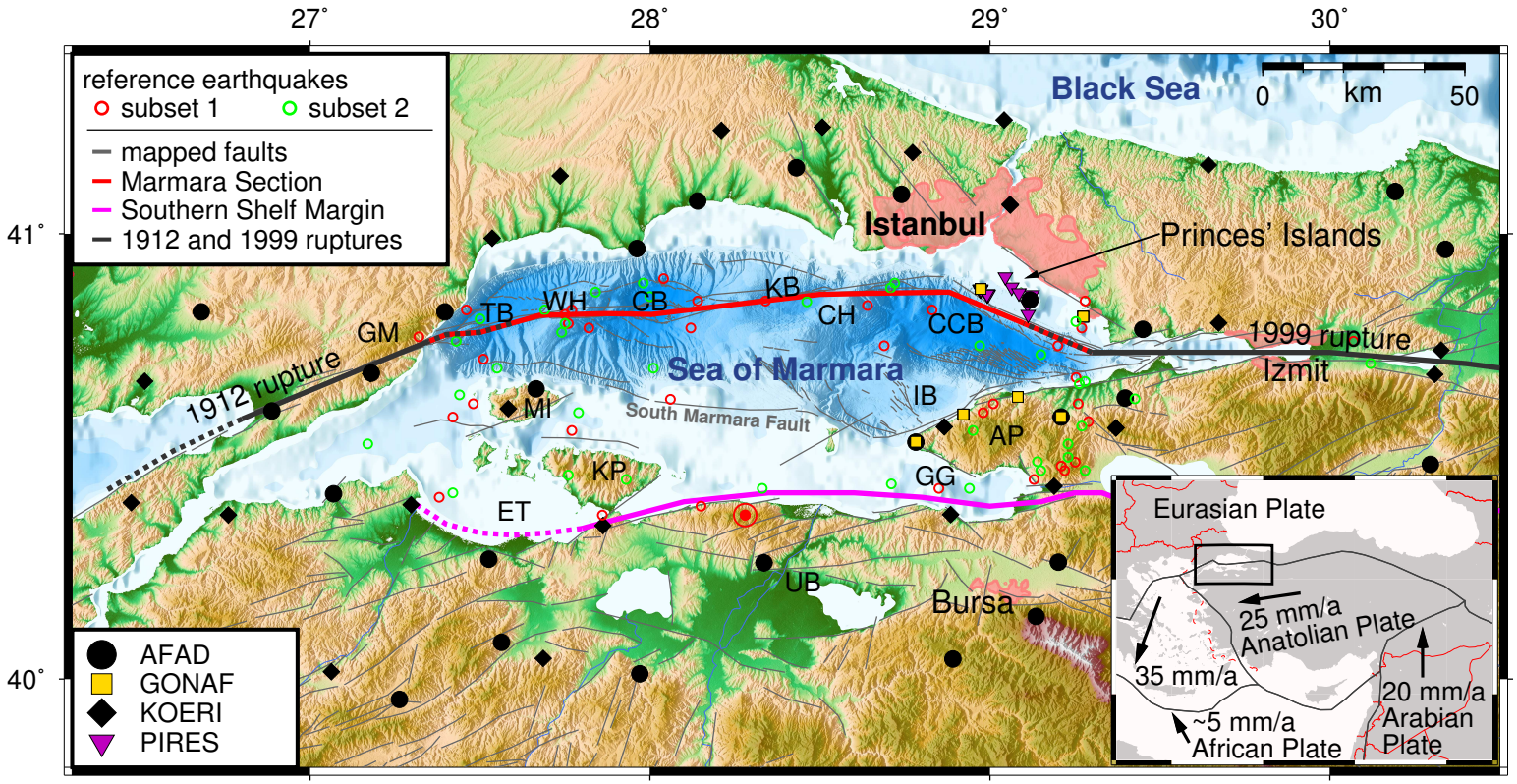

Figure 2.1.: The caption is on the next page.

Figure 2.1.: The North Anatolian Fault Zone (NAFZ) around the Sea of Marmara region. The 1912 Ganos and 1999 Izmit earthquake ruptures are indicated by the thick grey lines. The NAFZ is highlighted in red. The Southern Shelf Margin (Armijo et al. 1999; Murru et al. 2016) is delineated in magenta. Abbreviations in capital letters name some common topographic features: Tekirdağ Basin (TB), Western High (WH), Central Basin (CB), Central High (CH), Kumburgaz Basin (KB), Çınarcık Basin (CCB), Imrali Basin (NIB), Armutlu Peninsula (AP) all after Bécel et al. (2009), Gulf of Gemlik (GG), Kapıdağ Peninsula (KP), Erdek Tombolo (ET), Marmara Island (MI), Ganos Mountains (GM) all after Şengör et al. (2014), Uluabat Basin (UB) after Le Pichon et al. (2014). Seismic stations of permanent seismic networks used in this study are indicated by different symbols. The bathymetry and submarine faults are after Le Pichon et al. (2001) and Armijo et al. (2005) and onshore faults are after the Turkey General Directorate of Mineral Research and Exploration (pers. comm.). Larger cities (Istanbul, Izmit, Bursa) are plotted as pink areas. Red and green circles mark the epicentres of two subsets of earthquakes for which onset times of crustal phases were manually determined (see Section 3.3 for details). The bold red circle located on the southern coastline marks the event whose waveform recordings are shown in Fig. 3.7. The inset in the lower right shows the area of study in the broader tectonic regime with respect to stable Eurasia.

In the historic past, the Marmara Section of the NAFZ created dominantly strike-slip but also $M > 6$ normal faulting earthquakes such as the 1963 earthquake below the eastern Sea of Marmara (Bulut et al. 2007b). The offshore Marmara section is bound by the two most recent magnitude $M > 7$ earthquakes of the region, the 1912 Mürefte-Ganos event in the west (Ambraseys 1970; Janssen et al. 2009) and the 1999 Izmit and Düzce events in the east (Pinar et al. 2001; Tibi et al. 2001; Barka et al. 2002; Bohnhoff et al. 2016a) (Fig. 2.1). The Marmara Section last ruptured in 1766 with a M7.4 event. The estimated recurrence time for this event is 200–250 years (Parsons 2004; Bohnhoff et al. 2016b) indicating that this fault is currently in the final phase of its seismic cycle and thus needs to be considered as a seismic gap posing a major threat to the Istanbul metropolitan region. The southern NAFZ strand hosts only 20 % of Anatolia's westward motion (e.g. Ergintav et al. 2014). It is located in the southern Sea of Marmara shelf (Armijo et al. 1999; Le Pichon et al. 2001) and bypasses the Sea of Marmara to its south, south of the Uluabat Basins, bending SW thereafter before entering the Aegan Sea (Armijo et al. 1999; Le Pichon et al. 2014) (Fig. 2.1). It is of "fragmented" nature (Şengör et al. 1985; Le Pichon et al. 2003, 2014) and displays transtensional structures south of the Sea of Marmara.

While there is consensus on the potential for a larger (M up to 7.4) event in this region, there is an ongoing discussion on the dominant type of faulting to be expected. The two end-members discussed in the literature are the activa-

tion of a single through-going strike-slip fault (the so-called "Main Marmara Fault") (Le Pichon et al. 1999, 2001) versus the activation of several smaller en-echelon normal faults (Armijo et al. 2002, 2005). While the "Main Marmara Fault" model predicts a single strike-slip event with a larger magnitude of up to 7.4 and subsequent implications for intense ground-shaking, the normal faulting events would probably not exceed M∼7 but host the potential for local tsunamis. Pinar et al. (2003) summarized several other models for a variety of fault systems in the Sea of Marmara including the two above-mentioned end-members. The authors themselves proposed that the main fault between the two most recent major ruptures in 1912 and 1999, should be decomposed into three throughgoing right-lateral subsegments which are linked by right and left stepovers and numerous subsidiary faults.

Between the northern and southern NAFZ branches, two other secondary fault strands have been identified. The first of these follows the southern coast of the Sea of Marmara coinciding with the "Southern Shelf Margin" (Armijo et al. 1999) and it was named the "Central North Anatolian Fault" by Murru et al. (2016) (Fig. 2.1). Faults in this structure have been mostly attributed to normal faulting-type seismicity (Le Pichon et al. 2001). Additionally, Le Pichon et al. (2014) delineated a deformation zone between Marmara Island and the Armutlu Peninsula (Fig. 2.1) named the "South Marmara Fault". This structure strikes WNW forming a wide arc bypassing Marmara Island and then continuing further westward sub-parallel to the Ganos fault. The fault was characterized as right-lateral strike-slip and the end of its activity was dated to 5 Ma ago when motion of the Anatolian plate started to be predominantly accommodated by the northern branch (Le Pichon et al. 2014).

First information on the stress field orientation in the broader Marmara region was provided by Kiratzi (2002) who inverted focal mechanisms of twelve large regional earthquakes recorded during the second half of the 20^{th} century, most of which occurred on the mainland surrounding the Sea of Marmara. The results show a first-order strike-slip stress field with an oblique component. The largest horizontal stress (S_{Hmax}) has a WNW–ESE orientation and a transpressional signature. However, also $M > 6$ normal faulting earthquakes such as the 1963 Armutlu earthquake below the eastern Sea of Marmara are well documented (Bulut et al. 2007a). Örgülü (2011) used a refined data set of numerous smaller events and showed that a strike-slip regime can be separated from a normal-faulting regime in the eastern Marmara region between the Princes' Islands Segment in the north and the neighbouring Armutlu Peninsula in the south (see Fig. 2.1 for location). This transition is accompanied by a rotation of S_{Hmax} from NW-SE to WNW-ESE and correlates well with the results for the fast polarization direction obtained from the shear-wave-splitting analysis (Eken et al. 2013). Here the polarization is sub-parallel to the maximum shortening direction at seismic stations in the Princes' Islands and rather diffuse for those in the Armutlu Peninsula. Similar stress orientations were found by

Pinar et al. (2003) who document a pure strike-slip regime with an intermediate shape ratio $R = 0.5$ for the entire eastern Sea of Marmara, where the overlap of the confidence areas of the smallest and the intermediate principal stresses, σ_2 and σ_3, indicate a transpressional stress regime. This is in contrast to the results of Örgülü (2011), who document an overlap of the confidence areas of the largest principal stresses, σ_1 and σ_2, thus indicating transtension. At the westernmost tip of the Princes' Islands Segment, Armijo et al. (2002) report on en-echelon normal fault scarps apparently produced by composite normal and strike-slip faulting. In the northern Armutlu Peninsula, normal-faulting with a more pronounced strike-slip component at the south is confirmed by Kinscher et al. (2013). For the Princes' Islands Segment, Armutlu Peninsula and the Gulf of Gemlik areas, Öztürk et al. (2015) find a normal-faulting stress regime and a rotation of the minimum horizontal stress S_{Hmin} from SW-NE to SSW-NNE, along a trajectory from north to south. Interestingly, several reverse mechanisms are reported further west. Strike-slip and normal faulting events generally dominate the offshore segment below the NAFZ, which evidently lacks near-fault observations (Pinar et al. 2003; Örgülü 2011; Wollin et al. 2018a). Below the western Sea of Marmara, where the Marmara Section changes strike from E-W to ESE-WNW at the Ganos-Bend, a transpressional stress regime (Armijo et al. 1999, 2002; Pinar et al. 2003; Janssen et al. 2009; Örgülü 2011) or strike slip Öztürk et al. (2015) is reported in the literature.

In the Sea of Marmara the pull-apart characteristics and the ongoing basin formation have also left their imprint on the crust-mantel boundary. A wide-angle seismic profile across the Sea of Marmara (Bécel et al. 2009) revealed the thinning of the upper crustal part beneath the North Marmara Trough which caused an up-warp of the lower crustal layers. This tectonic feature is also characterized by a 120 km wide plateau of a shallow Mohorovičić discontinuity (Moho) at ∼26 km depth which stretches between the Tekirdağ and the Çınarcık Basin in the West and East, respectively. Beyond this interval the Moho sharply gains depth by approximately 10 km. Towards the south the crust thickens more gradually.

2.2. A unified Marmara seismic network

Due to the geologic setting of the Marmara region, with the largest portion of the Marmara Section being located below the seabed between 10 and 30 km offshore the northern and up to 50 km away from the southern coast, permanent or long-term high-precision seismic monitoring is mostly constrained to the deployment of land-based seismometers at substantial distance to the fault. This generally limits the resolution capability, especially for precisely determining the absolute hypocentral depth and subsequently also for accurate single-event focal mechanisms due to the absence of near-fault stations. Deploying ocean-bottom seismometers to densely sample the entire focal sphere is

an alternative approach, but their long-term operation remains a difficult task and signal quality is usually limited due to coupling issues and enhanced noise levels on the seabed (Sato et al. 2004; Bulut et al. 2009; Schmittbuhl et al. 2015; Yamamoto et al. 2017). The only near-fault on-land spots are located in the eastern Sea of Marmara, where the Princes' Islands and selected onshore spots were recently equipped with permanent stations including surface and downhole vertical arrays (Bulut et al. 2009, 2011; Bohnhoff et al. 2013, 2017a,b).

Consequently, the best way to achieve a homogeneous seismicity catalogue in this region is as follows: (1) optimizing the azimuthal station coverage by combining stations from the different permanent regional networks; (2) reducing location uncertainties by applying optimized identification and timing of P- and S-wave arrival times; and (3) applying strict quality criteria and station corrections prior to travel time inversion for hypocentre determination in the absence of a high-resolution 3-D velocity model. Point (2) includes a unified processing of seismic waveforms aiming at assuring consistency among the arrival times.

On the land surrounding the Sea of Marmara, two regional permanent seismic networks are in operation. The Disaster and Emergency Management Presidency of Turkey (AFAD) and the Kandilli Observatory and Earthquake Research Institute (KOERI) operate two extensive but separate permanent networks of seismic stations throughout Turkey with higher station density in the broader Marmara region. For the first time, waveform recordings from both national networks were here combined to a single virtual regional seismic network with unprecedented station coverage along the entire Marmara section of the NAFZ (Fig. 2.1). We focused our study on the time period spanning from beginning of 2006 to mid-2016 thus comprising almost $10\,\frac{1}{2}$ years. We also included near-fault recordings from the Princes' Islands Realtime Earthquake monitoring System (PIRES) network and the Geophysical (borehole) Observatory at the North Anatolian Fault (GONAF) which started operation in 2006 and 2015, respectively (Bulut et al. 2009, 2011; Bohnhoff et al. 2013; Prevedel et al. 2015; Raub et al. 2016; Bohnhoff et al. 2017b) (Fig. 2.1). Incorporating further waveform data from additional temporary seismological deployments such as short-term local land-based networks or individual ocean bottom seismometers can only increase catalogue precision for a limited sub-region and time period. Thus, it does not substantially contribute to a regionally decreased magnitude of completeness for the entire Marmara region and the entire time period considered here.

The bulk of seismic recordings used in this study were provided by KOERI, from which we selected a total of 39 stations. Between 2006 and 2013, most KOERI waveform recordings were sampled with 50 Hz. After 2013, the sampling rate was doubled to 100 Hz. From AFAD, digital recordings were available from 29 stations from 2009 onwards. Their waveform data was consis-

tently sampled at 100 Hz. Furthermore, the recordings from 16 PIRES stations were sampled at 200 Hz covering the entire considered time period between 2006 and 2016. Lastly, GONAF recordings from six boreholes sampled at 500 Hz were available from 2015 onwards. All station locations are shown in (Fig. 2.1).

2.3. Merged seismicity catalogues for the Marmara region in the years 2006–2016

We based our study on the seismicity catalogues provided by KOERI, AFAD and PIRES, which were merged into a single catalogue containing event origin time and hypocentral coordinates. Locations of the different catalogues were calculated on the basis of different velocity models. Whereas KOERI and PIRES use velocity models derived for the eastern Sea of Marmara (Karabulut et al. 2002; Bulut et al. 2009, respectively), AFAD locations are determined with one standard velocity model throughout Turkey. The individual catalogues provide different magnitude scales (predominantly durational and local magnitudes). We also compared the resulting list of events with the seismicity catalogue provided by MARsite (`www.marsite.eu`) to ensure that no event located anywhere along the entire Marmara section of the NAFZ during the considered period of time was missing. Duplicated earthquakes were removed, by applying a density based clustering analysis to the origin times (DBSCAN, Ester et al. 1996). Clusters of origin times were defined for pairs separated by less than 30 s. By keeping all earthquakes with unclustered origin times and the earliest occurrence within clusters, we obtained a total number of 12,186 events.

3. Timing (picking) of seismic phases of regional earthquakes[a]

> "Coco, it is important what you play, but much more important is what you don't play!"
>
> Hans Korsek
> to Coco Schumann (1997)
> some time in the 1930ies

[a] Large parts of this chapter have been published in Wollin et al. (2018a). Here we added some details that fell short in the publication.

3.1. Introduction

In order to locate the earthquake hypocentres and their origin times, the timing of P- and S-phase onsets (picking) remains a standard approach and a pre-requisite to date. We analysed ∼580,000 three-component recordings (47 per event on average) from 86 permanent stations in the Sea of Marmara (also see Sec. 2.2) for a 10-year time period where the waveforms were cut to a time interval of 240 s (1 min before to 3 min after the origin time given in the merged catalogues) thereby ensuring to include full body wave trains and their coda even for stations up to ∼200 km epicentral distance. In total we retrieve ∼360,000 P- and S-picks. The here applied automatic picking procedure, i.e. the procedure for timing P- and S-wave onsets, is essential for the derived quality of the hypocentre catalogue (see Chapter 4) and therefore the applied methodology is described in detail in this chapter. The automatic picking procedure primarily serves the purpose to ensure consistency among the seismic arrival times which are the most important intermediate results for a study of regional seismicity as done here. This is relevant because otherwise, the consistency of phase data acquired from independently operating data centres or researchers cannot be presumed. After an introduction into peculiarities of seismic travel times at regional distances, this chapter summarizes the procedure of manual reference picking. This is followed by a description of enhancements to the automatic picking algorithm presented by Küperkoch et al. (2010, 2012). Preliminary and final results for the timed P- and S-phase arrivals which were obtained with the former and the improved picking algorithm are discussed with respect to the reference picks.

3.2. Seismic phases at regional distances

The sudden displacement of rock mass as it occurs during the rupture of critically stressed crust in Earth, produces elastic waves which may propagate through the entire volume of the planet. Long-period waves as emitted by moderate and larger earthquakes ($M > 5$) are detectable at teleseismic distances, i.e. several hundreds to thousands of kilometres away from the source. With a dominant frequency of less than 1/10 Hz and an average propagation velocity of ∼10 km/s their waves are predominantly affected by velocity contrasts effective over several tens of kilometres. Minor earthquakes of magnitude $M < 3$ are composed of higher frequencies and their wave field is sensitive to a smaller scale of velocity heterogeneities. The already smaller amplitudes will also be attenuated much faster such that minor and micro earthquakes can only be detected regionally if only locally, i.e. across some dozens of kilometres.

The average magnitude of earthquakes detected in the Sea of Marmara is $M \sim 2$. However, the seismicity there frequently reaches magnitudes which make it detectable throughout the region. The travel paths of the seismic

waves laterally cover an area extending approximately 150 km from North to South and 250 km from East to West and thus penetrate a prominent velocity discontinuity between the boundary between the Earth's crust and mantle known as the Mohorovičić discontinuity (Moho). Below continental crust, the Moho has an average depth of 35 km and the velocity increase by almost 15% from the crust to the uppermost mantle produces prominent reflected and refracted waves. Three major crustal and uppermost mantle P-phases and their S-wave pendants are defined (e.g. Shearer 1999):

- Pg waves can be observed at short distances and either travel upwards or bottom within the crust. They originate from sources within the crust.
- Pn waves bottom in the uppermost mantle if emitted by sources in the crust and travel upwards if emitted from within the upper mantle.
- PmP waves are P reflections from the outer side of the Moho.

This slightly differs from the IASPEI standard nomenclature of seismic phases which differentiates between upper and lower crust (Storchak et al. 2003). Here Pb-waves are defined too. They bottom or originate in the lower crust, thus restricting Pg to waves that bottom in the upper crust.

For any seismic source in the crust, the different phase velocities result in a triplication of the travel-time curve, i.e. the travel time of a ray to any point on Earth's surface as a function of epicentral distance. This phenomenon can be illustrated by a simplified model in which the crust-mantle system is described by two spherical layers with two different wave velocities. The wave velocity as a function of depth is displayed in Fig. 3.1a along with the 1st order velocity discontinuity. The resulting travel-time curve with the characteristic caustics is shown in Fig. 3.1c. The first prograde branch corresponds to arrival times of the Pg-phase (black rays and black curve in Fig. 3.1b and c, respectively), i.e. a decreasing take-off angle (from 180° pointing vertically upwards) results in an increasing epicentral distance. PmP (grey in Fig. 3.1c) always arrives later than Pg but its travel-time branch asymptotically approaches that of the Pg-phase. Rays emitted below the critical angle, turn in the second layer. Their arrival times give rise to the second prograde (cyan-coloured travel-time curve in Fig. 3.1c) which tangentially branches off the PmP branch at the critical point, i.e. the point defined by the epicentral distance and travel time corresponding to the critical takeoff angle. The second prograde has a slope corresponding to the propagation velocity of the second earth layer and it is associated with the Pn-wave. Once Pn overtakes the Pg branch at the crossover point, it is also termed head wave.

In the presence of a prominent velocity discontinuity, waves approaching it with an angle smaller than the critical angle, are not only refracted and reflected. Longitudinal are also converted into transversal oscillations and vice versa. Transmission and reflection coefficients of the different types of waves

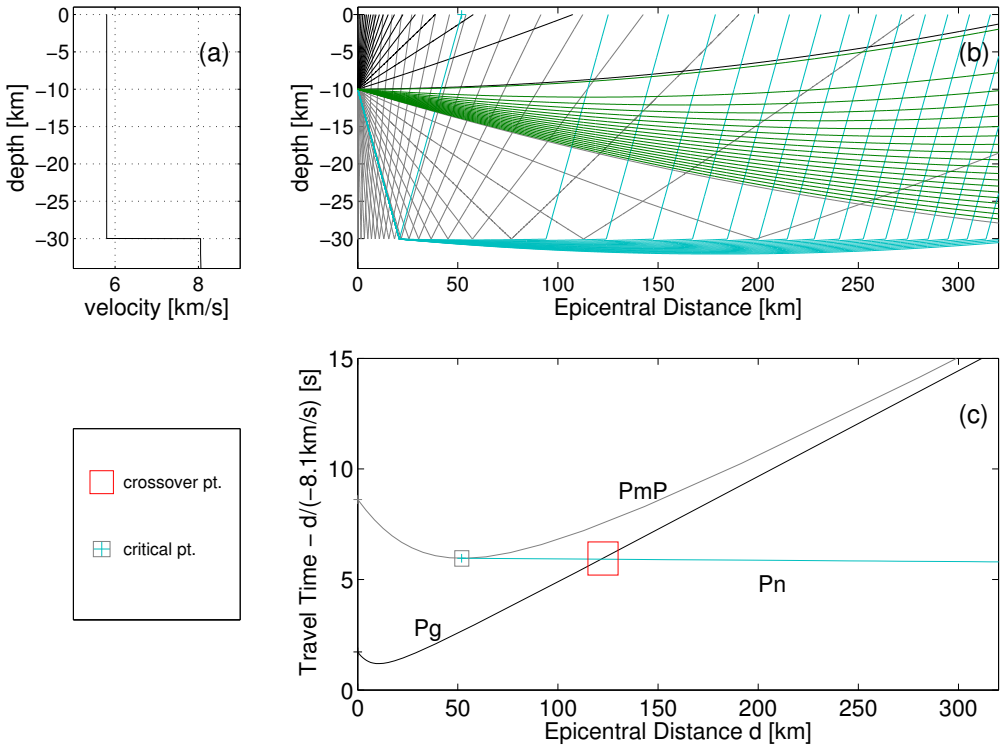

Figure 3.1.: Velocity model a), rays b) and travel time curves c) in a two-layer earth with an illustrative steep velocity gradient at 30 km depth representing the Moho and a seismic event in the upper layer at 10km depth. The travel time branches of the major crustal P-phases are labelled and the cross over and critical point marked by rectangles.

depend not only on the involved propagation velocities but also on the mass densities on both sides of the velocity discontinuity. Their functional dependence from the incidence angle is not monotonous and in the case of S- to P-wave conversion, also depends on the polarization direction relative to the plane of the boundary (Wallace 1951; Shearer 1999; Müller et al. 2007). In regional seismology, the S- to P-wave conversion at the Moho plays a role, since the P-wave propagates faster than the S-wave. Under favourable conditions, i.e. a large transmission coefficient for the conversion from S- to P-wave, the latter will be recorded before the onset of the actual S-phase and thus eventually compromise the timing of the S-wave arrival. However, due to slowing propagation velocities towards the surface, the incidence angles of seismic waves from earthquakes in the seismogenic layers of the crust are usually low. In consequence, the projection of the longitudinal oscillatory motion (of a S- to P-wave conversion before the onset of the actual S-wave) onto the horizontal components is small compared to the amplitude of the actual S-wave.

3.3. Manual reference picking

In order to evaluate and optimize the automatically derived P- and S-wave arrival times, we first defined two subsets of seismic events from the entire hypocentre catalogue. All waveforms for both subsets were then consistently manually picked (P and S). Each subset consisted of 36 events. In order to achieve an even spatial distribution of events throughout the target area (the entire Marmara region), we subdivided it into a regular mesh of rectangles. We then randomly sampled the events in each individual cell without replacement. The number of events drawn per cell is a discrete function of the total count of events in a cell. The function was defined such that relatively few are drawn from cells with many events, thus dampening the probabilistic weight of event clusters. Accordingly, to even out the more frequent occurrence of small events described by the Gutenberg-Richter distribution, large magnitudes were given an increased probabilistic weight, i.e. the probability for an event to be drawn as function of its magnitude remains constant at $\sim 0.05\%$ until a magnitude threshold at $M_{thresh} = 2.6$ and increases linearly from there onwards with ~ 3 percentage points per magnitude until a maximum magnitude of $M_{max} = 5$. The events making up the two subsets are marked in Fig. 2.1 (red and green circles, respectively) and the magnitude frequency distribution of those later successfully located is shown in Fig. 3.2.

Manual reference picking was performed following the strict criteria of Diehl et al. (2009a), identifying an earliest and latest possible, as well as the most likely phase onset time for three different crustal P phases (Pg, Pn, PmP) and their S pendants (also see Sec. 3.2). We also measured the first-motion polarity of all P-phases if possible. Around the cross-over point, the Pn and Pg phases may not be identified unambiguously. In this case, phases were

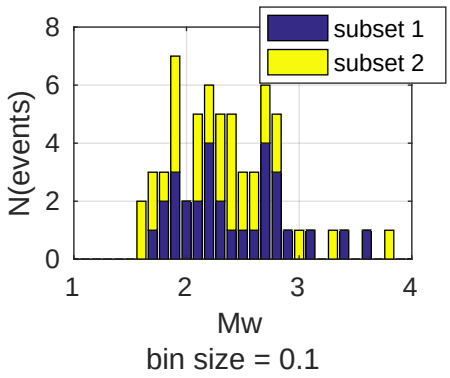

Figure 3.2.: Stacked frequency distributions of moment-magnitudes of two sets of reference events that were manually picked.

labelled in the order of their arrival, e.g. a phase which arrives first with certainty but which is of unknown type will be labelled P1. Phase onsets whose placing in the order of arrival could not be established, were simply labelled with P as proposed by Diehl et al. (2009a). Using previous catalogue locations, the horizontal recordings were transformed from vertical/North/East to vertical/radial/transverse coordinates prior to reference picking.

In order to identify the different crustal phases we calculated their travel time branches with a 1-D ray tracer using two different P-wave velocity models. Bulut et al. (2009) provide an optimized 1-D velocity model for the eastern Sea of Marmara which is roughly congruent with the corresponding sections of an east-west trending wide-angle seismic profile across the Sea of Marmara (Bécel et al. 2009). The significant crustal thinning revealed by the latter study which stretches along the North Marmara Trough at 40°45' N from 27°30' E to 29°E, was adopted in a second 1-D velocity model. The velocity models are compared to each other and to a more recent as well as to a global 1-D velocity model in Fig. 3.3.

For each earthquake, P- and S-wave arrival times of the above-mentioned crustal phases were estimated by plotting a travel-time section based on the event locations of the initial hypocentre catalogue, and travel time branches calculated for both 1-D velocity models. The S-wave travel times were derived from the corresponding P-wave travel times by multiplying the latter by a v_s/v_p ratio of $1/\sqrt{3}$. An example of a seismic section with the travel-time branches of one velocity model is shown in Fig. 3.4. The task of manual reference picking was then accomplished with the 'Picking and Location Tool' (PILOT), a MATLAB® based software developed by (Küperkoch 2011). Here the operand is supported by automatically adapting a time and amplitude window according to the given noise level, thus implementing the suggestions for consistent reference picking (Diehl et al. 2009a).

Only in a few cases and in certain distance intervals the actual seismic

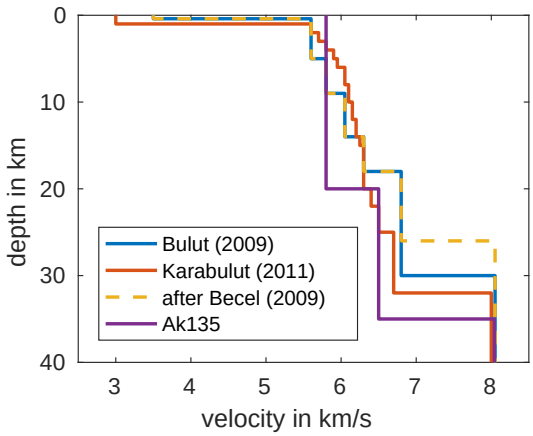

Figure 3.3.: 1-D velocity models derived for the Sea of Marmara by Bulut et al. (2009), Karabulut et al. (2011) and Bécel et al. (2009) where the latter was adapted from a 2-D wide-angle seismic profile and mimics a crustal plateau along the Marmara Trough. The global 1-D model Ak135 (Kennett et al. 1995) is plotted for comparison.

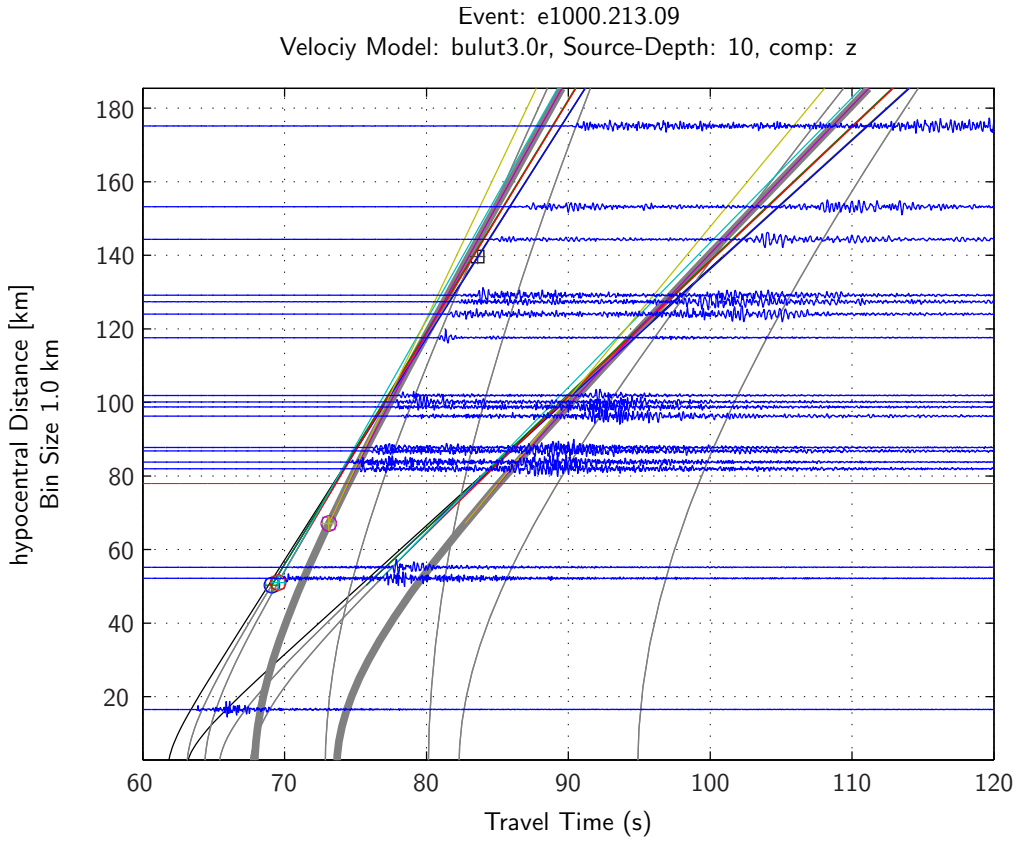

Figure 3.4.: Exemplary record section with travel time curves derived from the optimized velocity model for the eastern Sea of Marmara by Bulut et al. (2009).

phase onsets coincided with the anticipated arrival times (e.g. Fig. 3.4). This was most likely caused by miss location of the event in the initial (merged) catalogue as well as lateral 3-D deviations from the foreclosed velocity models. Nevertheless, visual comparison of the travel-time curves and the waveform of a particular recording at a certain distance revealed the approximate arrival time of secondary crustal phases by adding the corresponding theoretical time difference to the first onset of the P- or S-wave train. The frequency of picks by crustal phase and epicentral distance is depicted in Fig. 3.5a and 3.5b for subset 1 and 2, respectively.

The manual picks of the first subset served as a reference to finetune the automatic picking procedure (also see the end of the next section). Once the algorithm reproduced the manual picks to a satisfactory degree, its performance was independently compared to and evaluated with the second subset. With this procedure we ensured the highest possible picking precision for the automatic picker. An exemplary direct comparison of reference and automatic picks on the three component recordings of an individual station is displayed in Fig. 3.6. Reference picks for a multitude of vertical channels recording one seismic event are shown in a seismic section (Fig. 3.7). A quantitative evaluation of the automatic algorithm's performance with respect to the joint subsets of reference picks is discussed further below in Section 3.4.3.

(a)

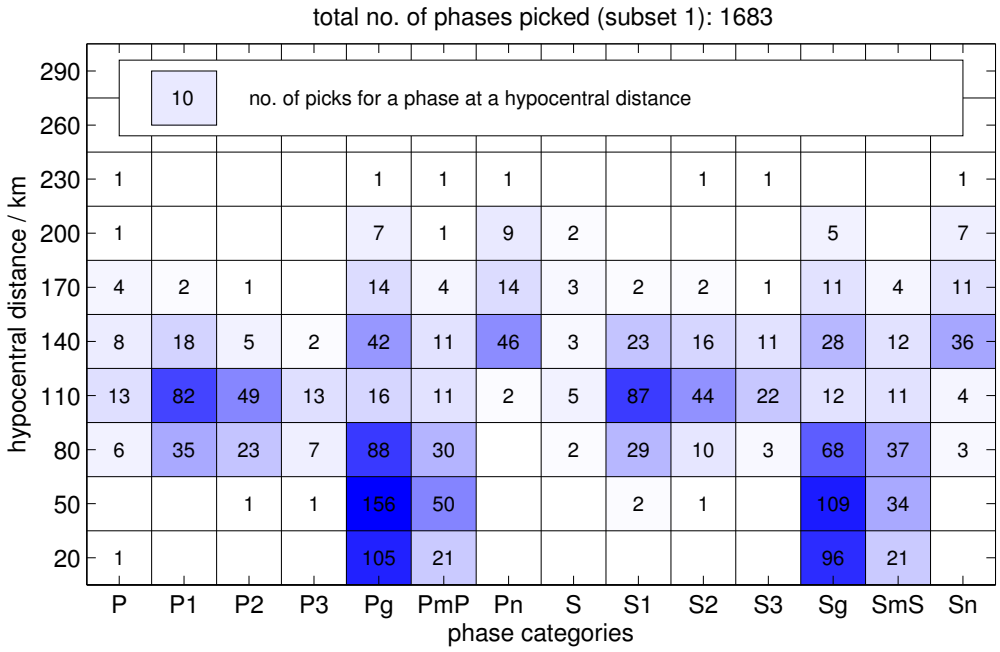

(b)

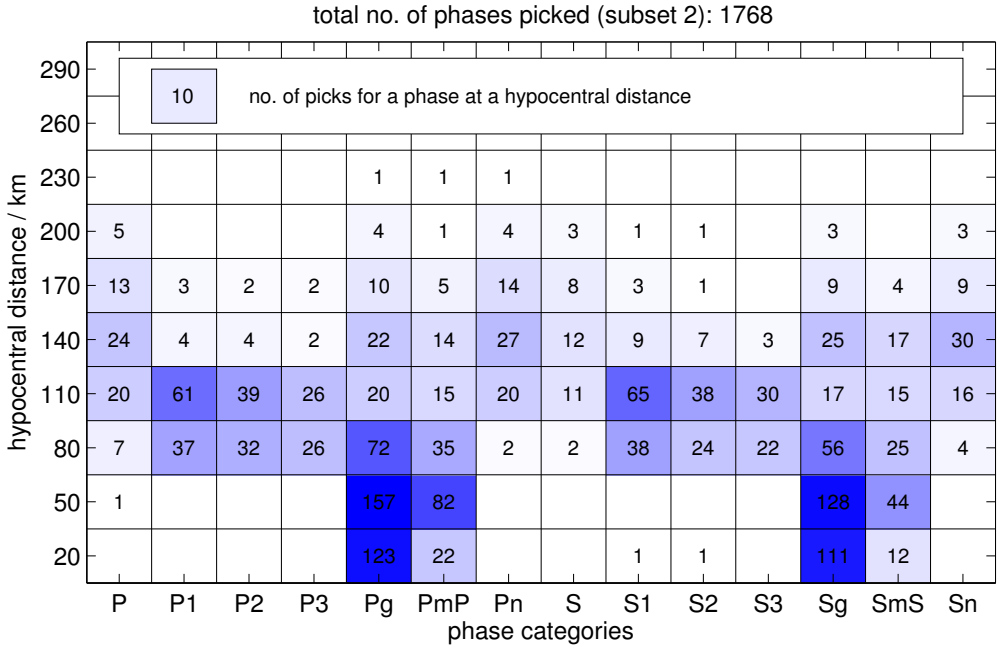

Figure 3.5.: Frequency of picks of certain crustal phases over epicentral distance (a) of reference subset 1 and (b) of reference subset 2.

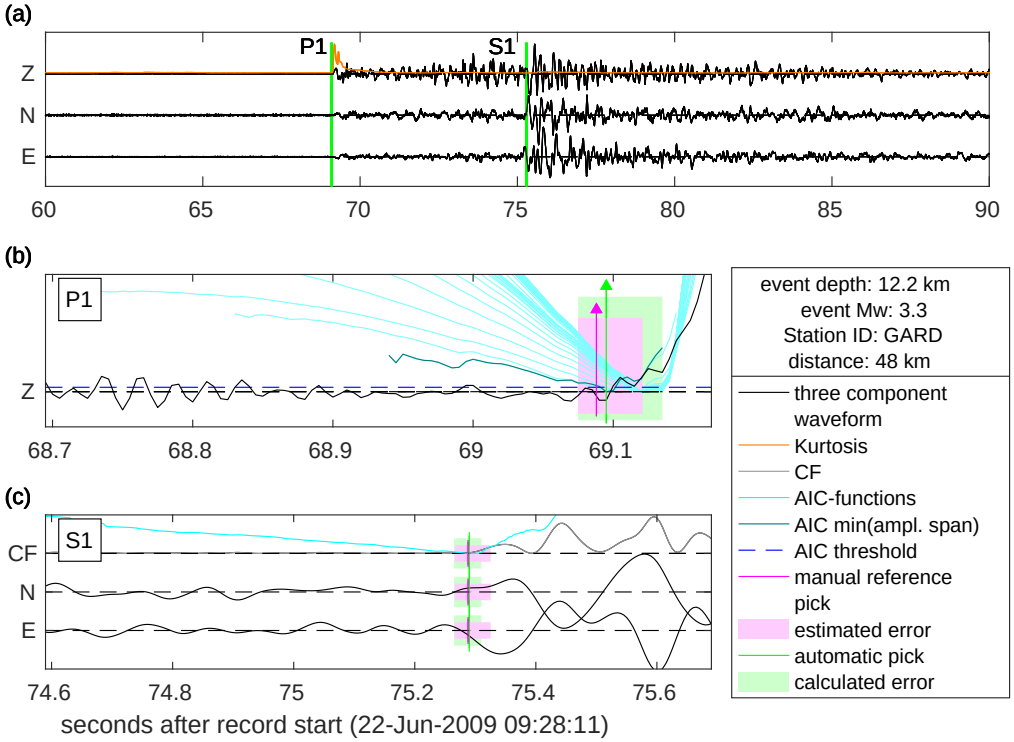

Figure 3.6.: (a) Exemplary 3-component recording with kurtosis (orange line) of the vertical recording and automatic P- and S-picks of the corresponding first arriving phases (P1 and S1 in green). (b)+(c) Zoom-in of the P- and S-pick, respectively, together with the corresponding manual reference picks (in magenta). Pale rectangles depict the interval of uncertainty of the respective pick. (b) Also indicates the manually and automatically determined first-motion polarity of both reference and automatic picks as well as the suit of AIC functions used to automatically determine the P-onset and to calculate its uncertainty. (c) Horizontal components and their characteristic function (CF). The suit of AIC functions used to derive the S-pick and its uncertainty is similar to the one shown in (b) and is subsumed into one representative AIC function for better overview here (also see legend).

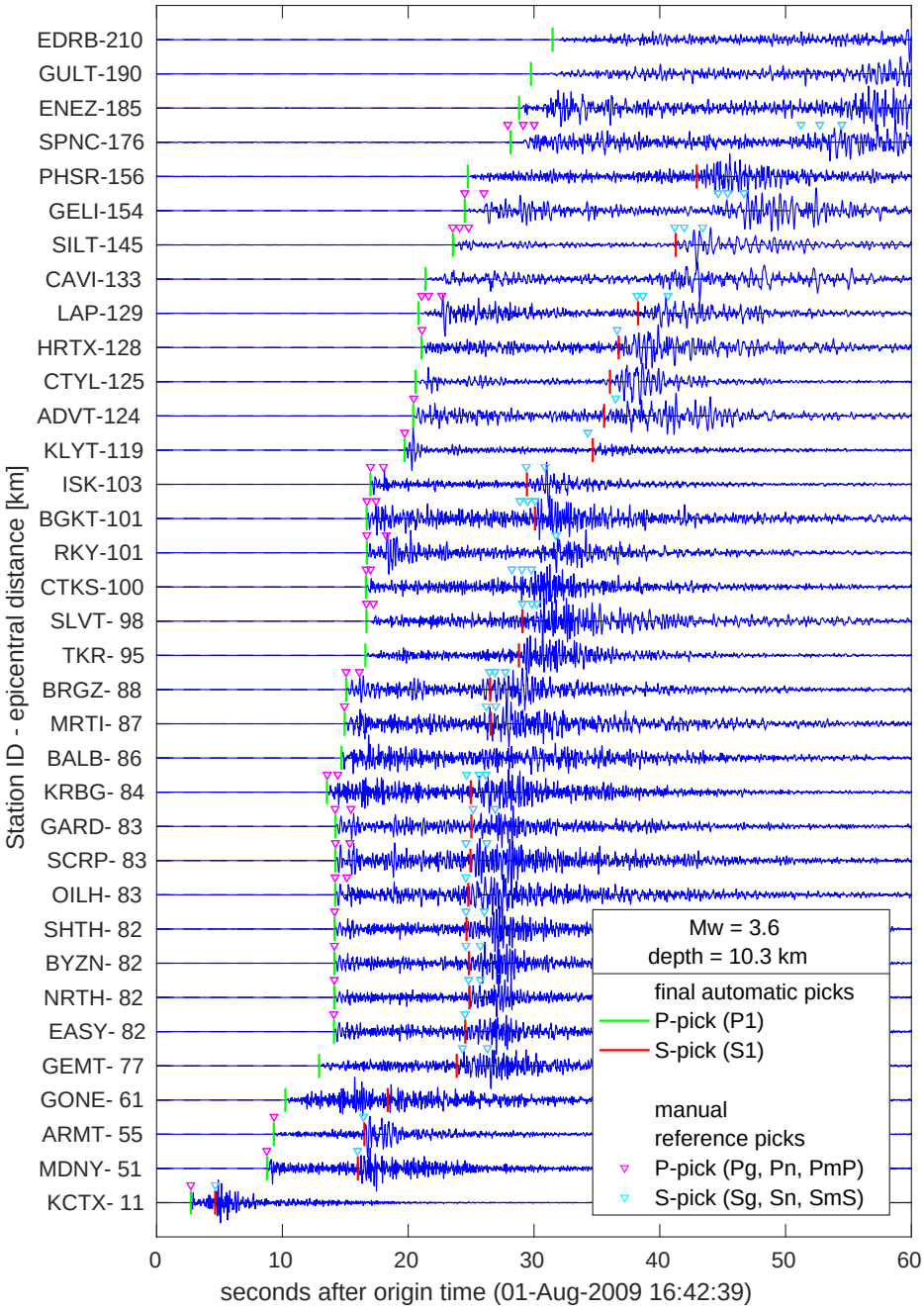

Figure 3.7.: Vertical component recordings of a $M_w = 3.6$ earthquake located in the southern central Sea of Marmara (see Fig. 2.1 for location) plotted with the traces sorted by epicentral distance. Green and red markers indicate automatically derived P- and S-wave onset picks, respectively. Magenta and cyan coloured triangles show manually picked arrival times of different crustal P- and S-phases respectively.

3.4. Automated picking

As an enhancement to 'PILOT' (see Sec. 3.3 Küperkoch 2011), the software used during the manual reference picking, Küperkoch et al. (2010, 2012) developed 'autoPILOT', a MATLAB® based software to automatically determine P- and S-wave onset times. First results for automatically timed P- and S-wave onsets were obtained with this software. However, these results were not satisfactory and thus an alternative processing scheme was developed. The algorithm used in this study retains the approach of Küperkoch et al. (2010, 2012) to use a two-step procedure during which a preliminary and a final pick are set using a narrow and a wider causal band-pass filter. The rationale of this procedure is to first effectively suppress noise and then to include the relevant frequency band. However, the processing scheme proposed by Küperkoch et al. (2010, 2012) was substantially altered and in order to determine the onsets of seismic P- and S-phases as well as to calculate a corresponding uncertainty interval, the approach of a rolling and nested Akaike Information Criterion (AIC) was introduced.

3.4.1. Processing scheme after Küperkoch et al. (2010, 2012)

P-wave Küperkoch et al. (2010) showed that in contrast to other characteristic functions like for instance the short-term average over long-term average (STA/LTA), the kurtosis calculated on a window causally running over the filtered waveform is not only sensitive to amplitude but also to frequency and phase changes, and thus can be used as a characteristic function (CF) to amplify also very subtle onsets of seismic signals. The kurtosis K for a statistical process sampled by $x = [x_1, ..., x_N]$ equals the quotient of the fourth and the squared second statistical moment, $\mu^{(4)}$ and $\mu^{(2)^2}$ respectively,

$$K = \frac{\mu^{(4)}}{\mu^{(2)^2}} = N \frac{\sum_{j=1}^{N} (x_j - \bar{x})^4}{\left(\sum_{j=1}^{N} (x_j - \bar{x})^2 \right)^2} \tag{3.1}$$

where $\bar{x}$ represents the mean value of the suit of samples. As such the kurtosis describes the tails of a statistical process, i.e. for instance compared to a statistical process whose values obey a Gaussian probability distribution, another statistical process will have a higher kurtosis if it produces more extreme occurrences. After transforming the bandpass filtered vertical waveform recording with the rolling kurtosis the onset of the P-phase is crudely characterized by a sharp increase of the CF.

Then Maeda's representation (Eq. 3.2 Maeda 1985) of the Akaike Informa-

tion Criterion (AIC Akaike 1971; Akaike et al. 1974) is applied to the CF. Assuming that a time series is composed of two consecutive portions, each representing a distinct statistical process, the AIC essentially measures the relative misfit of statistical models. The AIC ideally yields a global minimum at that point in time, which best divides the time series in to two distinct statistical models. The k^{th} sample of the AIC applied to a real discrete time series $x = [x_1, ..., x_N]$ is defined as

$$aic_k(x) = k \log\big(var_{1,k}(x)\big) + (N - k) \log\big(var_{k+1,N}(x)\big) \tag{3.2}$$

where $var_{n,k}(x) = var\big([x_n, ..., x_k]\big) = \mu^{(2)}\big([x_n, ..., x_k]\big)$ is the variance (or the second statistical moment) of x restricted to the interval from n^{th} to k^{th} sample. In our case, the time series consists of white noise which is then succeeded by an emerging signal and the AIC's minimum coincides with the onset of the seismic signal. The AIC has been frequently used to determine the onset of seismic signals in other automatized picking algorithms (Zhang et al. 2003; Diehl et al. 2009b) or as visual picking assistance to a human operator (Jousset et al. 2013).

After identifying the global minimum of the AIC, Küperkoch et al. (2010) further refine the pick with a pragmatic scheme involving the original and a smoothed AIC. In 'autoPILOT', the implementation of the "search for a common minimum of the original and a smoothed AIC function"[1] (Küperkoch et al. 2010), results in setting the automatic pick prior to the (original) AIC minimum. The quality of the pick is estimated by means of the slope of the CF after the determined onset time. The same procedure is repeated with the second (the wider) filter.

However, detailed examination of the distribution of picking residuals (i.e. the difference between corresponding automatic and reference pick; also see Sec. 3.4.3) shows that P-picks obtained with 'autoPILOT' are slightly but systematically shifted towards later times (Fig. 3.8a). The reason for that lies in the usage of causally running windows when calculating the kurtosis. The continuous mapping of the samples of some time window to a value associated with the upper bound (or the end) of that time window, will smoothen any abrupt change in the characteristics of a time series and thus delay the detection of any significant change. This characteristic behaviour of time-series transforms involving local averages is confirmed independently in a separate study comparing picks automatically timed with a short-term over long-term average filter (STA/LTA) and picks obtained with the rolling and nested AIC picking scheme (Appendix A.1, Fig. A.2b). The latter algorithm was developed for this study and is described in the subsequent section.

[1] Note that a "common [local or global] minimum" of some time series and its transform by a rolling local average, does not generally exist.

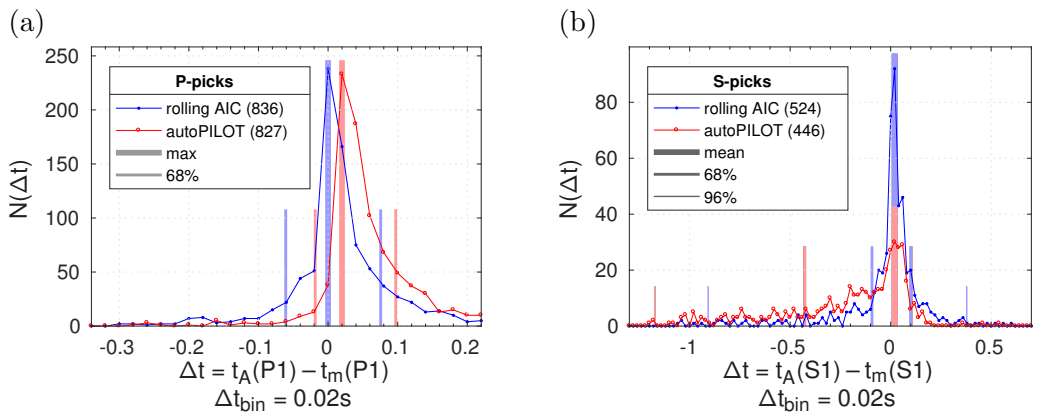

Figure 3.8.: Residual Δt between automatic and manual reference picks with respect to the first incoming crustal phase associated to (a) a P- and (b) a S-wave. The distributions for automatic picks obtained with the here developed rolling and nested AIC picking algorithm and the 'autoPILOT' software (Küperkoch et al. 2010, 2012) are shown in blue and red, respectively. Picks from 72 reference earthquakes were compared (also see Sec. 3.3).

S-wave For the determination of the S-wave onset, Küperkoch et al. (2012) propose an autoregressive multicomponent forward prediction (ARMFP) which adapts the autoregressive (AR) forward prediction (Leonard et al. 1999) to several dimensions. In this procedure the moving time window of the horizontal particle motion (2-D time series) is divided into a "determination" window and a preceding "prediction" window where the former is chosen to be a bit longer than the latter. The recorded waveform in the "determination" window is used to calculate the AR-coefficients on whose basis the temporal development of the horizontal particle motion is predicted. The number of AR-coefficients is equivalent to the AR-model order and, in contrast to Sleeman et al. (1999) who propose a model order of 8 to 10, Küperkoch et al. (2012) argue that a model order of 4 is reasonable to to describe noise or the P-wave coda. The root mean square error of (i.e. the euclidean distance between) the ARMFP and the actual horizontal particle motion is then used as a CF which is sensitive to instantaneous changes in frequency, amplitude, phase and polarization (Küperkoch et al. 2012) and which may indicate an S-phase onset. Then a scheme similar to the one applied for the P-wave onset determination (Küperkoch et al. 2010) is used to time the S-wave arrival. An example of the ARMFP characteristic function is shown in Fig. 3.9 (green graph on the upper x-axis).

Two insufficiencies became apparent during the application of this S-phase picking scheme to the Sea of Marmara seismic recordings.

1. The distribution of picking residuals of first incoming S-phases (Fig.

3.8b) shows that a significant fraction are timed too early by the 'autoPILOT' software. This may have two reasons.

a) 'autoPILOT' uses the unrotated N-E horizontal components to calculate the characteristic function from ARMFP. The horizontal particle motion may thus contain energy from S- to P-converted waves, which are usually recorded as precursors of the S-wave.

b) The previously mentioned shifting of the final pick to a point in time prior to the original global minimum of the AIC function (as a result of the "search for a common minimum of the original and a smoothed AIC-function" Küperkoch et al. 2010) is of marginal effect if the searched onset is impulsive but may grow large if emergent. The latter is often the case for the characteristic function obtained with the ARMFP which has a comparatively low signal to noise ratio around the transition from P-coda to S-wave (Fig. 3.9 and Fig. 4 and 8 in Küperkoch et al. (2012)).

2. The frequency of S-picks per event as function of the epicentral distance (Fig. 3.10) shows that for distances $\leq$ 25 km relatively fewer S-picks are determined as compared to larger distances. This behaviour was found to be caused by determination windows of the ARMFP hanging over the actual S-wave onset at small epicentral distances, thus impeding the calculation of a meaningful prediction of the time series development. A lower bound for the determination-window length was set by low sampling rates of waveforms from the KOERI network recorded before 2009.

These drawbacks of the S-wave picking scheme proposed by Küperkoch et al. (2012) have the potential to compromise accurate results during the travel-time inversion. Earlier S-picks (and later P-picks) would result in shorter S minus P times and thus indicate too small epicentral distances. Further, the lack of S-picks at short epicentral distances is difficult to accept as they are particularly crucial for hypocentral depth determination. Although application of the AIC to the ARMFP yields a minimum coinciding with manual reference pick (cyan graph in Fig. 3.9), thus patching point 1., point 2. (as well as systematically late P-picks) remained unsolved. For this reason a variation of the picking scheme was implemented and the rolling and nested AIC introduced.

3.4.2. A new processing scheme: systematic application of the Akaike Information Criterion

Rolling and nested and AIC The algorithm applied in this study to automatically determine P- and S-wave adapts the approach of Küperkoch et al. (2010, 2012) who use a two-step procedure during which a preliminary and a final pick are calculated. For the preliminary and final P-pick (S-pick) we used

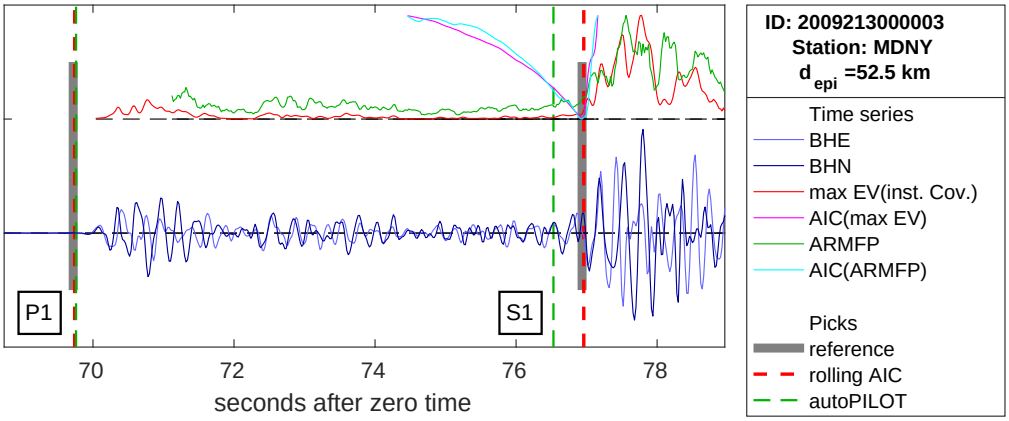

Figure 3.9.: Differently timed first incoming S-phase onsets ($t \approx 77s$) obtained during the manual reference picking (grey), with the here developed rolling AIC picking algorithm (red) as well as with the 'autoPILOT' software (Küperkoch et al. 2010, 2012) (green). At the bottom the seismograms of the two horizontal components are shown in different shades of blue. At the top, the time series of the corresponding characteristic functions obtained from the largest eigenvalue of the instantaneous covariance matrix [max EV(inst. Cov.)] (Vidale 1986) and from the multicomponent autoregressive forward prediction (Küperkoch et al. 2012) are plotted in red and green, respectively. The AIC applied to both characteristic functions on a time window approximately at $74 \leq t \leq 77$ is shown in magenta and cyan, respectively.

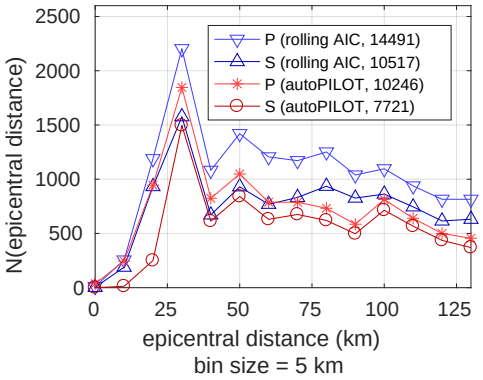

Figure 3.10.: Frequency of automatic P- and S-picks at a certain epicentral distance evaluated on a common set of 838 earthquakes occurring in the Sea of Marmara between 2006 and 2010. The distributions for the here developed rolling and nested AIC picking algorithm and the 'autoPILOT' software (Küperkoch et al. 2010, 2012) shown in blue and red, respectively.

a 3rd order Butterworth band-pass filter with cutoff frequencies of [2, 12] Hz and [1, 33] Hz, respectively ([2, 12] Hz and [1, 16] Hz), where the upper cutoff frequency was adapted to 75 % of the Nyquist frequency for 50 Hz recordings. We additionally defined asymmetric left and right-sided pick uncertainties.

While keeping the two-step approach of Küperkoch et al. (2010, 2012), we here refined the inner procedure by using Higher Order Statistics (HOS, Eq. 3.1) as a refined trigger to crudely estimate the P-phase onset (e.g. Ross et al. 2014). The temporal development of the HOS kurtosis, causally calculated on a 2 s long moving window, and its maximum (crudely indicating the beginning of the wave train) are illustrated in Fig. 3.6a. Furthermore, the Akaike Information Criterion (AIC) (Akaike et al. 1974) in Maeda's representation (Eq. 3.2) (Maeda 1985) was repeatedly applied to different wavelet portions containing the phase onset with high certainty in order to pick it as accurately as possible. However, the precise point in time containing the global minimum is very sensitive to the actual wavelet window transformed with the AIC-function. We thus systematically calculated suits of AIC-functions on rolling and nested windows of the waveform and used the variability of the global minima to estimate an asymmetric uncertainty for the pick.

P-pick A moving window of 8 s length splitting the waveform into 100 overlapping portions was used to calculate the preliminary P-pick. This procedure is illustrated in Fig. 3.11a with eight rolling windows of a narrowly filtered seismogram thus obtaining a preliminary P-wave onset. The moving windows always contained the maximum of the kurtosis with an overlap of 1 s such that each window of the underlying time series contained noise and a portion of the seismic signal. This ensured, that a meaningful minimum for each AIC-function was obtained.

The final pick is obtained by means of 100 nested waveform windows on which the AIC was applied. The largest window was 8 s long and all windows contained the uncertainty interval of the preliminary pick. For eight nested windows the procedure is illustrated in Fig. 3.11b. Fig. 3.6b shows a closeup of the vertical recording in Fig. 3.6a around the P-pick. Each AIC-function has a global minimum and the earliest of all is defined as the most likely onset. The pick's uncertainty was then defined as the time domain within which the suit of AIC-functions remains below a certain threshold. This threshold was individually defined for every pick. Out of all members of the corresponding suit of AIC-functions we chose that with the smallest span of amplitudes (dark cyan in Fig. 3.6b) and define the threshold as twenty and ten percent of its largest deflection (dashed blue horizontal line in Fig. 3.6b) for the preliminary and final pick, respectively. The earliest and latest possible times for the phase onset were then defined as the left- and right-sided bounds of the pick's uncertainty.

The P-wave uncertainty assessment described above was developed in or-

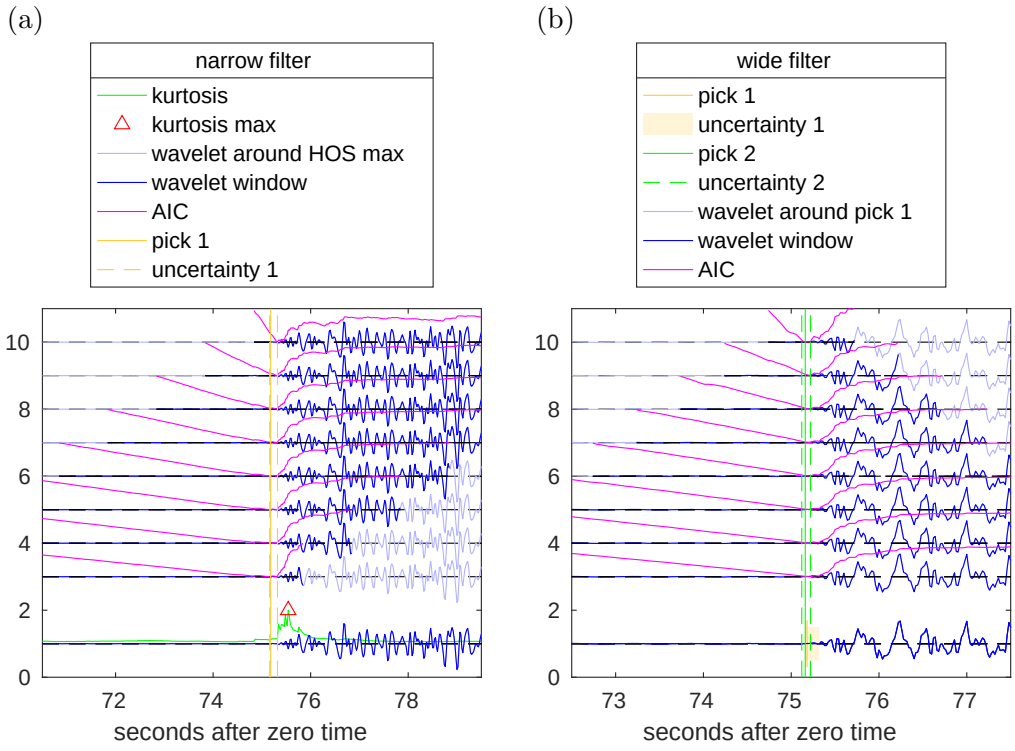

Figure 3.11.: (a) Exemplary rolling and (b) nested application of the AIC on a narrowly and a widely filtered waveform, yielding the preliminary and final pick with uncertainties (Pick 1 and 2), respectively.

der to capture not only the uncertainty inherent by the shape of the onset, i.e. emergent or impulsive, and the signal-to-noise ratio (SNR), but also the frequent scenario of close sequential phases, e.g. a head- followed by a direct wave close to the crossover point (see the Section 3.3) where, the first phase onset may be closely succeeded by a more prominent one. In such a case, the targeted first onset is often mistaken for the more prominent one, not only by the original automatic algorithm (Küperkoch et al. 2010) but also in manual phase readings (Diehl et al. 2009a). Usually the automatic algorithm can be tuned to pick the correct onset on an individual trace, yet with dramatic consequences for the accurate processing of other traces. Our approach is designed to assign larger uncertainties in these doubtful cases, possibly spanning a time interval containing both onsets.

S-pick A similar two-step procedure with suits of rolling and nested AIC-functions were also used to calculate the S-picks and their bounds of uncertainty. Here we followed (Grigoli et al. 2014) and calculated the temporal development of the largest eigenvalue of the instantaneous covariance matrix (Vidale 1986) (uppermost graph in Fig. 3.6c and red graph in Fig. 3.9) of both horizontal waveform components (E- and N-components in Fig. 3.6c and Fig. 3.9).[2] The time series served as a characteristic function (CF) and was then used to calculate the suit of AIC-functions.

Rejection of picks The picking process was interrupted and the corresponding pick discarded under the following circumstances:

1. the trace had smeared energy, i.e. the temporal distribution of energy peaks in the 4 min long waveform was not concentrated on a bounded domain as characteristic for a well recorded earthquake,

2. the P-pick was too early or too late, i.e. occurring at a point in time that belongs to a different event or an epicentre outside the network,

3. the P-wave had a lower SNR on the vertical component than on the horizontal components (indicating that the P-pick has likely been set in front of a S-wave onset),

4. P- or S-pick had SNR below 1, or

5. the S-pick SNR was too low.

[2] In this case, i.e. for two time series, the instantaneous covariance is expressed by a 2x2-matrix whose first eigenvalue equals zero and the second (the largest) reads

$$\lambda_{max}(t) = |X(t)|^2 + |Y(t)|^2 \,. \tag{3.3}$$

$X(t)$ and $Y(t)$ are the analytical representations of the time series, $x(t)$ and $y(t)$, e.g. $X(t) = x(t) + i \cdot \mathcal{H}(x)(t)$ where $\mathcal{H}(x)(t)$ is the Hilbert transform of $x(t)$ and $i^2 = -1$.

We used the automatic algorithm described above to analyse ∼580,000 three-component recordings from 12,186 earthquakes, this way retrieving ∼360,000 P- or S-picks in total. Figure 3.7 shows automatic P- and S-picks on top of the vertical waveforms of a seismic event ($M_w = 3.6$) recorded throughout the unified seismic network. The manual reference picks are shown for comparison.

First motion In order to determine focal mechanisms for the best covered and located events, in addition to the onset times the first-motion polarities of P-waves were also determined automatically. After applying the same band-pass filter as for the final P-pick to the vertical recording, we measured the slope of two straights both crossing the first local extremum after the pick. The first straight also intersects the amplitude at the picked P-wave onset whereas the second intersects the first local extremum before that point in time. The first motion was declared to be positive or negative, if both straights had positive or negative slope, the ratio of maximum signal to maximum noise level was larger than 4, and the standard deviation of noise and signal was larger than 3, where the waveform interval of [-1.00, -0.05]s and [0.05, 0.30]s before and after the P-pick were considered to represent noise and signal, respectively.

Tuning of the algorithm For the tuning of the algorithm the interplay of the band-pass filters and the windowing of the seismograms was important. We chose a narrow band-pass filter first, to reduce noise as much as necessary in order to obtain characteristic onsets of the kurtosis. The width of the second filter was increased to display details of the phase onset as for instance the first-motion polarity. The width of the wavelet windows as base for the suits of AIC-functions as well as their overlap with a characteristic point in time (the maximum of the kurtosis and the maximum of the CF for the P- and S-pick, respectively) was also adopted to the regional seismicity observed. The AIC-threshold was chosen larger for the preliminary pick, thus creating a sufficiently large time interval for the search of the final pick. The range of decisive parameters and their dimensioning in comparison to the application of the algorithm to local (induced) seismicity is summarized in Table A.1.

3.4.3. Assessment of automated picks with respect to reference picks

Picking residuals We performed a quantitative comparison of manually derived reference picks of the different crustal phases and the automatically calculated P- and S-phase onsets by calculating their time difference (Fig. 3.12). The picking residual for the primary phase (P-wave) is thus defined as $\Delta t = t_A(P1) - t_m(\tilde{P})$ where $t_A(P1)$ represents the automatically determined pick and $t_m(\tilde{P})$ several manually derived reference phase onsets of different crustal phases as defined above (Section 3.3), namely $\tilde{P} \in \{Pn, Pg, PmP, P1, P\}$.

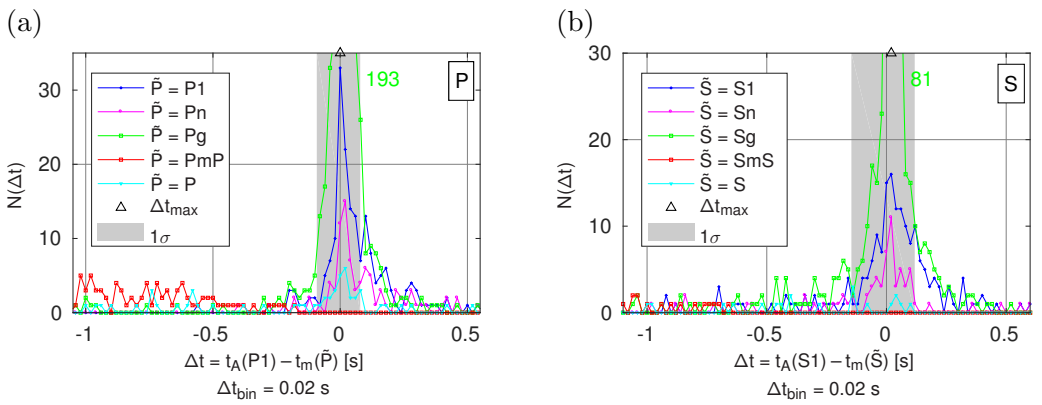

Figure 3.12.: Residual Δt between automatic and manual reference picks with respect to different crustal phases associated to (a) a P- and (b) a S-wave (see Section 3.3 for detailed explanation, e.g. of individual ray paths of different crustal phases). The area shaded in darker grey indicates the interval with 68 % of the pick residuals (1σ neighbourhood).

As such Δt is negative/positive if the automatic pick is earlier/later than the designated reference pick. $\Delta t = t_A(S1) - t_m(\tilde{S})$ is defined equivalently and the distribution of Δt is shown for the combined subsets of reference events for the P- and S-phases in Fig. 3.12a and Fig. 3.12b, respectively.

The automatic algorithm was designed to pick the first arriving phase only. Therefore, the distributions for the automatic picking residual to $\tilde{P} = Pg$ and $\tilde{P} = Pn$ (green and magenta graphs in Fig. 3.12a and 3.12b), whose order of arrival depends on the epicentral distance, consider reference picks only if they are first to arrive. The residual distribution obtained from stacking the distributions for the reference phases Pg, Pn, P1 and P (i.e. all first arriving P- and S-phases expected to correspond to the automatic P1- and S1-pick) peaks at zero time difference and contains 68 % of all values within ∼0.1 s. The equivalent distribution for the S-phases peaks at 0.02 s and contains 68 % of all values within ∼0.3 s. Fig. 3.12a and Fig. 3.12b also show the residual distributions to the reflected crustal phases PmP and SmP. They only count negative values indicating that, as expected, the automatic algorithm always picked earlier on the corresponding trace.

Pick uncertainties The distribution of left and right sided uncertainties for P- and S-picks determined with the here developed algorithm is depicted in Fig. 3.13a. The σ_1 (σ_2) neighbourhood, i.e. the bound including 68 % (95 %) of all values, for the left and right uncertainties is approximately -0.06 and 0.04 s (∓ 0.3 s) for the P-picks and approximately -0.2 and 0.1 s (-0.7 and 0.6 s) for the S-picks. Together with the bivariate analysis of left and right sided uncertainties (i.e the occurrence of certain pairs of values, Fig. 3.13b),

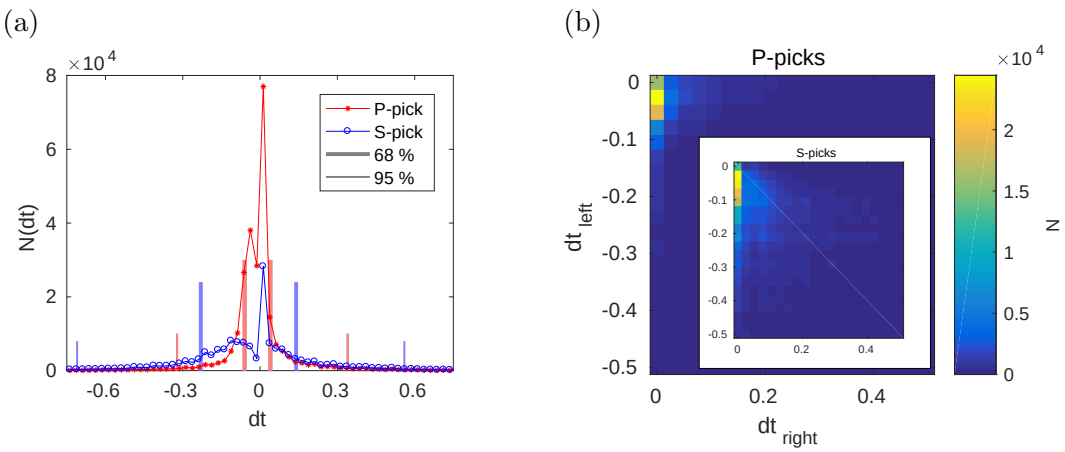

Figure 3.13.: (a) Frequency distribution of automatic P- and S-pick uncertainties in red and blue, respectively. (b) Bivariate analysis of left and right sided uncertainties for P-picks (and S-picks in the inset. In (a) and (b), negative and positive values indicate left and right sided uncertainties, respectively.

this indicates that compared to the right sided, the left sided uncertainties are slightly larger on average.

Figure 3.14a and Fig. 3.14b show two-dimensional histograms comparing the uncertainty assigned during the reference picking (x-axis) and that calculated by our algorithm (y-axis) for P- and S-picks respectively, where the picking uncertainty is defined as the domain of uncertainty, i.e. the time difference between latest and earliest possible pick $dt = t_l - t_e$ (see Section 3.3 and Section 3.4). Diagonal elements represent cases where automatic and reference uncertainty lie in the same range.

Over 35 % of uncertainties assigned during the reference picking of P-wave onsets lie in the range between 0.025 and 0.125 s (i.e. in the histogram bins of 0.05 s and 0.10 s) and have a corresponding automatic pick in the same uncertainty range (Fig. 3.14a). Increased occurrences above the diagonal at reference uncertainties larger or equal to 0.15 s indicate that the statistical uncertainty estimation performed by our algorithm undermatches the reference uncertainties in this interval. The spread of calculated S-pick uncertainties is much larger than that of the P-picks (Fig. 3.14b). Most reference uncertainties lie in the histogram bins between 0.05 s and 0.35 s and a large fraction is paired with slightly lower calculated uncertainties. However, the automatic algorithm also returns a tail of larger uncertainties. The discrepancy can be explained with the different approaches for determining the pick uncertainties: on the one hand the deterministic approach described by Diehl et al. (2009a) is still subjected to the consistent performance of the human operator, whereas the algorithm relies on a multitude of statistically derived picks repeatedly applying the AIC. Overall the distributions of P- and S-pick uncertainties

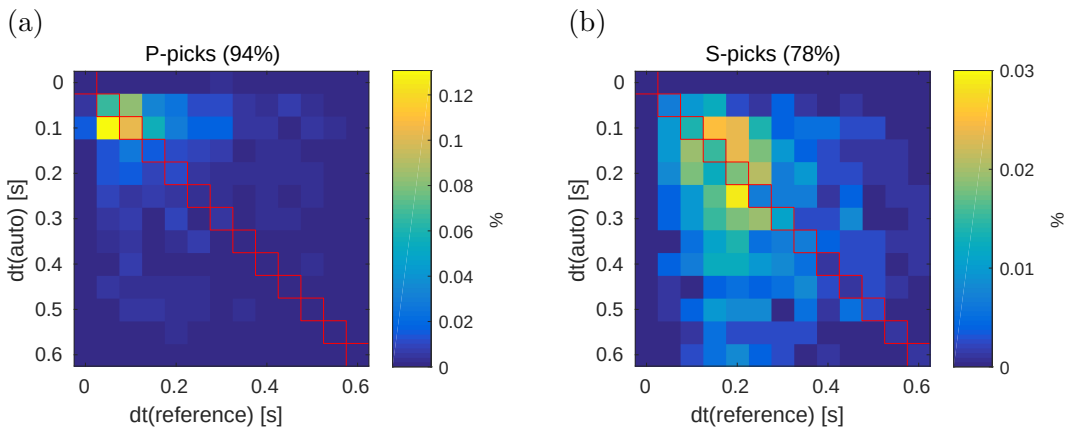

Figure 3.14.: Two-dimensional histograms in (c) and (d) display how well the picking uncertainties calculated by our algorithm, dt(auto), match those assigned during the reference picking, dt(reference). Each square has a width of 0.05 s. The percentage in the title expresses the fraction of uncertainty pairs with both uncertainty values below 0.6 s.

calculated with our algorithm peak at smaller values and have a long tail of large values.

First-motion polarities We also compare automatically calculated with manually derived first-motion polarities. Fig. 3.15 displays the fraction of manually derived Up- and Down first-motions that were determined with the same or opposite polarity or were left undetermined by the automatic algorithm. In this way we can estimate that on average, out of all reference Up- and Down-first-motions 90 % were determined correctly.

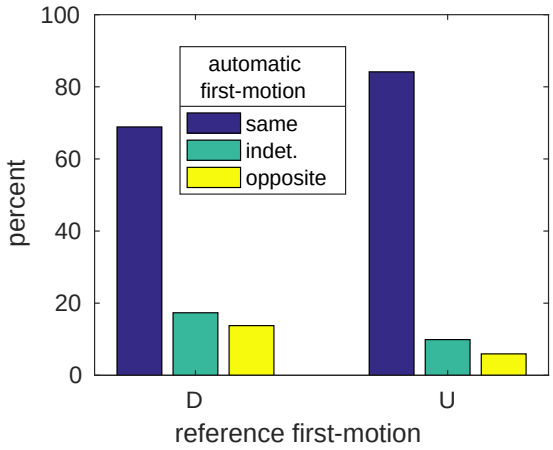

Figure 3.15.: Automatically calculated first-motions in relation to previously manually determined Up- and Down-first-motions.

4. A unified earthquake catalogue for the Sea of Marmara Region, Turkey, based on automatized phase picking and travel-time inversion: Seismotectonic implications[a]

Abstract The Marmara section of the North Anatolian Fault Zone (NAFZ) is late in its seismic cycle and can be expected to produce a magnitude M up to 7.4 earthquake during the next decades in direct vicinity to the 15-million population centre Istanbul. This setting translates the seismic hazard into very high risk and makes a thorough understanding of the current seismotectonic setting of this NAFZ section a pressing task. The absence of near-fault stations along most part of the offshore Marmara section limits the reliability of existing seismicity catalogues for this region. For the first time we combine the different regional permanent networks thereby optimizing azimuthal coverage and present a refined hypocentre catalogue for the Sea of Marmara on this basis. Compared to the original locations, adoption of a refined automated technique to determine precise onset times for the different body waves and an iterative travel-time inversion scheme, lead to substantial improvement of 6812 absolute earthquake locations, particularly in the epicentral distribution. The automated processing is explained in detail. Further optimization is achieved through relative relocation of 4407 earthquakes. Our catalogue covers more than a decade (2006 – 2016) with a regional moment-magnitude of completeness of $M_c = 2.1$. The epicentral distribution delineates the Marmara Section, i.e. the northern NAFZ branch, as the seismically most active fault strand. We identify

[a]This chapter is an excerpt from a research article published in Tectonophysics: **C. Wollin**, M. Bohnhoff, P. Martínez-Garzón, L. Küperkoch and C. Raub (2018a). "A Unified Earthquake Catalogue for the Sea of armara Region, Turkey, Based on Automatized Phase Picking and Travel-Time Inversion: Seismotectonic Implications". In: *Tectonophysics*. https://doi.org/10.1016/j.tecto.2018.05.020.
The excerpt reflects the publication's main results.

several aseismic fault patches that are interpreted to represent locked parts of the fault. Seismic activity in the past decade predominantly occurs off the main fault on the edges of the aseismic patches, supporting previous studies that the Marmara section of the NAFZ contains both locked and creeping fault portions. Single-event focal mechanisms ($2.7 \leq M_{\mathrm{w}} \leq 4.5$) indicate that currently both strike-slip and normal faulting occur, confirming the transtensional setting of the region.

4.1. Introduction

In this paper, we present a unified hypocentre catalogue for the time period 2006–2016 combining for the first time the two major national permanent seismic networks of the region operated by the Disaster and Emergency Management Presidency of Turkey (AFAD) and the Kandilli Observatory and Earthquake Research Institute (KOERI), and also including near-fault recordings from the local PIRES (Princes' Islands Realtime Earthquake monitoring System) and GONAF (Geophysical Observatory at the North Anatolian Fault) networks in the eastern Sea of Marmara. The unified seismic network consists of a total of 83 land-based permanent seismic stations in the immediate vicinity of the Sea of Marmara region with full azimuthal coverage and locally unprecedented station density. The integrated data from the different seismic networks was consistently processed using a refined automated picking procedure developed and fine-tuned to determine arrival times of the P- and S-waves with the highest possible precision. The newly compiled homogeneous seismicity catalogue allows to define the individual fault strands of the NAFZ below the Sea of Marmara and their faulting kinematics from focal mechanism solutions. Based on refined relative hypocentre relocations, seismically active or quiet fault segments throughout the Marmara region are identified and discussed in the light of the pending $M > 7$ earthquake.

The paper is organized as follows. After introducing the tectonic setting of the North Anatolian Fault Zone in the Marmara region (Sec. 2.1), we describe the integrated data and our employed automatized processing scheme (Sec. 2.3). While the automatically determined picks can be considered intermediate results and we evaluate their quality at this point of methodical account, section 4.3, 'Results and Discussion', is dedicated to the description and interpretation of the new earthquake locations, magnitudes as well as focal mechanisms (which are based on the picks). We finally conclude on the insights gained by creating a unified and consistent earthquake catalogue (Sec. 4.4).

4.2. Hypocentre determination

4.2.1. Travel time inversion

With ∼360,000 automatically determined P- and S-wave arrival times (P- and S-picks) we perform a travel-time inversion using the HYPOSAT software (Schweitzer 2001) that is based on Geiger's stepwise linearised least-squares method (Geiger 1912). We tested the performance of different 1-D velocity models and selected the model from Karabulut et al. (2011) that was developed for the broader Sea of Marmara region. We selected this particular model due to the best trade-off between number of relocated events and depth accuracy. We then calculated station corrections in order to account for a systematic delay or acceleration of phase arrival times due to heterogeneities of the wave propagation velocity in the rock volume in the immediate vicinity of a seismic station. For this purpose, we first inverted for the hypocentre of every earthquake using picks with the smallest uncertainties (P-picks were included if they belonged to the lower 66-percentile of an event's P-pick uncertainty distribution or if they belonged to the 95-percentile and had a S-pick, which was then also included in the inversion). At this point HYPOSAT performed two subsequent inversions, where the depth was kept constant during the first and was then retrieved after the second inversion. The correction for the P- and S-phase arrival times at a station was then obtained from the mean of the travel time residual distribution of all preliminary locations at this particular station. The succeeding inversions performed to obtain the final locations, used travel times from which the corresponding station corrections were subtracted.

In order to identify and discard imprecise picks and at the same time retain as much travel-time information as possible, we implemented an iterative inversion scheme similar to Sippl et al. (2013) which tests the results of many inversion runs obtained with different sets of picks. The high number of possible combinations of picks associated with an earthquake prevents the rigorous testing of all such combinations, and the presented work-flow is a compromise to computational expense. The earthquake location methodology applied here was as follows:

1) In a first step, we calculated the standard deviation of $y = t_A(S) - sqrt(3) * t_A(P)$ for pairs of automatic P- and corresponding S-picks, $t_A(P)$ and $t_A(S)$ respectively, assuming $v_P/v_S \approx \sqrt{3}$. We then preliminarily excluded S-picks for which y is beyond the 1σ neighbourhood.

2) For the initial inversion of this iterative procedure the remaining picks from 1) were subjected to the same selection as used during the calculation of station corrections. Here and in the subsequent steps, travel times were directly inverted for a hypocentre location until otherwise stated (in contrast to HYPOSAT's optional procedure to perform two inversions keeping

depth constant during the first and retrieving it after the second, the direct inversion for the hypocentre is computationally much faster).

3) Successively removing picks with travel time residuals exceeding two times the travel time RMS (tt-RMS), the inversion was repeated while the tt-RMS of the new location dropped below 2/3 of the value of the previous run or a minimum of four P-picks was reached.

4) In order to regain as much information about the event as possible we re-tested all picks discarded in the previously described steps 1)–3). The picks to be tested were sorted according to the epicentral distance of the associated station, quality (smallest uncertainty margin) and phase. Beginning with the best P-phase of the nearest station, the picks were individually added to the set of picks previously inverted and kept only if the added pick's residual did not exceed 2.5 times the new location's tt-RMS and the latter did not exceed 1.2 times the tt-RMS of the result of the last inversion run yielding an improvement, where the last location obtained in step 3) was used as initial reference.

5) The set of picks obtained after step 4) was considered best and the location constrained by choosing HYPOSAT to invert for the epicentre with fixed depth before inverting for the depth as well (this is the default behaviour of HYPOSAT and also yields the best locations when a consistent set of picks is provided). If the results deviated significantly from the location obtained after step 4) the inversion was considered unstable. In this case we attempted to obtain a better constraint on the epicentre by repeating steps 2)–4) with the hypocentral depth fixed at 10 km. Doing so, the inversion did not yield any estimate for the depth uncertainty.

6) Finally, we checked the consistency of depth and depth uncertainty. If the event was located with zero depth, or the upper bound for the depth's uncertainty exceeds the surface level or no depth uncertainty was retrieved, we inverted the most suitable set of picks obtained from step 4) with fixed depth, where different values for the depth were probed. We began with depths from 0 to 30 km in a 5 km spacing. The subsequent loop probed the depth interval around the depth of the location with the lowest RMS value in a 1 km spacing. This procedure was repeated until reaching a spacing of 0.1 km and the final location was chosen by the lowest RMS value.

The parameters presented in 1)–4) were found by optimizing earthquake locations achieved with a number of observations larger than average but at the same time resulting in large location uncertainties in terms of tt-RMS and error ellipse area. With this procedure we determined a total of 11,835 absolute hypocentres out of the 12,816 events for which P- and S-onset times were picked. Table 4.1 shows how categories of best, good and fair event locations

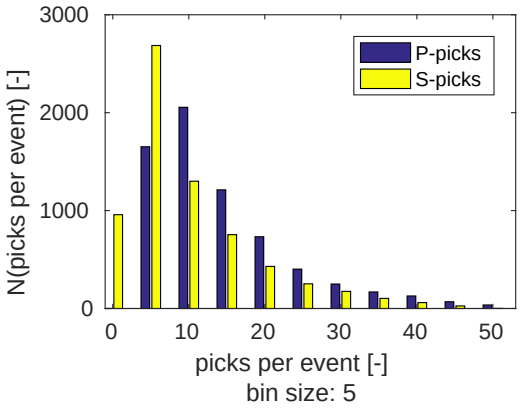

Figure 4.1.: Frequency of events located with a certain number of P- and S-picks (the two distributions must be read separately from one another, e.g. the majority of events were located with 8-12 P-picks and ≈1000 with 0-3 S-picks). Events falling under the category of best, good or fair locations are considered (see Table 4.1). The bins are centred around multiples of five.

can be obtained by imposing limits to the minimum number of total, P- or S-picks as well as maximum values for the azimuthal gap and horizontal uncertainty (expressed by the error ellipse area), where the sets of locations are nested with increasing strictness of the selection criteria, e.g. the set of good locations is a subset of the set of fair locations. Out of 6812 fair locations 5098 were retrieved after step 5) of the iterative inversion scheme, 1714 after step 6). For these locations a total of $\sim 98,600$ P- and $\sim 65,700$ S-picks have finally been inverted. Figure 4.1 displays the frequency of fair locations with a certain number of P- and S-picks and Fig. 4.2 the travel-time residual RMS distributions by quality. Approximately 2000 of the fair locations are characterized by RMS-values smaller than 0.2 s, thus underestimating location-uncertainty and indicating that more phase-arrival observations would be needed to realistically constrain it. Fig. 4.3 displays histograms of the horizontal uncertainties in terms of the error ellipse area and vertical location errors in km^2 and km (blue graph in the main plot and yellow in the inset), respectively. The abundant occurrence of vanishing vertical uncertainties smaller than 1 km affects locations of all qualities and is clearly too optimistic. We obtain a more realistic estimation after refining the hypocentres with a relative relocation procedure described in the following section. The epicentres of this subset of well located events are shown in Fig. 4.4a and discussed in the corresponding Section 4.3.1.

4.2.2. Double-difference relocation of hypocentres

In order to further refine the relative precision of hypocentres we relocated the catalogue of absolute locations employing the double-difference technique

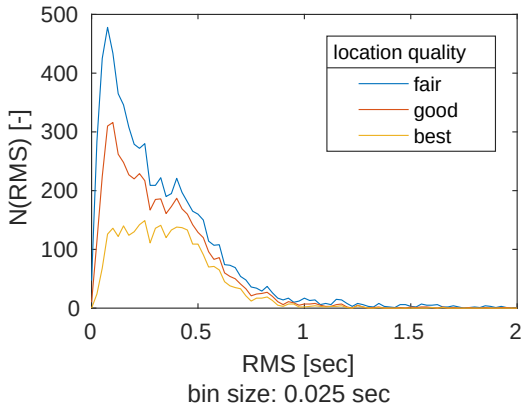

Figure 4.2.: Travel time RMS distribution of absolute locations by location quality (see Table 4.1).

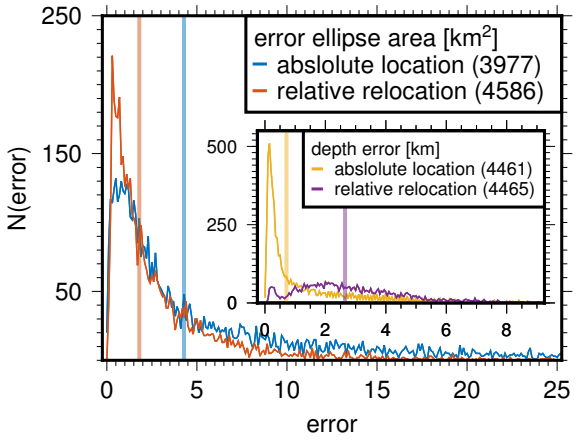

Figure 4.3.: Frequency distributions of horizontal uncertainty in terms of the error ellipse area in km^2 and depth uncertainty in km (inset) of relative relocations and corresponding absolute locations, where the histogram bin-size is $0.5\,km^2$ (km). The median of each distribution is indicated by thick vertical lines in the corresponding colour and the number in brackets behind the legend entries equals the sum of all data points shown.

(Waldhauser et al. 2000). For each earthquake, we computed differential travel times to up to six neighbouring events with a maximum separation of 20 km and based our relocation procedure on the P- and S-wave automatic picks. In the first iterations of the relocation procedure, all differential travel times were considered, and the differential travel times from S-waves were given half of the weight of the corresponding differential travel times from the P-waves. In the following iterations, we constrained the residual threshold gradually up to 0.5 s as well as the maximum distance between linked pairs gradually down to 6 km. After the relocation procedure, we obtained 4657 refined hypocentral locations. We further produced suits of 100 locations for every event by repeating the relocation procedure 100 times, perturbing the set of differential travel times according to their distribution obtained at individual stations. The hypocentral uncertainty was then assessed for individual events where the distribution of the corresponding locations defined error-ellipsoids containing 68 % of solutions (Waldhauser et al. 2000). Table 4.3 lists how the very best locations can be obtained upon imposing limits to the extent of the error ellipse. A refined regional catalogue of 4407 high-precision hypocentres is further analysed and discussed (Fig. 4.4b). The according distribution of the horizontal and vertical uncertainties is summarized in Fig. 4.3 (red graph in the main plot and purple graph in the inset, respectively). Compared to the absolute locations, particularly large horizontal uncertainties have been improved. The distribution of the vertical uncertainties of our final locations has a global maximum at 2.0 km and a mean value of ∼3.8 km.

4.2.3. Calculation of Moment Magnitudes

In order to unify the magnitude scale of the examined earthquakes, moment magnitudes were determined following a procedure that was recently applied to data sets from the eastern Sea of Marmara and Izmit/Düzce regions (Raub et al. 2017). The method relies on using J and K integrals over the squared velocity and displacement spectra, respectively, as first introduced by Andrews (1986) and Snoke (1987). Here, the spectra were calculated for waveform portions of vertical components around the P- as well as of horizontal components around the S-wave onset. Corrections for instrument response, spectral bandwidth and attenuation were applied in the frequency domain, and the low-frequency spectral level, needed for calculating the seismic moment, was estimated from the J and K integrals (Eq. 10 in Snoke (1987)). The moment magnitude was finally derived from the seismic moment using the relationship given by Hanks et al. (1979). For details on the magnitude determination we refer to Raub et al. (2017). P- and S-wave velocities at the source were determined using the 1-D velocity model also used during the travel time inversion (Karabulut et al. 2011). We estimated an earthquake's magnitude as the mean of all moment magnitudes retrieved from the individual traces of all

Table 4.1.: Different employed quality classifications and resulting number of absolute event locations $N_{locations}$, based on the following criteria: minimum number of picks (N_{min}), minimum number of P- and S-picks ($N_{P,min}$ and $N_{S,min}$, respectively) , maximum area of the ellipse representing the horizontal location uncertainty ($A_{errEll,max}$).

	Quality	$N_{locations}$	GAP_{max}	N_{min}	$N_{P,min}$	$N_{S,min}$	$A_{errEll,max}$
1	best	3054	180°	0	10	5	$36km^2$
2	good	4937	200°	0	4	3	$64km^2$
3	fair	6812	270°	7	0	0	$256km^2$
4	all	11835	360°	0	0	0	inf km^2

three-component recordings associated with an event. We only excluded waveform recordings with a signal-to-noise ratio smaller than 10, measured around the corresponding phase onset and within the used bandwidth for the magnitude determination. Results for the calculation of 5353 moment magnitudes are further discussed in the following section.

4.3. Results and discussion

4.3.1. Absolute epicentral and magnitude distribution

The iterative localization scheme described in the previous section yields 11,835 absolute hypocentre locations of varying location quality. Thus we applied strict quality criteria to only select events with highly reliable locations for further interpretation (Table 4.1). Figure 4.4a depicts the epicentral distribution together with individual error ellipses of the catalogue of absolute earthquake locations subsumed under the category of fair locations for which events had to be located with at least seven picks, an azimuthal gap smaller than 270° and an error ellipse area of less than 256 km^2.

For locations categorized as fair, magnitudes were calculated as described in the previous Section 4.2.3. The magnitude range of the catalogue extends between $M_{\mathrm{w,min}} = 0.7$ and $M_{\mathrm{w,max}} = 4.5$ the variance of the individual network-magnitudes being smaller than 0.2 for all of the earthquakes. We used the goodness of fit method (Wiemer et al. 2000) as described by Raub et al. (2017) to calculate the magnitude of completeness M_{c}. The b-value was calculated on the basis of the maximum likelihood method (Page 1968). Both methods were applied to the catalogue of fair absolute locations after removing events which were located shallower than 5 km and within areas that most likely contain quarry-blasts (green patches in Fig. 4.4a). These areas were defined by the joined 4 km neighbourhoods of quarry-blasts, intersected with land. The quarry-blast locations were taken from a separate catalogue provided by KOERI (see Fig. 4.4 for the according www-link). M_{c} and b-value were calcu-

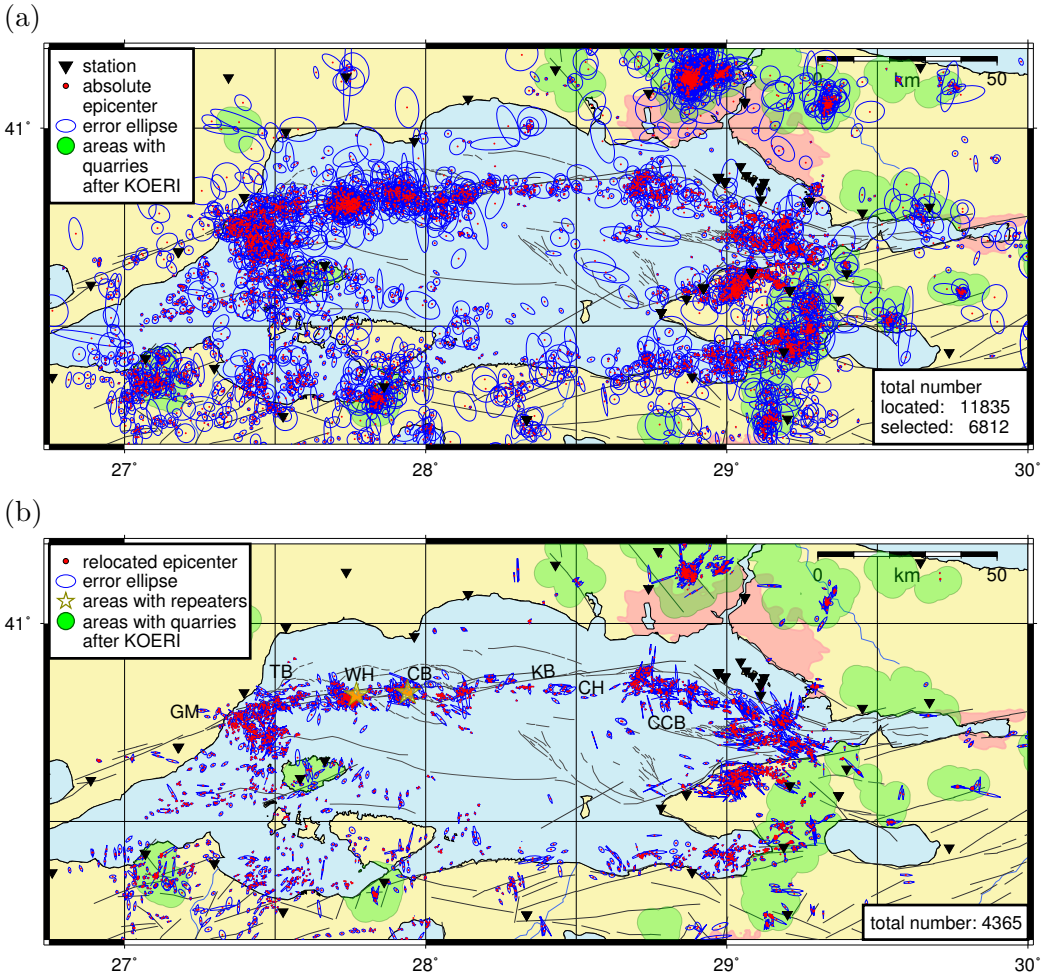

Figure 4.4.: (a) Epicentral distribution of absolute locations in the broader Sea of Marmara region based on the automatic picks from the virtual network of 86 stations surrounding the Marmara Section of the NAFZ. A total of 6812 out of 11,835 located events of "Fair" quality (see Table 4.1 for specific constrains) were selected here. Epicentres are plotted with their lateral error ellipses. (b) Relative relocated epicentres of good quality (see Table 4.3) after applying the hypoDD double-difference technique (Waldhauser et al. 2000) to the events from (a) resulting in a total number of 4407 events. The location of repeating earthquakes detected by Bohnhoff et al. (2017a) are marked with yellow stars. Regional abbreviations are like in Fig. 2.1. Areas coloured in green contain quarry blasts as cataloged by KOERI (http://www.koeri.boun.edu.tr/sismo/zeqdb/indexeng.asp, last visited 2016.10.13). Dense epicentral clusters in the catalogue of relocated events within these areas and having relatively shallow depth are likely to be quarries (small green patches in Fig. 4.8a – 4.11a).

lated for the remaining events, 1) for stricter catalogue qualities ('good' and 'best') and 2) for events located in the (entire) 'Marmara Region' as well as in sub-regions that correspond to the areas further investigated in cross-sectional volumes in the following section, namely the 'Marmara Section', 'Southern Shelf', 'Princes Island-' as well as 'Yalova-Hersek-Segment' and the Western Sea of Marmara (Fig. 4.5b). For each subset of magnitudes we performed a bootstrap re-sampling by repeating the calculation of M_c and b-value 1000 times on the basis of 75 % of the underlying magnitude population which was randomly sampled without replacement. The corresponding averages and standard deviations are summarized in Table 4.2 where M_c varies between 1.9 calculated for several subregions and 2.1 for the Marmara Section. This can be expected as the PIRES-network provides near-fault coverage while the Marmara Section is more distant to seismic stations. We obtain a reasonable b-value of $b = 1.24 \pm 0.05$ for the entire region and time period. Significantly larger b-values were measured for the Western Marmara (1.38) as well as for the Princes-Island- (1.59) and Yalova-Hersek-Segement (1.50). For the latter this could be related to a lower differential stress in that area, implying a normal fault regime, which is confirmed by the according focal mechanisms (Sec. 4.3.4, Fig. 4.12, Örgülü 2011; Kinscher et al. 2013; Öztürk et al. 2015). We can follow this line of argument for the Princes-Island-Segment by considering the two normal faulting events we here observe at its western tip (events 6 and 7 in Fig. 4.12. On the other hand, elevated b-values are also associated with areas of geological complexity and the activation of abundant small faults (Raub et al. 2017), such that the Princes-Island-Segment as described by Pinar et al. (2003) and the Western-Marmara containing the Ganos-Bend, could be such candidates.

Events contained in the categories of best, good or fair locations roughly constitute half of the events initially analysed. The remaining events were not located with sufficient precision and thus discarded from further processing and analysis. Fig. 4.5a indicates how application of stricter quality criteria discards particularly events with $M_w < 2.1$. Small events are likely to be recorded properly only by a local subset of the seismic stations, thus yielding too few picks to retrieve a stable hypocentre.

Old compared to new absolute locations The new locations achieve an improvement with respect to the initial hypocentres particularly in their horizontal distribution which shows less epicentral spread and sharper contours of seismically active clusters (Fig. 4.6a). The new distribution also creates more differentiated hypocentral depths (Fig. 4.6b–4.6c). Several of the initial hypocentres seem to have been located at fixed depth (at 7.5 km), a substantial portion being distributed in a narrow band around this depth and another in a more diffuse manner at greater depth. In contrast, the bulk of new hypocentres are generally located deeper than 7.5 km which is likely re-

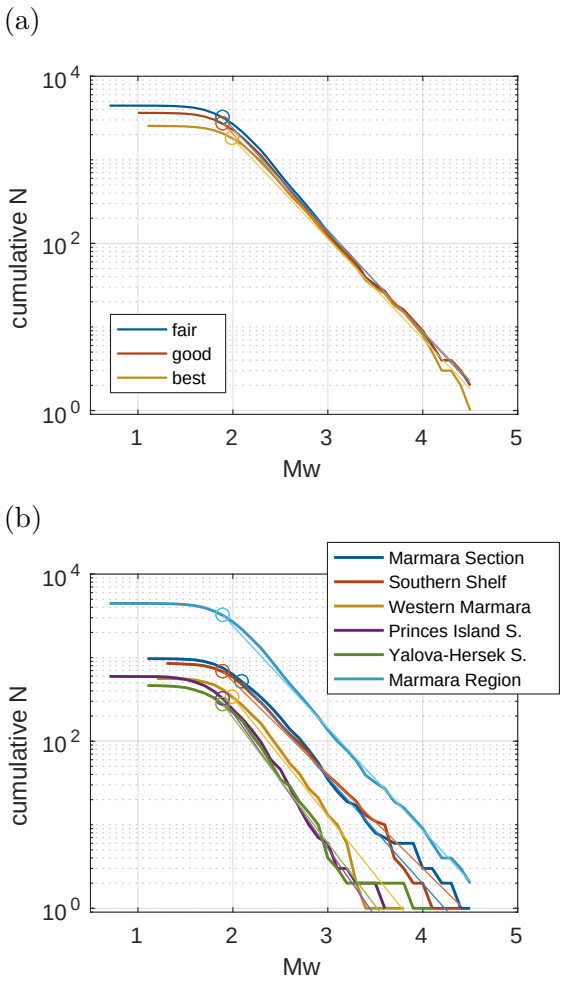

Figure 4.5.: Cumulative magnitude-frequency distributions of absolute locations (Fig. 4.4a), (a) for different catalogue qualities (Table 4.3) and (b) for different subregions. Shallow earthquakes inside areas likely containing quarries are not considered. The magnitude of completeness M_c and the b-value were obtained after bootstrap re-sampling and are marked by a circle and the slope of the straight, respectively. The numeric values of each are given in Table 4.2 together with references to maps showing the corresponding area.

Table 4.2.: Summary of magnitude frequency-statistics of absolute locations as illustrated by Fig. 4.5a and 4.5b for different catalogue qualities and subregions, respectively, obtained after bootstrap re-sampling. The subregions are those investigated in Sec. 4.3.2.

region		quality	N(events)	M_c	b-value	
Marmara Section	(Fig. 4.8b)	fair	971	2.1 ± 0.1	1.29 ± 0.08	Fig. 4.5b
Southern Shelf	(Fig. 4.8c)		853	2.0 ± 0.2	1.18 ± 0.09	
Western Marmara	(Fig. 4.11a)		563	2.0 ± 0.1	1.39 ± 0.10	
Princes Island S.	(Fig. 4.9c)		596	1.9 ± 0.1	1.59 ± 0.10	
Yalova-Hersek S.	(Fig. 4.9e)		463	1.9 ± 0.1	1.49 ± 0.11	
Marmara Region	(Fig. 4.4b)		4452	1.9 ± 0.1	1.25 ± 0.05	
Marmara Region	Fig. 4.4a	fair	4452	1.9 ± 0.1	1.24 ± 0.05	Fig. 4.5a
		good	3643	1.9 ± 0.1	1.23 ± 0.06	
		best	2544	2.0 ± 0.1	1.20 ± 0.02	

lated to the fact that the velocity model used in this study (Karabulut et al. 2011) is faster on average than that used for instance for the KOERI-locations (Karabulut et al. 2002). Some seismicity, however, has been moved closer to the surface. Yet, differences in this behaviour can be observed along the lateral extension of the two exemplary cross-sections. For instance at the Ganos bend which is situated offshore but near several coast lines, the seismic cloud delineates an EW dipping trend of the activity (from approximately 8 to 12 km) with some sparse events slipping to shallower depths. Further East, along the Marmara-Section around the Western-High (WH), near surface events seem to form systematic clusters of seismic activity. However, depth accuracy for shallow seismicity offshore is hampered by the here present sedimentary layers which are insufficiently reflected in the 1D-velocity model (Karabulut et al. 2011). Near surface seismicity can also be observed at onshore segments of the southern cross-section where it is likely to represent query blasts. These observations are discussed in further detail together with the corresponding relative relocations in the following section. Because some of the features discussed are obscured in Fig. 4.6 by the catalogue plotted second and the dislocation vectors, we provide the two shown sets of hypocentres separately in a flip-book like manner in the appendix (Fig. 4.15–4.16).

4.3.2. Spatial distribution of relocated hypocentres

The here presented seismicity catalogue of relative relocated earthquakes consists of 4774 events throughout the Marmara region covering the time interval 2006–2016. We consider 4407 events with small horizontal location uncertainty for further analysis, i.e. maximum extent of major axis of error ellipse $\leq 9\ km$ and maximum error ellipse area $\leq 25\ km^2$ (Fig. 4.4b). Within the catalogue of the best relative relocations, we identify events which likely constitute clus-

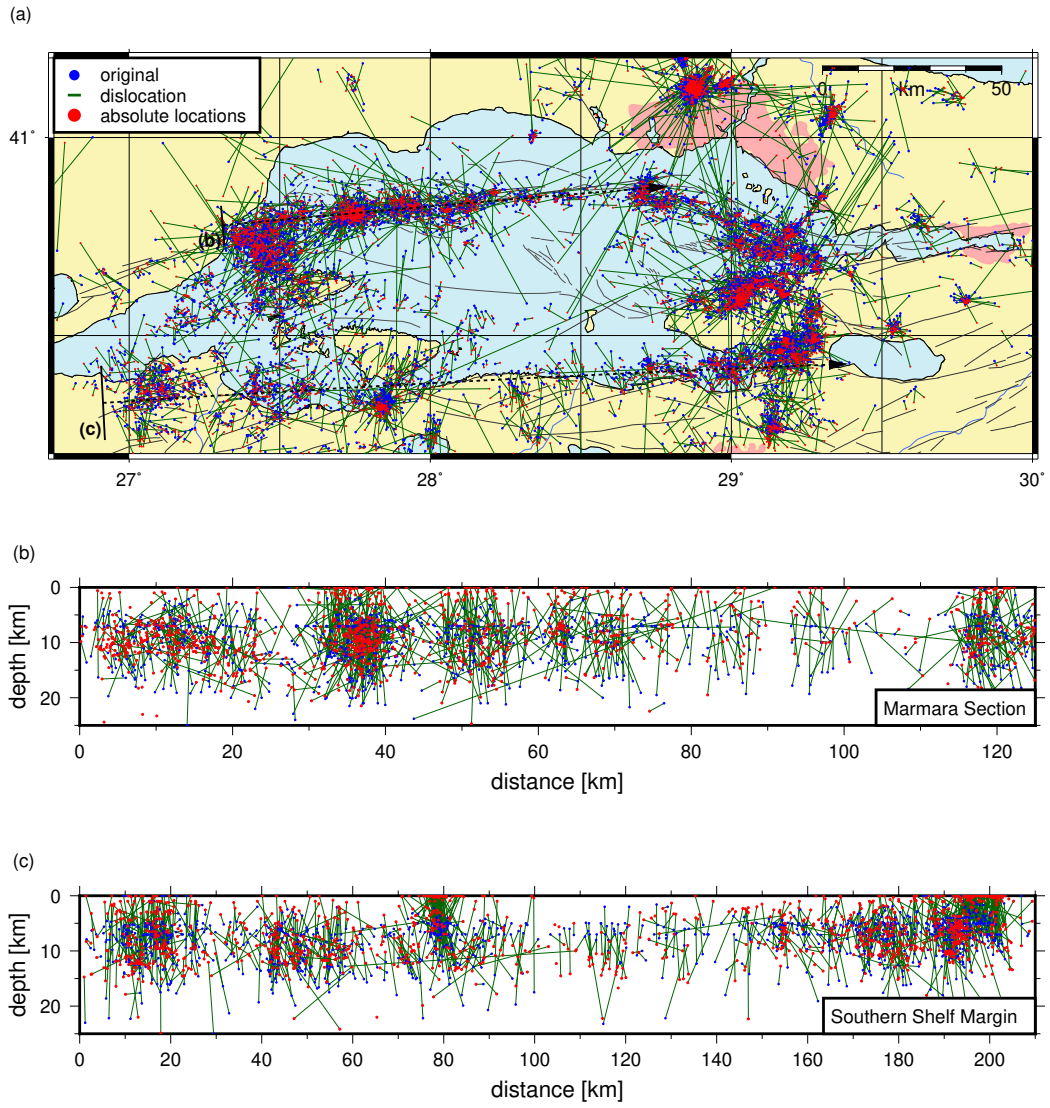

Figure 4.6.: Dislocation (green lines) of fair absolute locations (red dots) as calculated in this study, from the original locations of the merged catalogues (blue dots) in (a) map view and in cross sections along (b) the Marmara Section and (c) the Southern Shelf Margin. The comparison of both catalogues is also provided as flip-book in the appendix where the two sets of hypocentres are plotted separately (Fig. 4.15–4.16).

Table 4.3.: Different employed quality classifications and resulting number of relative relocations $N_{locations}$, based on the following criteria: maximum length of the error ellipse's major axis ($r_{major,max}$) and maximum area of the ellipse representing the horizontal location uncertainty ($A_{errEll,max}$).

	Quality	$N_{locations}$	$r_{major,max}$	$A_{errEll,max}$
1	very best	4407	9km	25 km^2
2	all	4657	inf km	inf km^2

ters of quarry blasts. These clusters were defined by means of a density based clustering analysis (DBSCAN Ester et al. 1996), where a quarry-cluster had to consist of at least three events within 800 m epicentral distance and its centroid had to be situated in one of the areas previously constructed on the bases of the quarry-blast catalogue provided by KOERI (Fig. 4.4). The green shaded areas shown in Figures 4.8a – 4.11a were finally obtained by joining the 1.2 km neighbourhoods of events that were members of the obtained clusters. Generally events within these areas are characterized by shallow hypocentral location, presumed as quarry blasts and discarded from further discussion.

Absolute compared to relative (re-)locations With respect to the absolute locations, the relative relocations achieve further compaction and sharpening of seismic clusters in the horizontal (Fig. 4.7a). This is equally true for the vertical distribution although with less precision as compared to the horizontal. Nevertheless trends of the seismic cloud as well as sharp contours of some sub-clusters within it become visible (Fig. 4.7b–c). Generally, since the relative relocation initially relies on pairs of nearby seismicity, isolated seismic events are often discarded by the procedure. This mostly affects areas far from the core activity spots like for instance the water area in the middle of the Sea of Marmara. We further discuss the initial, absolute and relative (re-) locations in selected areas in the following paragraphs. The two sets of hypocentres shown in Fig. 4.7 are also provided separately in a flip-book like manner as electronic supplement in order to make visible features otherwise obscured by the dislocation vectors and the second layer of hypocentres (Fig. 4.17–4.18).

Central Marmara Section and Southern Marmara Shelf The majority of events are aligned offshore along the northern Marmara Section, extending between the Ganos fault in the west and the Central Basin in the east, and further eastward offshore of Istanbul along the Princes' Islands segment and a fault aligned parallel to the northern coast of the Armutlu Pensinsula and running towards the Imrali Basin, the Yalova-Hersek segment (Pinar et al. 2001, Figures 2.1 and 4.8a). The Marmara Section as the seismically most active strand is part of the main northern NAFZ branch and hosts the largest

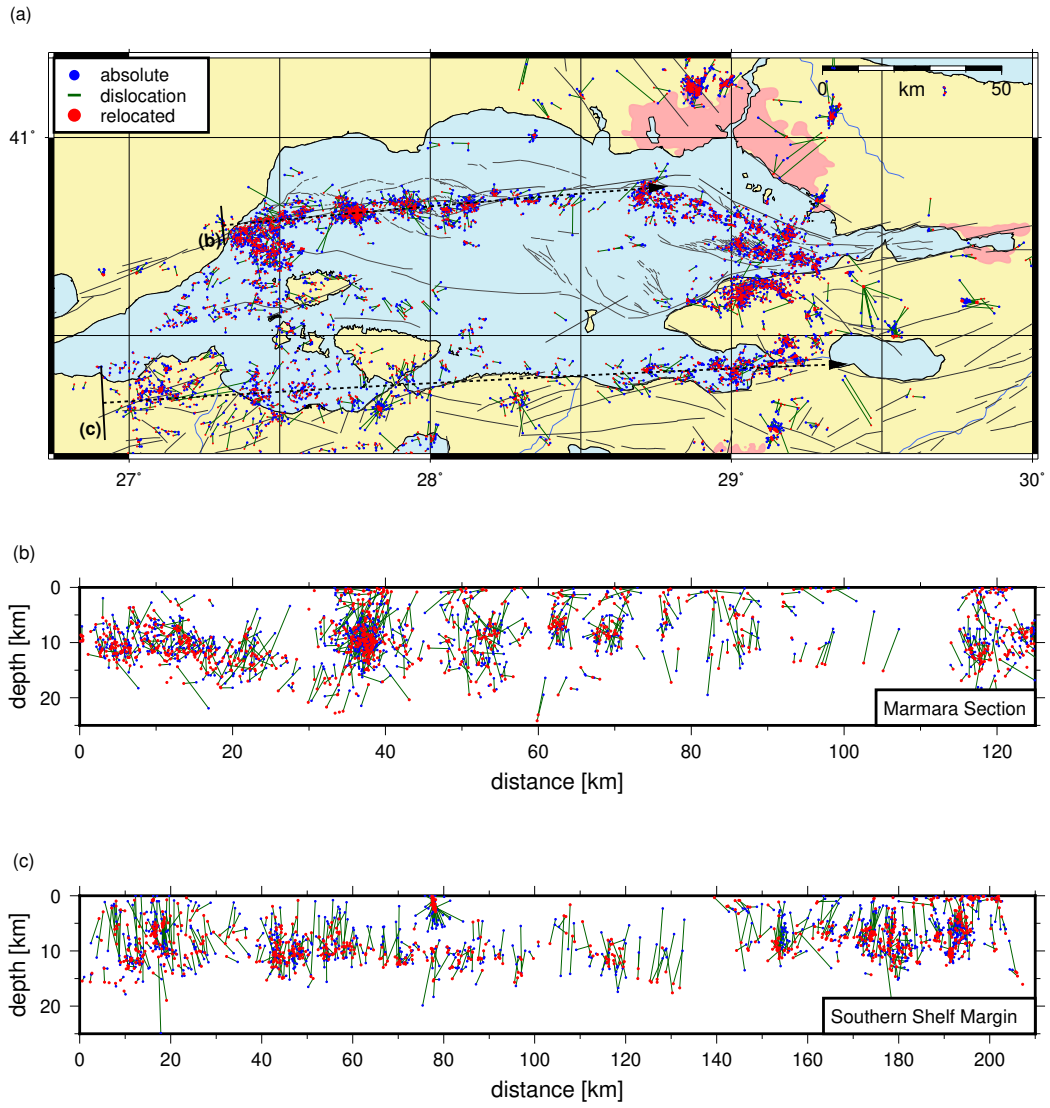

Figure 4.7.: Dislocation (green lines) of relative relocations (red dots) from absolute locations (blue dots) in (a) map view and in cross sections along (b) the Marmara Section and (c) the Southern Shelf Margin. The comparison of both catalogues is also provided as flip-book in the appendix where the two sets of hypocentres are plotted separately (Fig. 4.17–4.18).

part of the relative plate motion, on the order of 10–15 mm/yr (Hergert et al. 2010; Ergintav et al. 2014). In first order approximation its trajectory through the Sea of Marmara is composed of succeeding straight segments delineated by coherent seismic activity and interrupted by several seismically less active – or entirely inactive – portions or spots. We refer to this later in the text. The width of the seismicity band is a few tens of kilometres on average with local variations. Whereas the transform fault character of the NAFZ suggests that the Marmara Section is a near-vertical fault, the verticality of the fault would imply that a substantial part of the activity is occurring off the main branch on secondary and/or splay faults. Such features have been observed earlier along the Princes' Islands segment with bursts of activity migrating along a splay fault (Bulut et al. 2011). The second coherent seismically active feature seen in the epicentral distribution is pronounced activity along the Southern Marmara Shelf representing the northern part of the southern NAFZ branch (Figs. 2.1 and 4.8a). There, the activity level is lower and events are less spatially clustered compared to the Marmara Section in the north.

The hypocentral depth of the seismicity generally extends from a few kilometres down to 16–18 km throughout the Marmara region. The depth distribution along the Marmara Section allows to identify systematic lateral variations of the hypocentral distribution (Fig. 4.8b). We highlight the trend of the lower bound of the seismogenic layer with an upper and lower estimate of the same, by calculating the depth down to which 85 – 95 % of the seismicity occurs in lengthwise equally long intervals. We applied this procedure to all cross sections (Figures 4.8 – 4.11), where the number of intervals a cross-section was divided into, was chosen such that every interval contained at least one event. The resulting values were locally averaged with a running mean. The activity spots west of the Tekirdak Basin (TB) and below the Western High (WH) show activity down to the base of the seismogenic layer (∼18 km) (Fig. 4.8b). The here reported depths are generally consistent with previous values reported by Schmittbuhl et al. (2015). Only slight discrepancies can be observed in comparison with Yamamoto et al. (2017), who determine deeper hypocentres and vanishing shallow seismicity below the Western High (WH) using ten months of OBS data recorded immediately above the seismicity. Seismicity clusters and quiescent areas marked by Yamamoto et al. (2017) can also be identified in our catalogue, indicating that there are no short-term spatio-temporal variations existing in the study area during the 10 years of observation except in shallow sedimentary layers where gas emissions have been reported (Tary et al. 2011) and seismicity there has been identified as after shocks to $M > 4$ earthquakes (Cros et al. 2013). We find a similar trend of the lower boundary for the depth of seismic activity as Yamamoto et al. (2017) It becomes shallower towards the east, starting from a minimum of ∼18 km depth below the Western High, and passing the Central Basin (CB), it reaches down to ∼12 km only below the Kumburgaz Basin (KB) (Fig. 4.8b). In contrast, hypocentral depths east

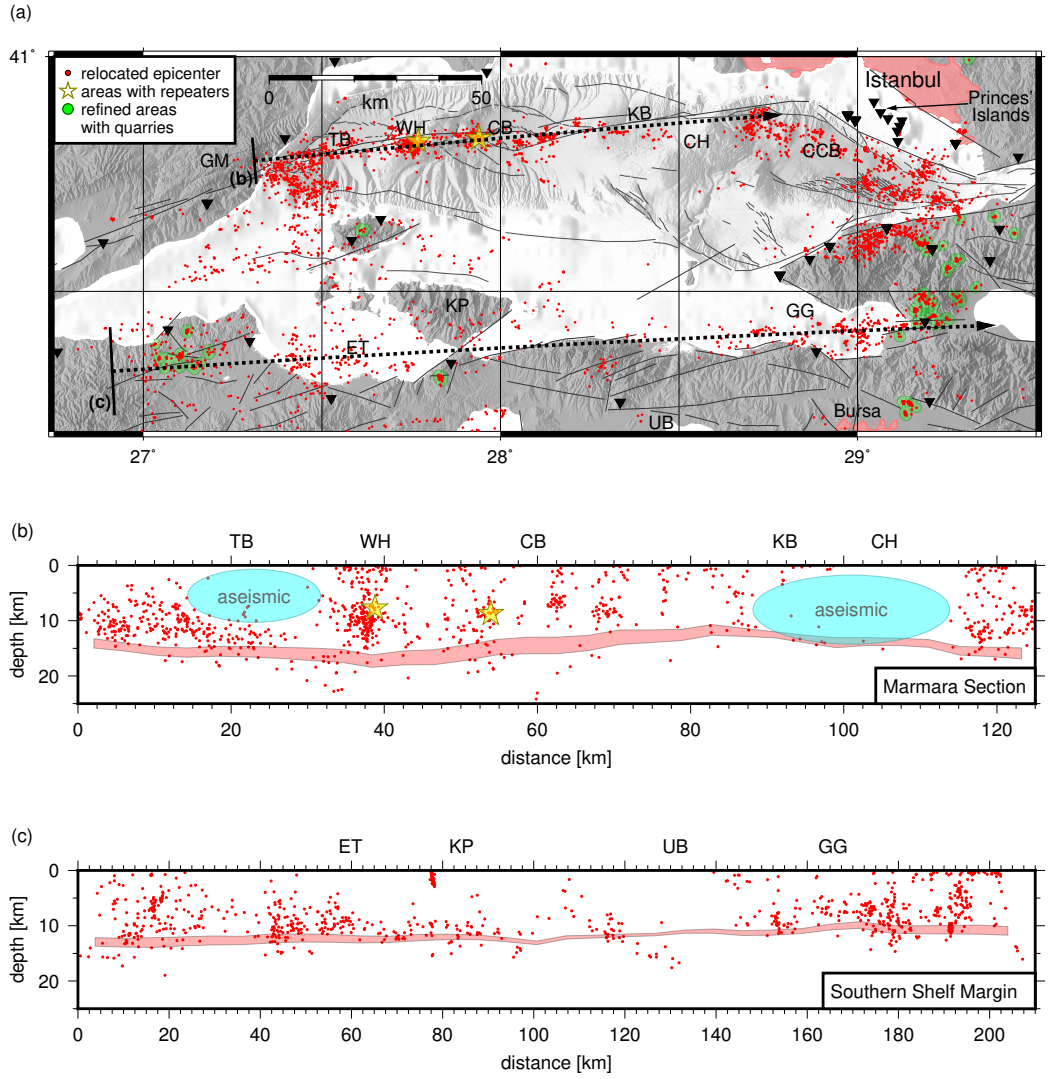

Figure 4.8.: (a) Epicentre map with the surface projections of two east-west trending vertical cross sections containing the seismicity shown in (b) and (c). The extent of the volume included in a cross section is delineated by the dashed black lines where the volume's width is indicated by the orthogonal line at its beginning and the orientation of the cross section by the arrowhead at its end. Areas coloured green contain dense epicentral clusters likely corresponding to quarry blasts. b) Depth section along the main northern NAFZ branch below the Sea of Marmara between the Ganos fault and the Istanbul bend. The light-red band delineates the base of the seismogenic layer (see section 4.3.2 for details). (Caption continues on the next page.)

Figure 4.8.: (Continued caption from previous page.) Cyan coloured ellipses indicate aseismic patches of the fault. Abbreviations indicate geographical features as in Fig. 2.1 and are orthogonally projected onto the central line of the cross section for better orientation. c) Depth section along the main southern NAFZ branch along the southern shore of the Sea of Marmara coinciding with the Southern Shelf Margin.

of the Central High drop to almost 20 km again (Fig. 4.8b). The Cinarcik Basin (CCB) shows activity down to ∼18 km. Most interestingly, there are two well-defined aseismic patches that show the same characteristics as those recently reported along the Princes' Islands segment (Bohnhoff et al. 2013) and along the combined Izmit-Düzce rupture (Bohnhoff et al. 2016a). The first aseismic patch extends from the surface down to ∼10 km and is located between the Tekirdak Basin and the Western High (Fig. 4.8b). The second, located further east below the Central High, even extends down to the base of the seismogenic crust. On the basis of the new absolute hypocentres, both aseismic patches are characterized by sparse seismicity (Fig. 4.6). Whereas this holds true from the perspective of the original locations for the second aseismic patch, the first is not visible here (Fig. 4.7). These aseismic patches are of particular interest as they may represent either creeping segments or locked fault asperities and thus potential nucleation points of future ruptures (Bohnhoff et al. 2013, 2016a). Two doublets of earthquake repeaters were previously found in the vicinity of the Western High and Central Basin (yellow stars in Fig. 4.8a and 4.8b) (Bohnhoff et al. 2017a) and they were interpreted to indicate fault creep. However, they appear to be located outside of the here reported aseismic patches. This would imply that there is no indication for creep along the two aseismic patches. They thus can be considered to reflect locked patches of the main NAFZ branch below the Sea of Marmara, thereby representing potential nucleation points of future earthquakes in this region.

The hypocentral depth along the Southern Marmara Shelf is generally slightly shallower than along the Marmara Section and it shows a consistent lower boundary at ∼14 km (Fig. 4.8c). Lateral variations from west to east are smoother than along the Marmara Section but still do allow to identify active portions throughout the seismogenic layer in the western half (km 0–100 in Fig. 4.8c) and in the east (km 150–200) and a nearly-aseismic patch around the Uluabad Basin. Since there is less consensus on whether the Southern Marmara Shelf represents a coherent NAFZ fault branch similar to the Marmara Section in the north, we do not further interpret the tectonic role of this aseismic portion.

Eastern Sea of Marmara The seismicity distribution in the eastern Sea of Marmara is shown in Figure 4.9. There, the NAFZ branches into two main fault strands, the Princes' Islands segment in the north and Yalova-Hersek

segment in the south. Both strands bound the pull-apart Cinarcik Basin depocentre which is a half-graben structure with a sedimentary thickness on the order of 3–4 km (Le Pichon et al. 2001; Karabulut et al. 2002; Acarel et al. 2014). The epicentral distribution in this region allows to identify pronounced seismicity along both fault strands with a lateral extension across the fault on the order of ∼20 km. Both strands were recently shown to merge towards a single master fault below the base of the seismogenic layer (Bohnhoff et al. 2013). In order to separate on-fault from off-fault seismicity we plot vertical transects of two different widths along the Princes' Islands segment (Fig. 4.9b + 4.9c) and along the Yalova-Hersek segment (Fig. 4.9d + 4.9e). For the Princes' Islands segment we identify and confirm the existence of a ∼10 km deep and 40 km long aseismic patch with a slightly deeper extend at its western part (Fig. 4.9c). This feature is clearly visible also among the new absolute locations but obscured in the merged catalogue by the concentration of seismicity at 7.5 km depth (appendix Fig. 4.15–4.19). The Imrali Basin is entirely inactive while the Yalova-Hersek segment hosts an aseismic patch down to 10 km (Fig. 4.9e). The latter is interpreted to reflect a potential fault asperity similar to that identified along the Princes' Islands segment.

Depth transects perpendicular to the Princes' Islands segment are shown in Fig. 4.10. They confirm that the actual main fault branch (indicated by thick magenta coloured line in Fig. 4.10a) is seismically inactive from the Istanbul bend in the west until 20°10'E longitude in the east (Figs. 4.10c – 4.10e). Assuming a southward near vertical dip, some dense seismic activity occurs only near the bottom of the seismogenic layer. West of longitude 29°10' other seismicity along these transects is predominantly observed further south-west and off the presumable fault-plane. The phenomenon of abundant off-fault seismicity has been recently reported for the San Jacinto Fault, California (Ross et al. 2017). For this seismicity to occur on the main fault, the Princes' Islands segment would need to have a dip of nearly 45° from the mapped location of its fault escarpment. Beyond longitude 29°10' (and particularly at the site crossed by profile (f)) the seismicity extends to both sides of the fault. However, the calculated focal mechanisms of earthquakes located west of the Istanbul bend (Fig 4.12, focal mechanisms 4 and 5) suggest fault planes oriented rather parallel to the Princes' Islands segment indicating extensional off-fault structures. Örgülü (2011) describe the Cinarcik Basin as a mature basin in which a through-going fault has developed only recently from "coalescence of short strike-slip segments in en-echelon form". Possibly the formation is not yet fully concluded and the formation process is continued a few km further south of the mapped fault escarpment.

Western Marmara Seismicity along the western Marmara Section is shown in Fig. 4.11. While the onshore Ganos fault does not show any seismicity, in good accordance with earlier findings of a locked status there (Fig. 4.11a)

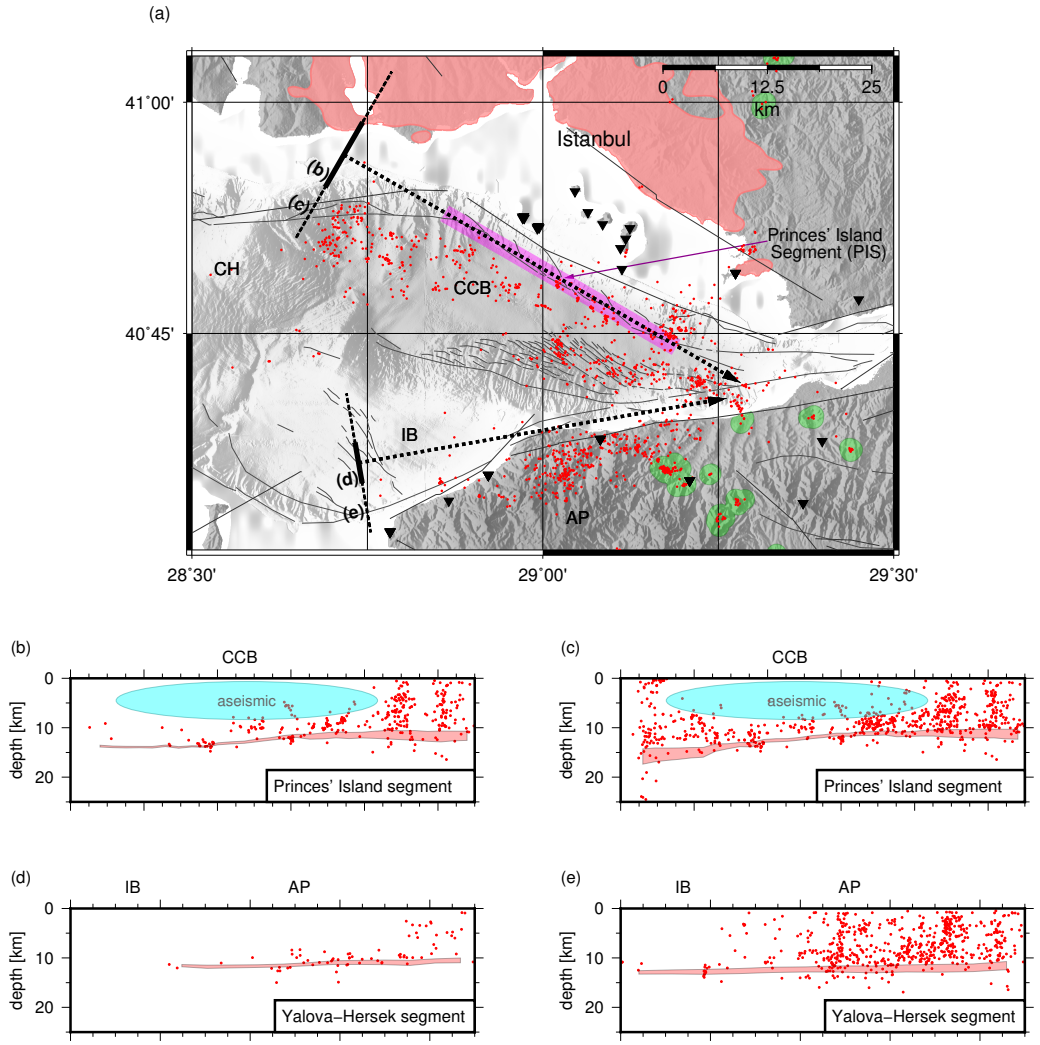

Figure 4.9.: (a) The epicentre map for the eastern Sea of Marmara delineates the surface projections of the vertical cross sections shown in (b)–(e) using the same symbolic scheme as in Fig. 4.8. The fault escarpment of the Princes' Islands segment (PIS) is marked in magenta. (b) and (c) Cross sections along the Princes' Islands segment between the Istanbul bend and the western termination of the 1999 Izmit rupture with increasing width of the cross-sectional volume. The cyan coloured ellipse marks an aseismic patch. (d) and (e) Yalova-Hersek segment at the southern margin of the Imrali Basin, with increasing width of the cross-sectional volume.

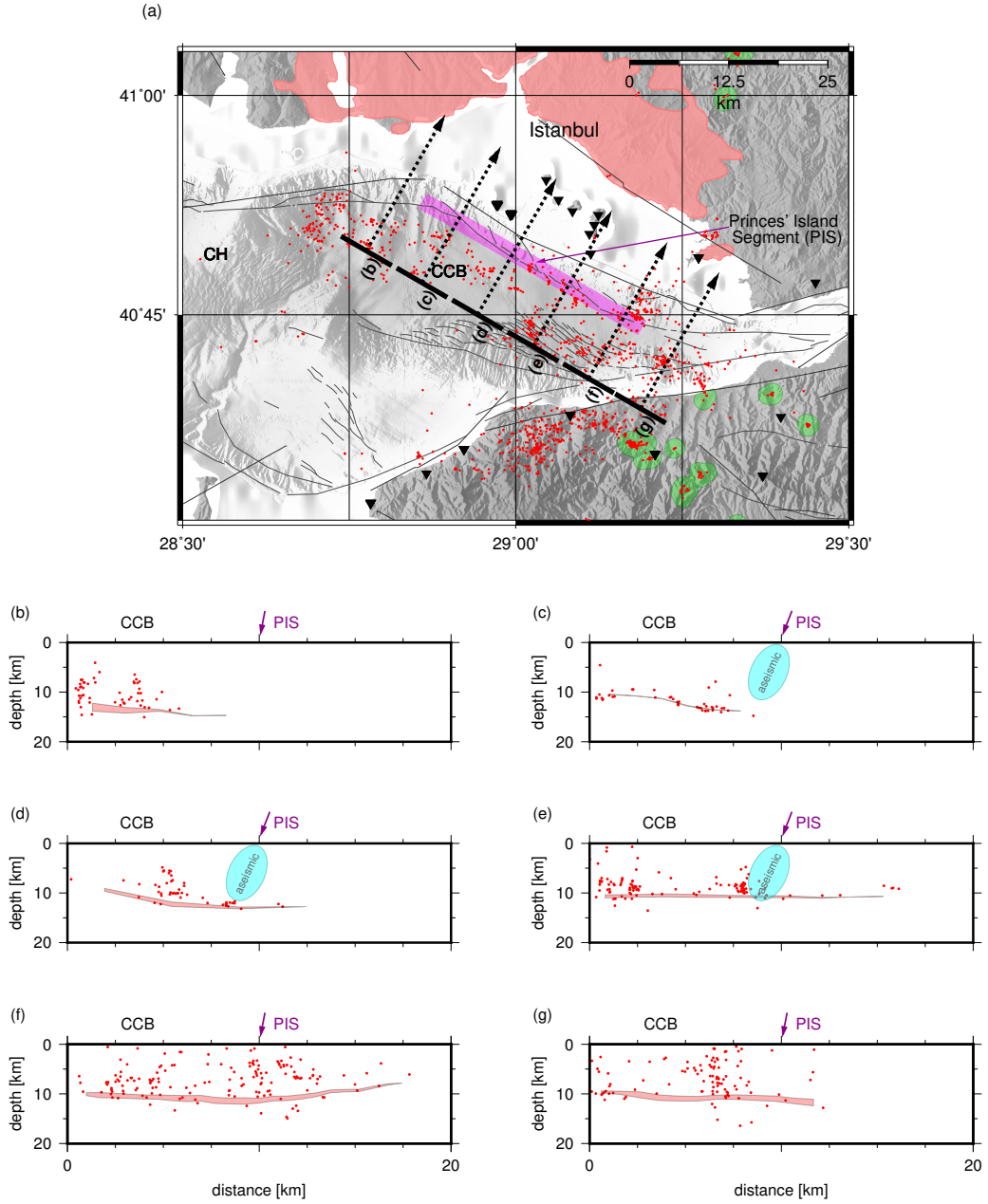

Figure 4.10.: (a) Epicentre map with the surface projections of the vertical cross sections shown in (b)–(g) (cross sections and other symbols as in Fig. 4.8) where the latter orthogonally strike through the Princes' Islands segment (PIS, also see Fig. 4.9) and are sorted from West to East. The magenta coloured arrow indicates the presumable fault's surface expression and dip (plotted to correspond 80°, note that the angle seems smaller due to the aspect ratio of the figure). The cyan coloured ellipse marks an aseismic patch.

(Motagh et al. 2007), the offshore portion west of the Tekirdak Basin does show activity throughout the seismogenic layer with an aseismic patch down to 10 km below the Tekirdak Basin itself (Fig. 4.11b). This is in agreement with findings from Yamamoto et al. (2017). The depth section across the fault (Fig. 4.11d) indicates that actually most of the activity is diffuse off-fault activity raising the question whether the actual fault might be aseismic as well and the seismicity reflects activation of minor branches and splay faults. The sparse seismicity along the Southern Marmara Shelf does not allow to clearly discriminate seismically active from inactive patches.

4.3.3. Identification of locked and creeping fault sections

Locked patches Based on the spatial distribution of seismicity along the Marmara Section as the main NAFZ fault branch extending along the northern Sea of Marmara we can refine the previous understanding of their current nature of deformation (locked versus creeping). Recent seismological and geodetic investigations support the view that the northern branch of the NAFZ, the Marmara Section, currently hosts both locked and creeping fault sections. The onshore Ganos fault immediately to the west of the Sea of Marmara where a M7.4 earthquake occurred in 1912 is currently locked (Motagh et al. 2007; Ergintav et al. 2014; Klein et al. 2017). This is in good agreement with our results where dominant off-fault seismicity is observed around the Ganos segment (Fig. 4.11b). Likewise, there are strong indications that the same is true for the Princes' Islands segment offshore Istanbul (Bohnhoff et al. 2013; Ergintav et al. 2014), where the seismic gap down to 10 km depth as reported earlier is confirmed by the here presented hypocentre catalogue.

While the western and eastern portions of the Marmara Section of the NAFZ are comparatively well studied, less information exists for the central part. This is due to the previously less dense distribution of permanent seismic stations there and due to the absence of islands to the south of the fault, preventing from obtaining near-fault GPS measurements. Several aseismic patches previously observed during a ten month long OBS-campaign (Yamamoto et al. 2017) can be confirmed to be quiescent over the entire observational period of ten years of this study. Whereas these features are very prominent in our relocated catalogue and can partially also be identified in the catalogue of new absolute locations, the abundant occurrence of seismicity at a fixed depth of 7.5 km in the merged original locations prevents the sight on most of them there. Furthermore, first results from sea-floor based deformation measurements from acoustic extensometers also seem to favour a locked over a creeping status for the Istanbul-Silivri fault segment / Kumburgaz Basin west of Istanbul (Sakic et al. 2016) and below the Western High (Yamamoto et al. 2016).

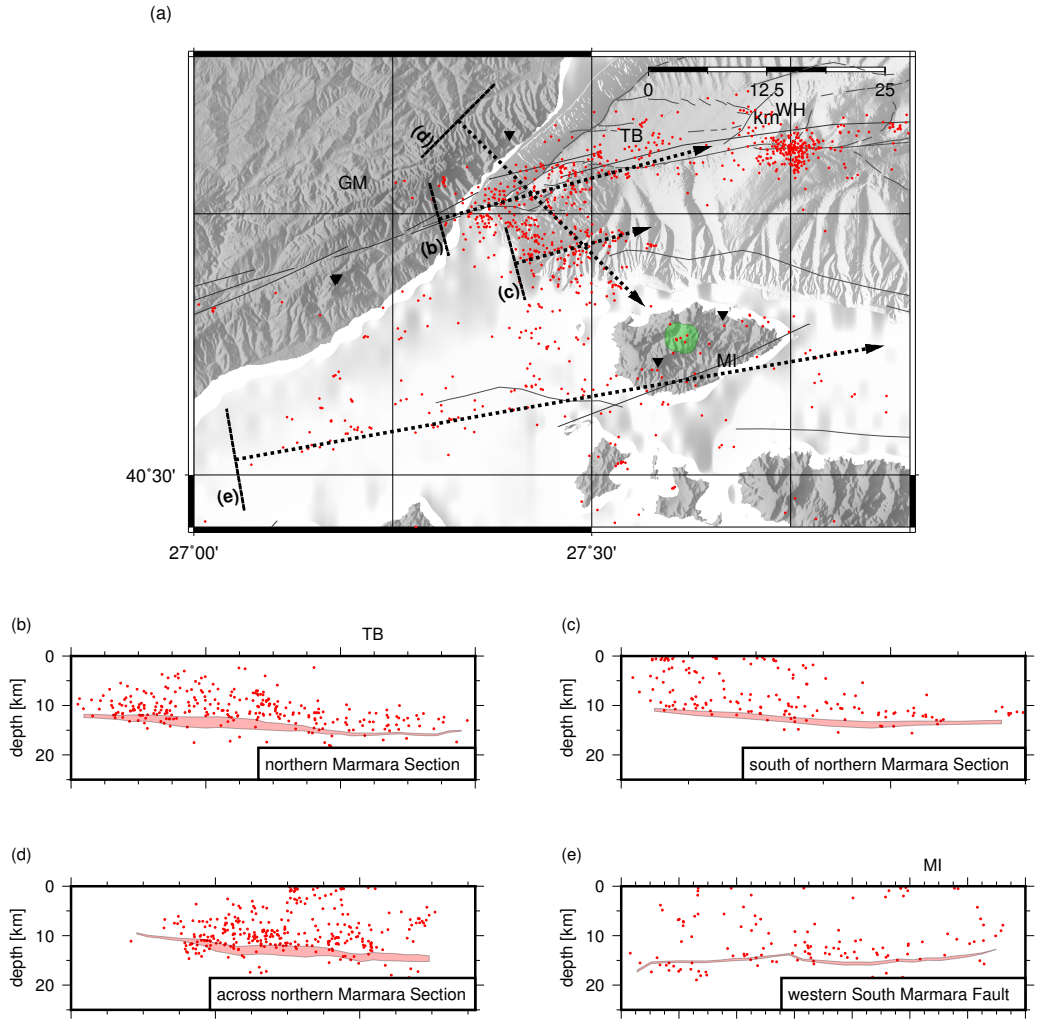

Figure 4.11.: (a) Epicentre map for the western Sea of Marmara at the termination of the Ganos fault with the surface projections of the vertical cross sections shown in (b)–(e) (cross sections and other symbols as in Fig. 4.8). (b) Western end of the Marmara Section of the northern NAFZ branch coinciding the eastern termination of the 1912 Ganos rupture (Armijo et al. 1999). (c) Seismicity between the Marmara Section of the northern NAFZ branch and the South Marmara Fault (Le Pichon et al. 2014). (d) Cross section cutting through the seismicity depicted in (b) and (c). (e) Seismicity at the western end of the South Marmara Fault.

Table 4.4.: Table relating colour of compressional quadrant of beachballs in Fig. 4.12 to respective fault plane uncertainty (ΔFP, last column in Table 4.5) in degrees. $N(FP)$ is the count of fault planes assigned to a certain uncertainty category.

ΔFP	$< 20°$	$< 25°$	$< 35°$	$< 45°$	$\geq 45°$	total	
color							
$N(FP)$	2	9	28	4	3	46	Fig. 4.12)
$N(FP)$	2	8	47	56	27	140	Fig. 4.13)

Creeping patches However, there are also strong indications for creeping sections below parts of the western Marmara Section based on the observation of repeating earthquakes and small b-values around the Central Basin and the Western High (Schmittbuhl et al. 2016; Yamamoto et al. 2016; Bohnhoff et al. 2017a) where creep rates might locally accommodate as much as 25–75% of the plate deformation (Bohnhoff et al. 2017a). The limitation of repeating earthquakes to the Western High and Central Basin regions establishes a focus on the adjacent areas, i.e. the edges of the central Marmara Section, namely the Tekirdag Basin and the Kumburgaz Basin/Central High region, where larger aseismic patches indicate potentially locked fault segments.

4.3.4. Focal mechanisms

Based on the here presented 10-year seismicity catalogue, we also determine single-event focal mechanism solutions for the largest events in order to study the kinematic setting along the principal NAFZ fault branches below the Sea of Marmara. We use the automatically determined P-wave first-motion polarities to calculate a total of 140 focal mechanisms which were calculated for events located with ≥ 20 P-picks containing ≥ 18 P-wave first motion polarities, ≥ 12 S-picks, azimuthal gap $\leq 90°$, area of error ellipse $\leq 25\ km^2$, focal depth in the range of [4, 20] km and magnitude $M_w \geq 2.7$. The inversion was performed with the HASH software (Hardebeck et al. 2002). The epicentres of all focal mechanisms and 46 beach-balls are shown on a map of the region in Fig. 4.12 together with selected focal mechanisms previously published (Örgülü 2011; Öztürk et al. 2015). The P- and T-axis distribution of all solutions is displayed on a stereographic projection of the lower hemisphere in Fig. 4.13. Our focal mechanism solutions were divided into four categories of quality according to table 4.4.

The spread of fault-plane uncertainties is large ($13° < \Delta FP < 53°$), the average fault plane uncertainty being 37°. The behaviour of the uncertainty cannot be unambiguously linked to one cause or parameter. Additionally to the fault-plane uncertainty (in degrees as returned by HASH), we also consider the number of first-motion polarities inverted as a proxy for a focal mechanisms quality (Table 4.4). However, there is a large spread in the correlation of these

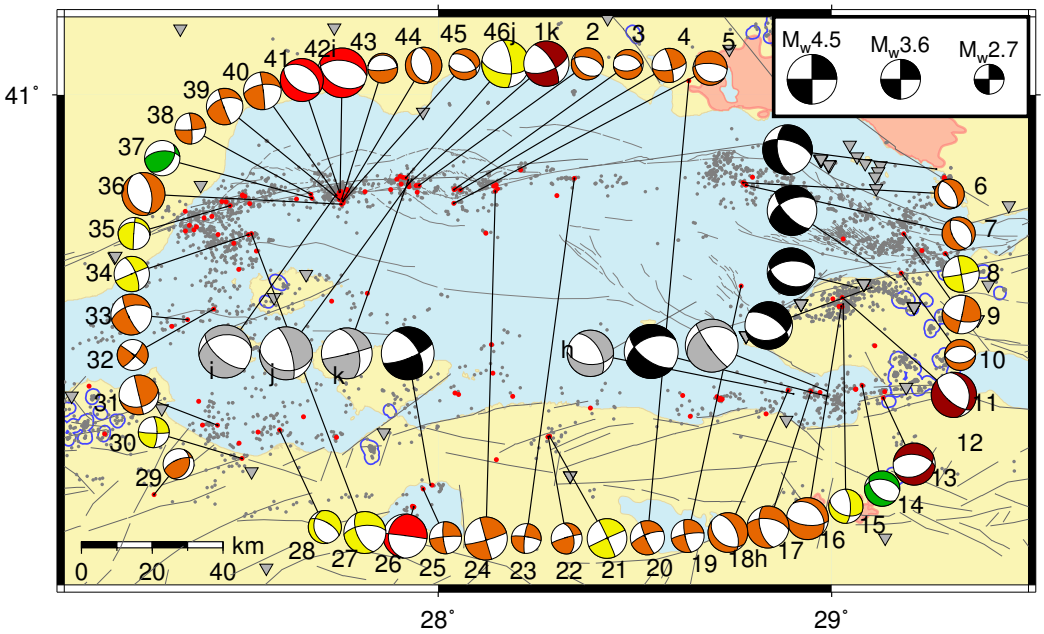

Figure 4.12.: Location of 140 events from Fig. 4.13 (their P- and T-axis on lower hemisphere) displayed by red circles and focal mechanism solutions for 46 relocated events with moment magnitude $2.7 \leq M_w \leq 4.5$ (from the 140 solutions, the 6 largest events and out of the remaining, the 40 best; also see Table 4.5). The beachball size corresponds to the magnitude. Relocated seismicity (from Fig. 4.4b) is marked by grey dots. The focal mechanisms were chosen according to their solution quality and magnitude (see Section 4.3.4 for details). The colour of the compressive quadrants, green, yellow, orange and red, indicate decreasing quality of a focal plane solution (see Table 4.4 for the corresponding interval of fault plane uncertainty in degrees). Black and grey focal planes are from Örgülü (2011) and Öztürk et al. (2015), respectively.

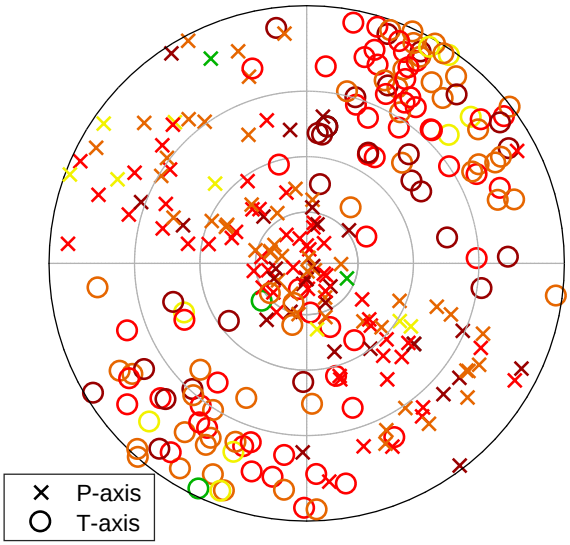

Figure 4.13.: P- and T-axis of 140 fault-plane solutions plotted on a stereographic projection of the lower hemisphere and symbolized by crosses and open circles respectively. The P- and T-axis are colour encoded according to the quality of the corresponding fault-plane solution (also see Table 4.4). The epicentres of the corresponding events are highlighted in Fig. 4.12.

two parameters (as well as in the correlation between magnitude and number of first-motion polarities). Apart from falsely picked first-motion polarities, this is likely because the coverage of the focal sphere is not optimal in general and also it varies strongly in between events. However, the inversion scheme is very sensitive to the coverage as well as to the orientation of the true underlying focal plane. For the method employed here smaller uncertainties would first of all require a complete coverage of the focal sphere particularly at its poles. Four of our focal mechanism solutions have been previously determined by Öztürk et al. (2015) too (focal plane # $= 1, 18, 42$ and 46, also see Table 4.5). The pairs of solutions are congruent. Detailed depiction of our solutions to three previously calculated focal-mechanism solutions, including first-motion polarities and P- and T-axis of all "acceptable solutions" (Hardebeck et al. 2002) are shown in Fig. 4.14a, 4.14c and 4.14d.

The analysed earthquakes display predominantly near horizontal SW-NE striking T-axis, most P-axis spreading along a band striking NW-SE (Fig. 4.13). This corresponds to focal mechanisms predominantly ranging in the strike-slip and normal faulting regime with no clear dependence on their magnitude, confirming the earlier findings of a primarily transtensional regime in the larger Marmara region (Armijo et al. 1999; Le Pichon et al. 2001; Bohnhoff et al. 2006). This observation holds for the NAFZ northern branch from the Western High eastwards to the rupture area of the 1999 Izmit earthquake as well as along the Southern Shelf Margin west of the Gemlik Bay (Fig. 4.12). The fact that no spatially isolated pure strike-slip or normal faulting segments

Table 4.5.: Table of earthquakes for which focal plane solutions are presented in Fig. 4.12 where they can be identified by the index given the first column (#). The fault plane uncertainty and the number of first-motion polarities used to calculate the focal plane solution are given in the last two columns, ΔFP and $N(FM)$, respectively. Focal plane solutions that can also be found in Öztürk et al. (2015) are highlighted in dark grey.

#	eventID	origin time	M_W	longitude	latitude	depth	strike	dip	rake	ΔFP	N(FM)
1	2013331000004	2013.11.27 04:13:37	4.1	27.9250	40.8290	9.00	70	62	-155	53	39
2	2016084000000	2016.03.24 08:04:59	2.9	27.9517	40.8255	8.34	285	56	-107	31	21
3	2010064000003	2010.03.05 17:31:55	2.7	28.0405	40.8173	7.47	82	54	-108	28	22
4	2008204000001	2008.07.22 10:04:01	3.1	28.0563	40.8168	9.00	80	67	-170	30	19
5	2016030000000	2016.01.30 09:03:14	3.1	28.0397	40.7910	11.02	274	67	-103	30	27
6	2015320000004	2015.11.16 16:36:25	2.7	28.7748	40.8308	8.90	330	60	-90	31	27
7	2015320000006	2015.11.16 17:04:13	3.0	28.7820	40.8260	9.57	316	33	-105	26	26
8	2015225000001	2015.08.13 01:01:29	3.3	29.2888	40.6938	11.97	80	87	-179	20	36
9	2008296000001	2008.10.22 01:00:36	3.5	29.1827	40.7320	9.40	104	62	-177	31	23
10	2009193000000	2009.07.12 06:59:12	2.8	29.1765	40.6563	11.19	88	47	-89	31	20
11	2008072000002	2008.03.12 18:53:32	4.1	29.0267	40.6087	13.74	132	64	-110	48	23
12	2011020000000	2011.01.20 02:09:37	3.8	29.8102	40.6945	14.70	292	68	178	42	24
13	2013229000001	2013.08.17 18:16:31	3.8	29.1310	40.4140	9.00	67	42	-113	56	27
14	2015339000005	2015.12.05 20:53:52	3.2	29.0773	40.4383	12.21	277	46	-116	19	42
15	2009011000001	2009.01.11 06:07:19	3.1	29.0290	40.5960	1.31	110	47	-149	21	25
16	2008279000000	2008.10.05 06:04:05	3.8	29.0242	40.5920	12.72	96	64	-111	30	22
17	2010162000001	2010.06.11 10:56:45	3.8	28.9468	40.4268	9.74	278	57	-143	30	23
18	2011228000001	2011.08.16 17:30:07	3.6	28.8890	40.4288	7.62	126	37	-113	27	26
19	2010013000001	2010.01.13 03:54:52	3.0	28.7700	40.6310	11.37	260	80	-167	29	31
20	2012293000000	2012.10.19 08:17:25	3.1	28.6370	41.0270	11.57	249	73	-172	31	26
21	2009213000003	2009.08.01 16:42:39	3.6	28.2832	40.3395	12.80	246	88	177	23	30
22	2009214000001	2009.08.02 01:21:08	2.8	28.2797	40.3387	12.19	254	84	142	31	35
23	2008203000000	2008.07.21 00:32:24	2.7	28.3460	40.8390	11.69	278	80	-170	28	23
24	2010276000003	2010.10.03 17:49:04	3.9	28.1455	40.8143	10.78	74	84	179	28	36
25	2011214000001	2011.08.02 04:42:30	2.9	27.9618	40.2370	13.55	265	85	-169	31	23
26	2014184000001	2014.07.03 05:04:46	4.0	27.9380	40.2017	11.92	277	89	-115	43	58
27	2009117000004	2009.04.27 19:03:07	3.8	27.5258	40.7322	15.60	265	62	-144	24	38
28	2016095000000	2016.04.04 16:31:29	3.0	27.5972	40.3520	10.19	300	66	-115	24	18
29	2015355000000	2015.12.21 01:16:00	2.8	27.2780	40.2260	14.95	247	66	112	30	25
30	2014253000008	2014.09.10 22:33:41	2.8	27.5017	40.2963	10.10	92	84	-162	25	23
31	2008197000000	2008.07.15 09:19:49	3.6	27.4393	40.3610	14.82	76	40	179	29	26
32	2010149000000	2010.05.29 02:05:58	2.8	27.4297	40.5865	14.48	308	86	167	27	29
33	2010365000002	2010.12.31 20:57:37	3.7	27.3632	40.5658	15.28	254	55	-165	29	31
34	2016088000007	2016.03.28 17:23:47	3.2	27.5182	40.7303	14.21	247	89	161	22	27
35	2014281000001	2014.10.08 03:08:50	2.9	27.4715	40.7865	17.42	277	30	-176	24	24
36	2009024000007	2009.01.24 15:58:40	3.9	27.7547	40.7892	14.90	149	32	-108	27	44
37	2010299000004	2010.10.26 22:09:41	3.2	27.6792	40.8008	10.78	265	57	119	14	30
38	2013289000001	2013.10.16 12:53:43	2.8	27.6767	40.8080	18.40	86	83	-172	31	26
39	2011206000020	2011.07.25 20:43:53	3.3	27.7490	40.7978	9.38	253	53	-175	28	29
40	2009077000008	2009.03.18 16:33:38	3.4	27.7420	40.8058	9.40	261	63	176	27	39
41	2015301000001	2015.10.28 16:20:03	3.9	27.7495	40.8122	11.79	308	39	-86	43	39
42	2011206000001	2011.07.25 17:57:21	4.5	27.7508	40.8132	11.90	278	48	-103	37	43
43	2009025000009	2009.01.25 08:28:38	2.7	27.7552	40.7995	12.66	85	78	-93	29	24
44	2009023000001	2009.01.23 16:34:52	3.3	27.7572	40.7953	13.26	156	36	-101	25	42
45	2009025000002	2009.01.25 02:54:23	2.8	27.7582	40.7945	12.25	88	47	-122	30	33
46	2012159000003	2012.06.07 20:54:26	4.3	27.9180	40.8402	11.55	98	56	-156	24	34

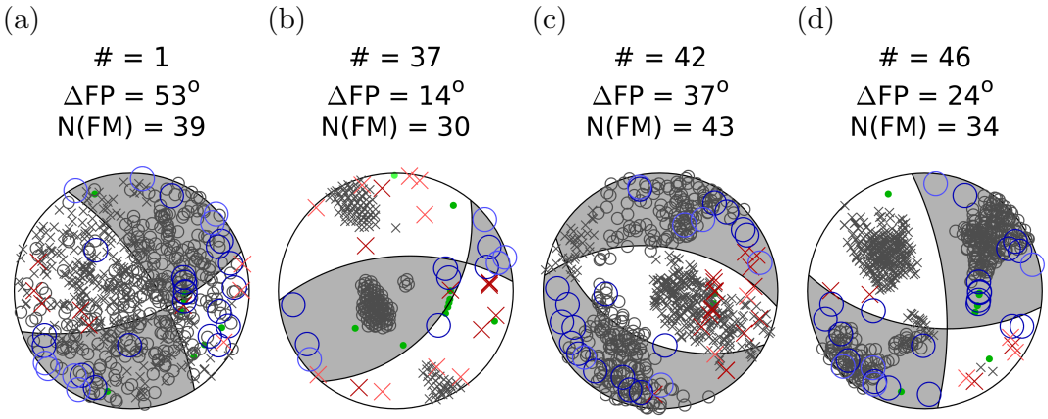

Figure 4.14.: Four exemplary focal mechanism solutions from Fig. 4.12 and Table 4.5. Inverted first-motion polarities are shown as blue circles, red crosses and green dots resembling up, down and indeterminable first motions, respectively. The P- and T-axis of "acceptable solutions" returned by HASH (Hardebeck et al. 2002) are shown as grey circles and crosses, respectively. The title lists the focal mechanism ID (#), focal plane uncertainty (ΔFP) and number of first-motions inverted ($N(FM)$).

are observed seems to indicate that there is neither a single through-going strike-slip fault as proposed by Le Pichon et al. (2001) nor a dominantly set of en-echelon normal faulting Armijo et al. (2002). In contrast, the entire region currently sees both strike-slip and normal faulting along the entire NAFZ section below the Sea of Marmara leaving the question open whether a pending larger earthquake might be one dominantly strike-slip event or a series of smaller normal faulting earthquakes.

Two focal mechanisms were calculated west of the Istanbul bend (numbers 6 and 7 in Fig. 4.12), being both normal faulting and suggesting that the ruptured faults form a large angle with the main fault trace to the north. This further supports the hypothesis that the seismicity of this region is occurring predominantly off-fault and therefore the main section could be accumulating seismic energy. In contrast, around the Central Basin (focal mechanisms 40, 1, 2, 3) the fault plane striking approximately ∼80° is in good agreement with the main fault trace at this area. This could provide further indication that around the Central Basin the seismicity occurs predominantly on the fault and that a portion of the slip is released aseismically.

Many of the focal mechanisms have a significant reverse component: 25 % measure oblique plunge of the tensional axis ($22.5° < pl(T) <= 67.5°$), another 4 % near vertical ($pl(T) <= 22.5°$) reverse components. This result contradicts the large scale picture, that the Sea of Marmara region is dominated by a transtensional stress regime, raising the question of how reliable this is. However, the set of focal mechanisms with thrust components includes such

with comparatively small uncertainties (Fig. 4.14b) thus confirming previous observations of local thrust faulting throughout the Sea of Marmara region made by other studies (Pinar et al. 2001, 2003; Bohnhoff et al. 2006; Bulut et al. 2009; Öztürk et al. 2015). The agglomeration of reverse faulting in the West near the Ganos Bend can be attributed to a transpressional stress-field component which results from the change of strike of the Marmara Section here (Pinar et al. 2003; Janssen et al. 2009; Örgülü 2011; Öztürk et al. 2015). In contrast rather sparse reverse faulting in other areas, e.g. the Central Basin as well as around the termination of the 1999 Izmit rupture, is explained with the activation of subsidiary faults, e.g. antithetic Riedel shears developing in vicinity of main E-W striking fault, (Pinar et al. 2003).

4.4. Conclusions

We present a refined hypocentre catalogue for the Sea of Marmara containing 6812 earthquake locations recorded during a $10\frac{1}{2}$ year period of time in the years 2006–2016. Relative relocation yields a subset of 4407 high precision earthquake locations. We calculate moment magnitudes for 5353 and focal mechanisms for 140 earthquakes. Our results are based on the analysis of recordings from several permanent seismic networks, most importantly of the integrated datasets provided by the two major national seismological services (AFAD and KOERI) running the largest seismological networks in the area. We employed an analysis scheme including automatized timing of P- and S-phases, determination of the P-wave first-motion polarity and an iterative travel-time inversion. Particular caution was exercised during the automatic picking, where results for P- and S-phases were assigned continuous uncertainties and validated with a set of manual reference picks.

A previously developed automatized picking scheme was modified and adapted to the here analysed regional seismicity. Approximately 360,000 P- and S-picks were retrieved and 165,000 crustal first arriving P- and S-phases inverted. With respect to manual reference picks, 68 % of automatic P- and S-picks lie within $\sim 0.1s$ and ~ 0.3s, respectively. Despite rigorously discarding seismic recordings without determinable seismic onsets, an iterative travel-time inversion-scheme improves location accuracy by discarding further miss-picked phase onsets. During this procedure, we fall back to phase-pick uncertainties which were calculated with a novel approach employing multiple application of the Akaike-Information-Criterion (AIC) to different windows of a seismic recording that likely contain the targeted seismic onset.

Our absolute (and relatively relocated) earthquake hypocentres make out more than one half (one third) of the $\sim 12,000$ earthquakes reported by the national seismological services and other researchers. We show that the loss affects small earthquakes that were likely recorded by a small fraction of the network only and thus lack sufficient observations needed for precise localization.

However, the final relative relocation of hypocentres yields a consistent long-term observation of a decade of regional seismic activity along the Marmara Section of the North Anatolian Fault Zone, during a seismotectonic period that presumably is developing towards a major $M \geq 7$ earthquake posing a significant seismic risk to substantial infrastructure in the Istanbul metropolitan area. Compared to the original merged catalogue, our automatized processing chain achieves a substantial improvement particularly of epicentral location accuracy. In areas at close proximity to seismic stations, e.g. the Princes' Islands segment, the improvement is distinct also in the vertical. The relative relocation further compacts densely occurring seismicity, revealing linear trends as well as sharpening the contours of its distribution.

The epicentral distribution delineates the Marmara Section of the northern branch of the NAF as the more active compared to the northern most branch of the southern NAF along the Southern Shelf Margin. Three unambiguously identifiable aseismic patches on the Marmara Section raise the question on the cause of this quiescence. Aseismic creep has been deduced from the occurrence of seismic repeaters as well as from large deformation rates measured with acoustic extensometers for some locations in the western half of the central part of the Marmara Section (Western High, Central Basin). However they are located outside the aseismic patches on which we report here, indicating that they are probably locked fault patches and thus potential nucleation points for the pending Marmara earthquake. Neither repeaters nor large deformation rates are reported for the Princes' Islands segment. Seismic activity in the past decade seems to occur off fault and predominantly on the edges of the aseismic patch, supporting previous studies that this fault segment in the immediate vicinity to the Istanbul Metropolitan area is locked. With respect to the E-W orientation of the central Marmara Section, we predominantly observe strike-slip with sub-parallel strike as well as normal faulting mechanisms of parallel and almost orthogonal strike. These mechanisms do not correlate clearly with magnitude, indicating that the region finds itself in a transtensional stress regime. Observation of well resolved reverse faulting mechanisms confirms results of other studies that numerous subsidiary faults exist in the area. This could be attributed to fault stepovers along the Marmara Section and supports the hypothesis of ongoing structure development. Consequently the here presented results show that neither the pure strike-slip nor the normal fault model are supported by the data. Instead a combination of both, with intersecting strike-slip and normal fault segments along the Marmara Section of the NAFZ is suggested by our findings.

4.A. Flip-book of initial, new absolute and new relocated hypocentre locations

We compared the original to our new absolute locations as well as the latter to the relative relocations with respect to the epicentral as well as the depth distribution in the cross-sections shown along the Marmara Section, the Southern Shelf Margin and the Princes' Islands segment by plotting dislocation vectors in Fig. 4.6 and 4.7. Although this is the most concise way to compare two catalogues, many of the dislocation vectors overlap thus obscuring some of the details. We here plot the catalogues individually each on a new page, in order to compare old and new locations in a flip-book like manner. The catalogues are organized as follows:

1. Merged catalogue (original locations, Fig. 4.15)
2. Fair absolute locations (Fig. 4.16)
3. Absolute locations (restricted to corresponding relative relocation, Fig. 4.17)
4. Relative relocations (Fig. 4.18)
5. Merged catalogue (restricted to corresponding relative relocation, Fig. 4.19)

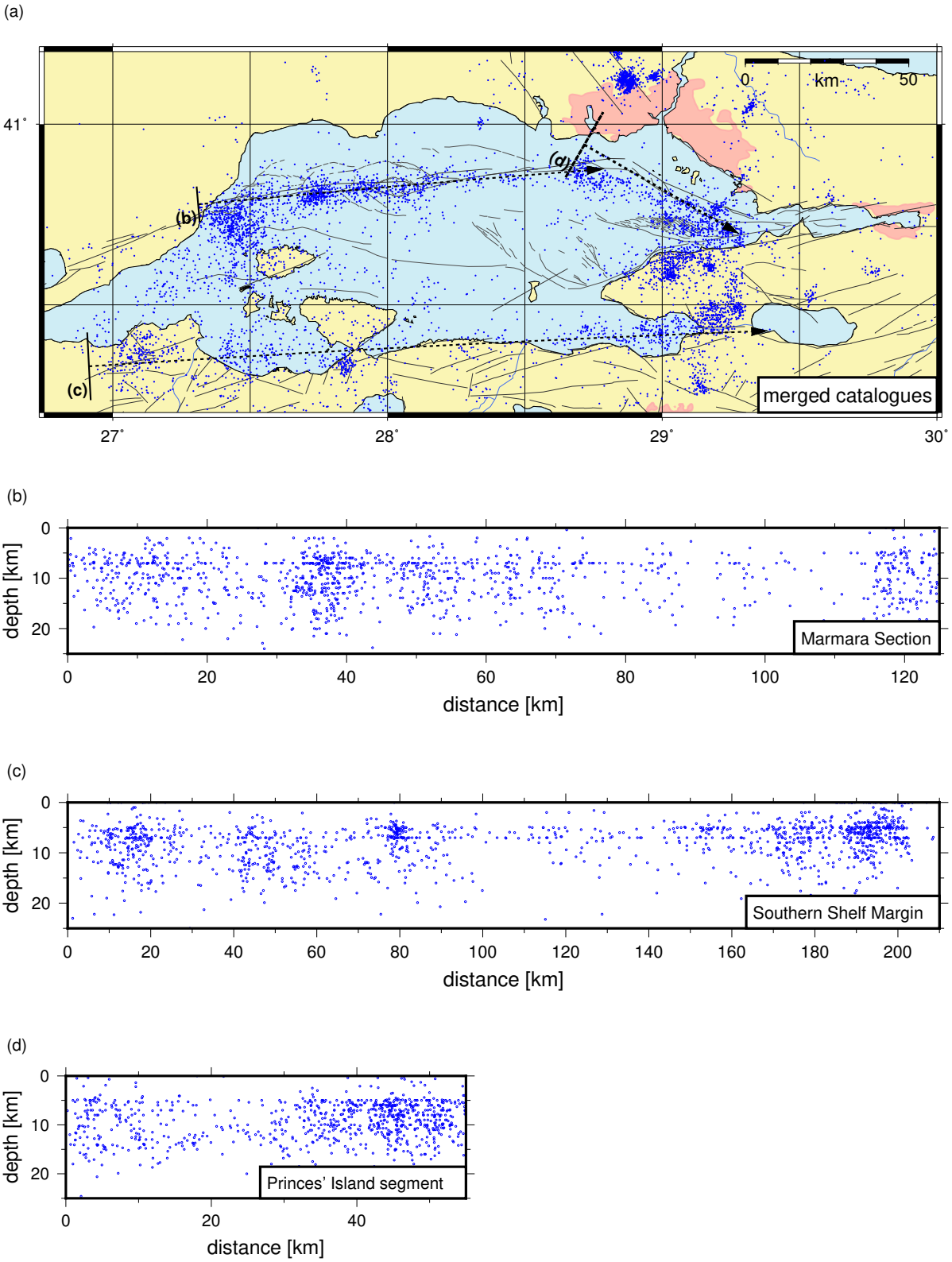

Figure 4.15: Merged original catalogues (restricted to events with a correspondent in the catalogue of fair absolute locations).

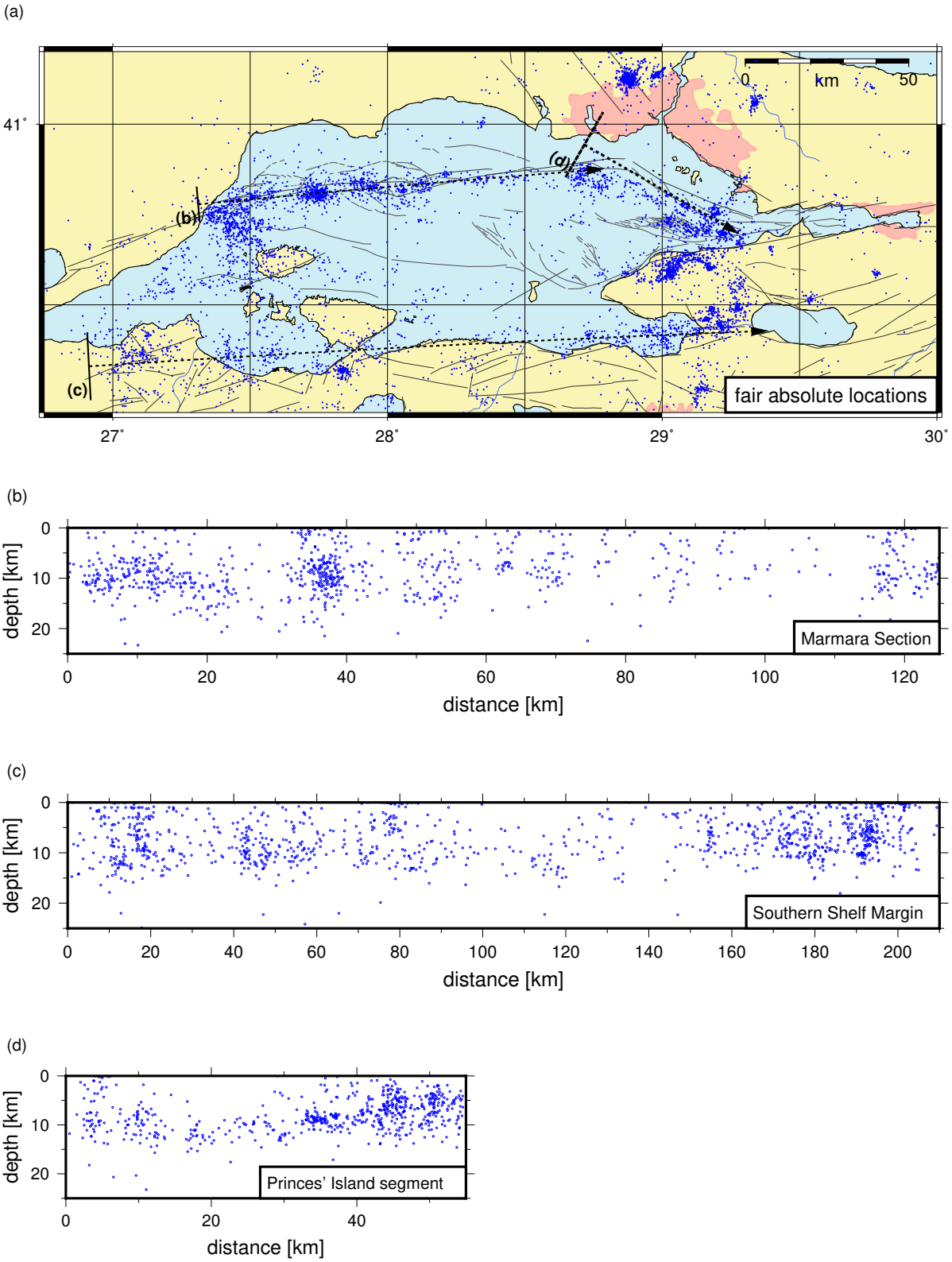

Figure 4.16: Fair absolute locations.

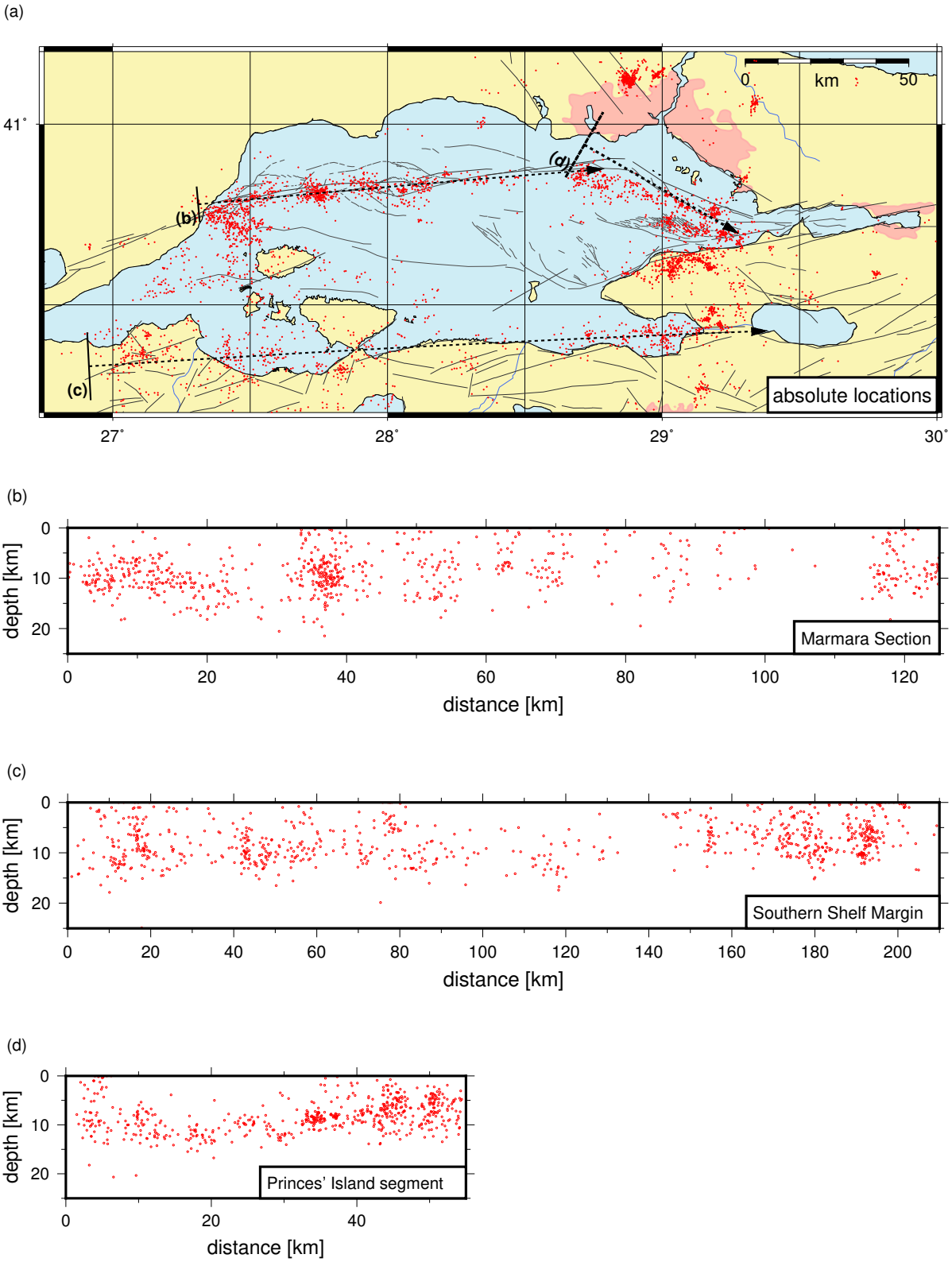

Figure 4.17: Fair absolute locations (restricted to events with a correspondent in the catalogue of the very best relocations).

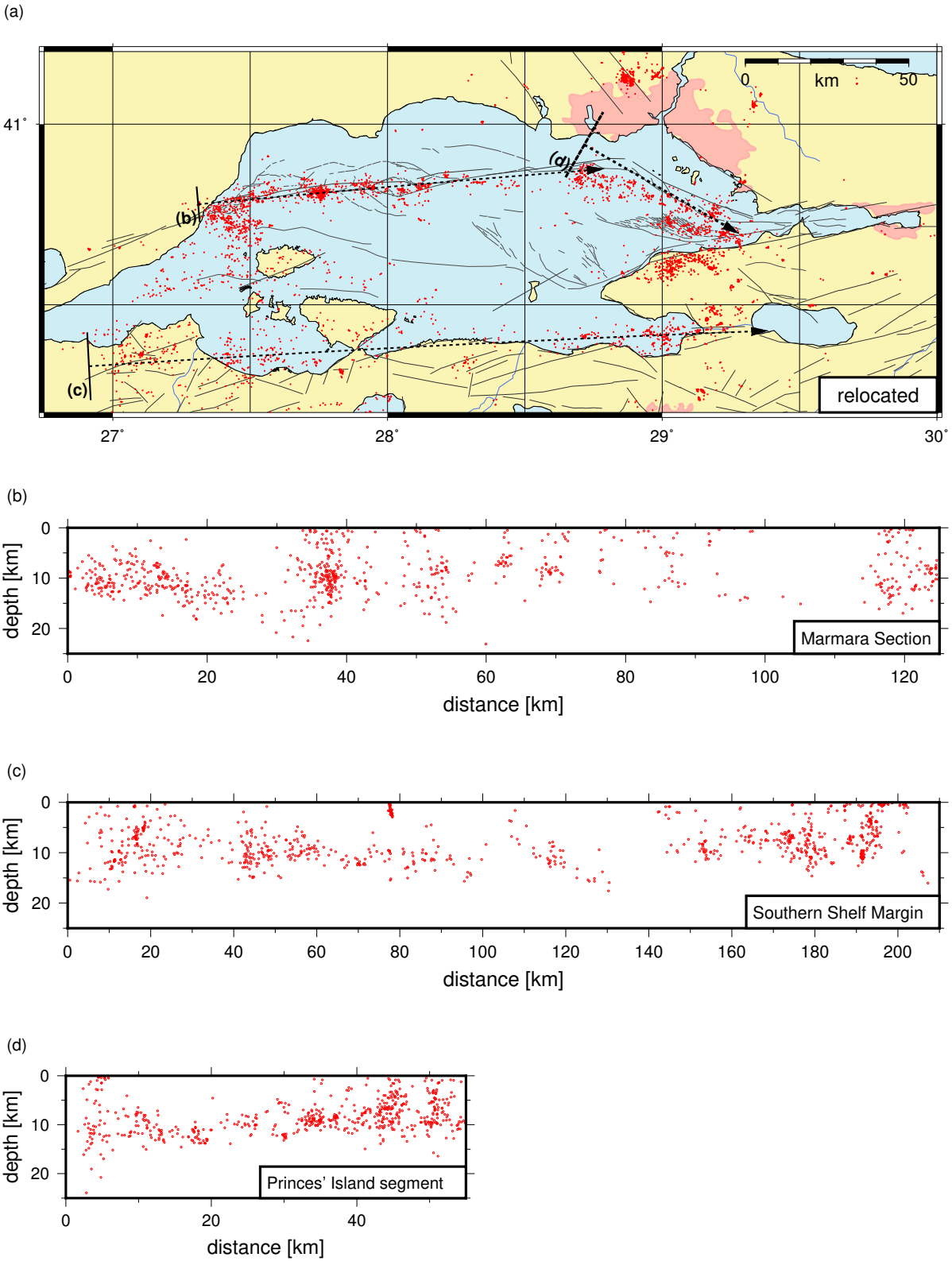

Figure 4.18: Relocated catalogue.

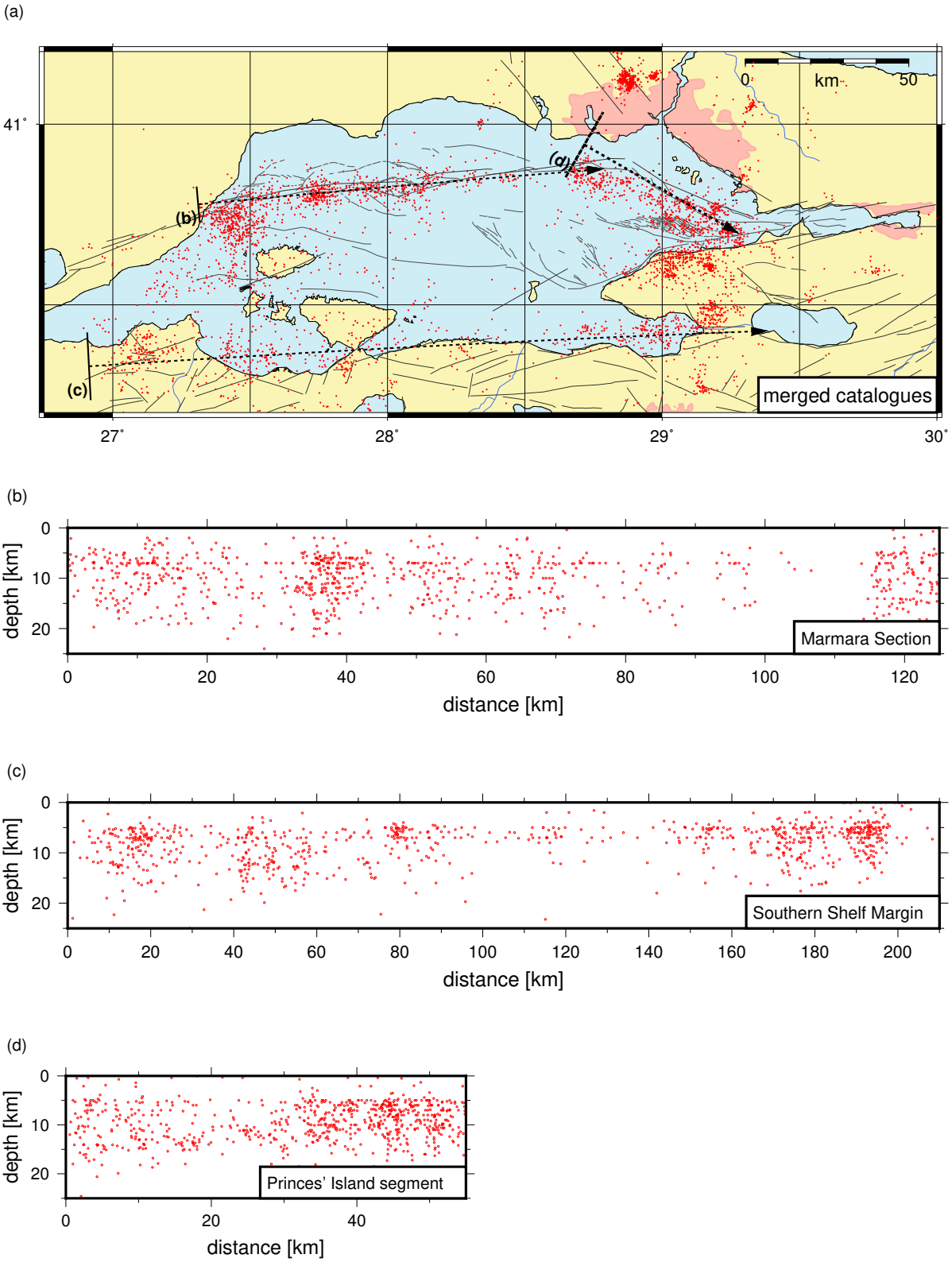

Figure 4.19: Merged original catalogues (restricted to events with a correspondent in the catalogue of the very best relocations).

5. Repeating Marmara Sea earthquakes: indication for fault creep[a]

Abstract Discriminating between a creeping and a locked status of active faults is of central relevance to characterize potential rupture scenarios of future earthquakes and the associated seismic hazard for nearby population centres. In this respect, highly similar earthquakes that repeatedly activate the same patch of an active fault portion are an important diagnostic tool to identify and possibly even quantify the amount of fault creep. Here, we present a refined hypocentre catalogue for the Marmara region in northwestern Turkey, where a magnitude M up to 7.4 earthquake is expected in the near future. Based on waveform cross-correlation for selected spatial seismicity clusters, we identify two magnitude $M \approx 2.8$ repeater pairs. These repeaters were identified as being indicative of fault creep based on the selection criteria applied to the waveforms. They are located below the western part of the Marmara section of the North Anatolian Fault Zone and are the largest reported repeaters for the larger Marmara region. While the eastern portion of the Marmara seismic gap has been identified to be locked, only sparse information on the deformation status has been reported for its western part. Our findings indicate that the western Marmara section deforms aseismically to a substantial extent, which reduces the probability for this region to host a nucleation point for the pending Marmara earthquake. This is of relevance, since a nucleation of the Marmara event in the west and subsequent eastward rupture propagation towards the Istanbul metropolitan region would result in a substantially higher seismic hazard and resulting risk than if the earthquake would nucleate in the east and thus propagate westward away from the population centre Istanbul.

[a]With exception of some omissions and supplements, this chapter has been published as a research article in Geophysical Journal International: M. Bohnhoff, **C. Wollin**, D. Domigall, L. Küperkoch, P. Martínez-Garzón, G. Kwiatek, G. Dresen and P. E. Malin (2017a); Repeating Marmara Sea earthquakes: indication for fault creep, In: *Geophysical Journal International*, Volume 210, Issue 1, Pages 332–339, https://doi.org/10.1093/gji/ggx169. Published by Oxford University Press on behalf of The Royal Astronomical Society and Deutsche Geophysikalische Gesellschaft.
The description of the tectonic setting of the Sea of Marmara and parts of the introduction have been moved to the introduction of this thesis (Chapter 2). After the article had been published, further insights into the topic of this chapter where made possible by extending the underlying database from a four to a ten year period (Chapter 4). These additional results are described in an amendment to the here recited article (Sec. 5.A).

5.1. Introduction

The Marmara section of the NAFZ is considered as a seismic gap for an $M \sim 7.4$ earthquake (Barka et al. 2002; Parsons 2004; Murru et al. 2016), posing a major hazard to the Istanbul metropolitan region with its $>$ 15 million inhabitants. A key question in this light is whether the $\sim$ 140 km long offshore fault segment is currently fully locked or partially creeping. Along its eastern portion, the Princes' Islands segment offshore Istanbul, a locked patch over a creeping base was identified based on both abundant local seismicity above 10 km depth (Bohnhoff et al. 2013) and GPS data (Ergintav et al. 2014). First results from seafloor deformation measurements along the adjacent segment to the west (Istanbul-Silivri fault) also tend to favour a locked over a creeping status there (Sakic et al. 2016). For the western Marmara section at the central Basin, Schmittbuhl et al. (2016) and Yamamoto et al. (2016) recently reported on indications for fault creep based on the observation of small-magnitude repeating earthquakes and observations from seabed acoustic extensometers, respectively.

In contrast to the easternmost portion of the Marmara section (Bohnhoff et al. 2013, 2017b), the NAFZ west of the Istanbul-Silivri fault is generally less well characterized. This is due to the absence of near-fault onshore locations and subsequent limits in high-precision seismic monitoring (Fig. 2.1). The western portion of the Marmara section, however, is of particular relevance since a repeat of an $M > 7$ Marmara event could nucleate there. Should that happen, the directivity effects of an eastward propagating rupture towards Istanbul would result in increasing ground shaking and subsequent enhanced seismic risk there.

One way of addressing the question of a locked versus creeping fault is through their association with repeating micro and local earthquakes. Repeating earthquakes along active plate boundaries appear to represent multiple slip of a brittle fault patch that is surrounded by an aseismically deforming fault. They seem to imply (1) constant tectonic loading and subsequent stress accumulation, (2) constant peak stress resulting in rock failure, (3) highly similar ray paths of seismic waves between the hypocentre and individual receiver stations (i.e. no first-order velocity changes in the time period considered) and (4) constant background noise levels at the receivers (Poupinet et al. 1984; Vidale et al. 1994; Nadeau et al. 1995, 2004). For the time period of several years considered in this study, assumption (4) is the least constrained due to natural and anthropogenic noise variations. However, also in situ changes in underground fluid pressure or the occurrence of nearby larger earthquakes can cause the recurrence intervals of repeating earthquakes to vary.

Seismic repeaters have been reported along several sections of the San Andreas Fault that are associated with creep (Nadeau et al. 2004). The most prominent examples are the M up to 2 repeaters along the Parkfield section in

central California (Nadeau et al. 1995; Rubinstein et al. 2010) and several repeater spots along the Hayward–Calaveras section in the eastern San Francisco bay area (Waldhauser et al. 2002; Chaussard et al. 2015).

In this paper, we report on the observation of repeating earthquakes below the western Marmara segment. The events have a magnitude of $M \sim 2.8$ and a recurrence period of up to 38 months. Their discovery was made possible with a newly compiled high-resolution hypocentre catalogue for the Marmara region. This catalogue was derived from careful re-examination and re-picking of waveform recordings from three previously separate networks. Waveforms recorded from these networks and originating from earthquakes located in four different clusters across the Sea of Marmara were cross-correlated in a search for high waveform similarity, following strict selection criteria and resulting in the discovery of the $M \sim 2.8$ repeating earthquakes.

5.2. Seismicity in the Marmara Region (2006–2010)

The key factor in identifying repeating earthquakes is a well constrained hypocentre catalogue based on high-quality waveform recordings. Here, we combine for the first time waveform data from the seismic networks of KOERI (Kandilli Observatory and Earthquake Research Institute), AFAD (Disaster and Emergency Management Presidency of Turkey) and the island-based PIRES (Princes' Islands Real-time Earthquake monitoring System Bulut et al. 2009; Bohnhoff et al. 2013). This results in an optimum azimuthal coverage for seismicity occurring along the entire Marmara section of the NAFZ.

From these combined networks, we generated a uniform waveform database considering merged detections of events from all three mentioned networks and incorporating all the available stations for the period 2006–2010. Sampling rate was 50 Hz (KOERI and AFAD) or 200 Hz (PIRES).

A total of 4016 events were picked and located following the procedure described above.[1] The magnitude-frequency distribution suggests that $M2.7$ is the lower magnitude of completeness (M_c hereafter) and thus smaller events are not complete in the catalogue due to the source–receiver geometry throughout the region (comparatively large epicentral distances due to offshore location of the fault). To ensure that only the best-constrained events were used to locate the Marmara fault, we restricted the catalogue based on individual number of picks, root mean square (rms) value and epicentre error ellipsoid. This severely reduced the set of best-constrained events to 1226 all of which were located based on phase arrival picks from ≥ 20 stations (Fig. 5.1a). Fig. 5.1b shows the distribution of the travel time residuals' (rms) of all located events. The epicentral distribution of the 1226 best-constrained events together with the

[1] i.e. in Sec. 3.3–3.4.3 and Sec. 4.2.1.

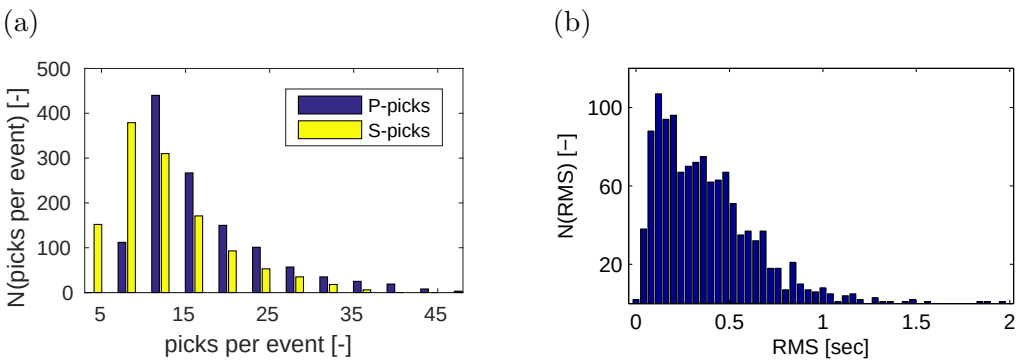

Figure 5.1.: (a) Frequency of events of the newly compiled Marmara hypocentre catalogue located with a certain number of P and S picks, respectively. (b) Root mean square (rms) values for the refined hypocentre catalogue for the Marmara region.

error ellipses is shown in Fig. 5.2. It allows for the identification of several active fault strands below the Sea of Marmara. These active fault patches alternate with areas of reduced or increased seismicity. In general, the seismicity distribution highlights the northern main branch of the NAFZ. This branch is where most of the current deformation takes place between the Ganos fault in the west and the western termination of the 1999 Izmit rupture just southeast of the Princes' Islands (Fig. 2.1).

5.3. Waveform processing and analysis to search for seismic repeaters

Repeating earthquakes represent multiple occurrences at the same location with the same magnitude and identical or highly similar waveforms. When they occur along active faults, they reflect multiple activation of the same brittle fault patch in a fault section also exhibiting creep. Given a constant deformation rate across a particular fault segment and assuming that the co-seismic slip scales with event size, the recurrence time of repeaters appears to be inversely proportional to their magnitude. Given our use of an $M < 2.2$ cut-off for our relatively limited-time data set, one might expect very few, if any, repeating events could be found in the new catalogue. If found at this level, several more should be present at smaller magnitudes in the surrounding area, but remain undetected since in the given station geometry they do not produce signal-to-noise ratios high enough to qualify for repeater given our selection criteria.

To search for repeaters within the new Marmara seismicity catalogue, we applied a cluster analysis involving waveform cross-correlation (e.g. Aster et

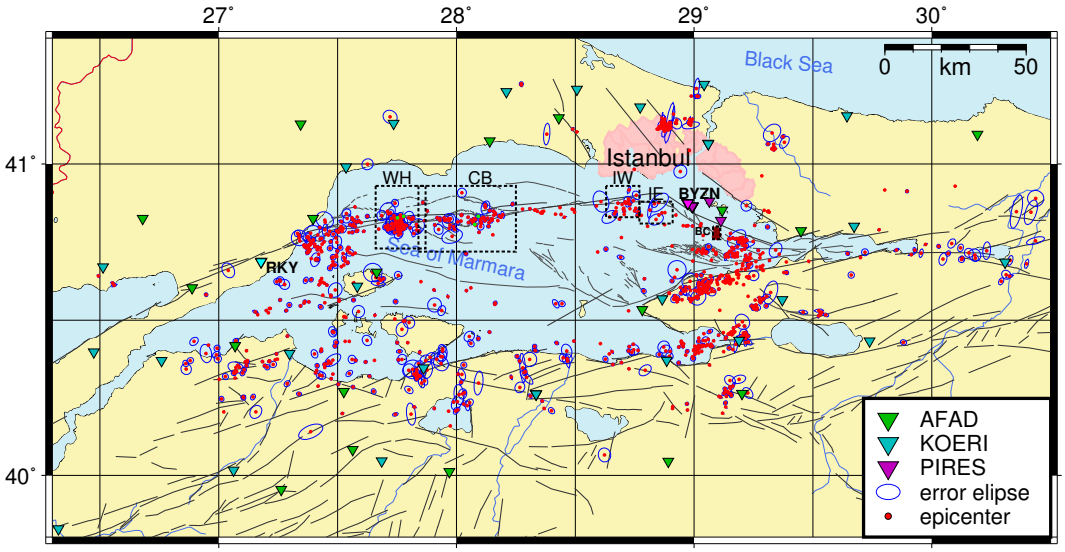

Figure 5.2.: Refined seismicity catalogue presented in this study for the time period 2006–2010 containing 1226 events as selected based on hypocentre precision. Red dots are epicentres, while the blue ellipses indicate their location error (see the text for details). The epicentral distribution allows to identify the location of the NAFZ below the Sea of Marmara with unprecedented detail. From this catalogue, five spatial clusters (indicated by the black rectangles) were determined and studied using waveform cross-correlation to search for seismic repeaters: these are from east to west the Baliciada (BC), the Istanbul-East (IE), the Istanbul-West (IW), the Central Basin (CB) and the Western High cluster (WH).

al. 1993; Vidale et al. 1994; Chaussard et al. 2015). The similarity of event pairs recorded at specific stations was quantified by their cross-correlation coefficient ($0 \leq ccc \leq 1$). We detrended and tapered 240 s long waveforms (from 60 s prior to and 180 s after origin time) and applied a bandpass filter between 3 and 23 Hz to include the entire frequency bandwidth of P and S waves in the waveform cross-correlation. This is in contrast to Schmittbuhl et al. (2016) who considered a frequency band between 1 and 10 Hz resulting in a larger number of repeaters. We then selected the entire combined P and S body wave train by cutting out wavelet windows of varying length from 0.1 s prior to P to two times the S-P differential travel time after P. For each defined cluster (see Fig. 5.2 for location), we then cross-correlated the wavelets of all event pairs when recorded by the same station.

The resulting correlation coefficients for event pairs recorded at a specific station were then sorted and visualized in matrix form (see example in Fig. 5.3). To identify potential repeating events, we then selected event pairs and multiplets (repeater groups consisting of more than two highly similar events) for further consideration if their cross-correlation coefficient was higher than 0.9 at a minimum of two stations and if their recurrence time was longer than 30 d. This eliminated main shock-aftershock sequences and swarm-like event occurrences like the Baliciada cluster (Bulut et al. 2011). Events were then identified as repeating earthquakes if their hypocentres were within 5 km epicentral distance and if their magnitudes were within ±0.2 units. For event pairs or multiplets fulfilling these criteria, we then took the cross-correlation results from other stations (i.e. where the correlation coefficients might have been lower due to higher background noise, with the result that they were not qualified as a repeater at that station) into consideration.

We applied this analysis scheme to five seismicity clusters that were defined based on their spatial density of events. These are from east to west (1) the Baliciada cluster (40.76–40.8°N, 29.08–29.11°E), (2) the Istanbul-East cluster (40.81–40.88°N, 28.77–28.91°E), (3) the Istanbul-West cluster (40.83–40.93°N, 28.63–28.77°E), (4) the Central Basin cluster (40.72– 40.93°N, 27.84–28.25°E) and (5) the Western High cluster (40.73–40.93°N, 27.66–27.87°E). All five clusters are indicated in Fig. 5.2.

The Baliciada cluster occurred immediately offshore of the PIRES network below the eastern Sea of Marmara and was investigated earlier by (Bulut et al. 2011). It includes 70 events that occurred within less than 24 hr. Following our definition (minimum recurrence time 30 days), these events do not qualify as repeaters. Rather, this sequence represents a seismic swarm with a systematic migration from the main Princes' Islands fault onto a smaller scale splay fault. However, the events of this cluster provide an excellent data set to test our algorithm to identify highly similar events.

Within the Istanbul-West (75 events) and Istanbul-East (102 events) clusters no repeating events with a correlation coefficient > 0.9 were identified at

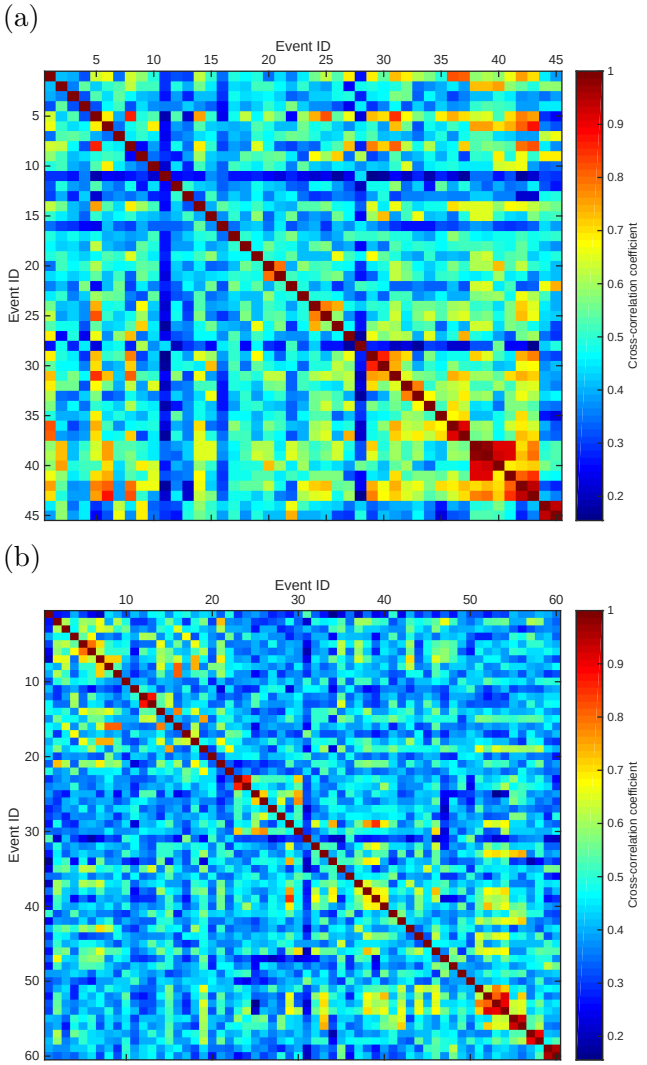

Figure 5.3.: (a) Cross-correlation coefficients of waveforms from the Central Basin spatial seismicity cluster (see Fig. 5.2 for location) recorded at the station PIRES BYZN on the Princes' Islands. A total of 45 events from this cluster were recorded at this station. The two identified repeaters (cross-correlation coefficient > 0.9) have Event-ID 44 and 45 and are seen in the lower right. (b) Cross-correlation coefficients of waveforms from the Western High spatial seismicity cluster (see Fig. 5.2 for location) recorded at the station RKY. A total of 60 events from this cluster were recorded at this station. The two identified repeaters (cross-correlation coefficient > 0.9) have Event-ID 59 and 60 and are seen in the lower right.

any station. This is in good agreement with earlier findings from the PIRES catalogue and GPS data that were interpreted as evidence of a locked status of the Princes' Islands segment (Bohnhoff et al. 2013; Ergintav et al. 2014) and the westward adjacent Istanbul–Silivri fault (Sakic et al. 2016).

Within the Central Basin cluster (176 events, indicated as CB in Fig. 5.2), two repeating earthquakes were identified based on high cross-correlation coefficients of $ccc > 0.8$ at 20 stations, including seven stations that have $ccc > 0.9$ for this event pair . The magnitude of this event pair is $M2.7$ and the inter-event time is 12 months. To the accuracy of the location method hypocentral depths of these events are 12 and 13 km, respectively. Fig. 5.3a shows the cross-correlation matrix of this cluster obtained from waveform recordings at station BYZN. The waveforms of the two repeaters – the events with the highest overall cross-correlation coefficients – recorded at the stations BYZN and GONE are shown in Figs 5.4a and b. The lack of additional repeater pairs may be directly related to the fact that the magnitude of the repeater pair is close to the catalogue magnitude of completeness M_c of 2.7 and thus slightly smaller additional repeaters might not have been detected. Given the example of the many repeating events on the San Andreas at smaller magnitudes than this, such events ended up being excluded from the hypocentre catalogue. Indeed, we have indications for several more similar events (potential repeaters) that have smaller ($M < 2.2$) magnitudes. However, keeping our strict selection criteria these events did not qualify as repeaters and were thus not further considered to indicate potential fault creep around the respective fault patch.

Within the Western High cluster (136 events, indicated as WH in Fig. 5.2), two repeaters were identified that have an inter-event time of 38 months. The magnitude was 2.8 in both cases and the hypocentral depth was determined to as 6.0 and 7.8 km, respectively. Fig. 5.3b shows the cross-correlation matrix of this cluster based on waveform recordings at station RKY. Examples of waveform recordings recorded at stations EDRB and RKY are shown in Figs 5.5a and b.

5.4. Discussion

Two pairs of repeating earthquakes were found below the western portion of the Marmara seismic gap. The repeater pairs reflect multiple rupture of the same fault patch and are interpreted to be surrounded by partially creeping fault sections. To further quantify the percentage of creep to be obtained from the repeater pairs, we assume an average annual deformation along the main northern branch of the fault below the Sea of Marmara where the repeating events occurred to as 15–20 mm (Hergert et al. 2010).

Furthermore, we assume an average coseismic displacement of the two repeater pairs from the Central Basin and the Western High that have a magnitude of 2.7 and 2.8, respectively, on the order of 10–15 mm (Bohnhoff et al.

(a)

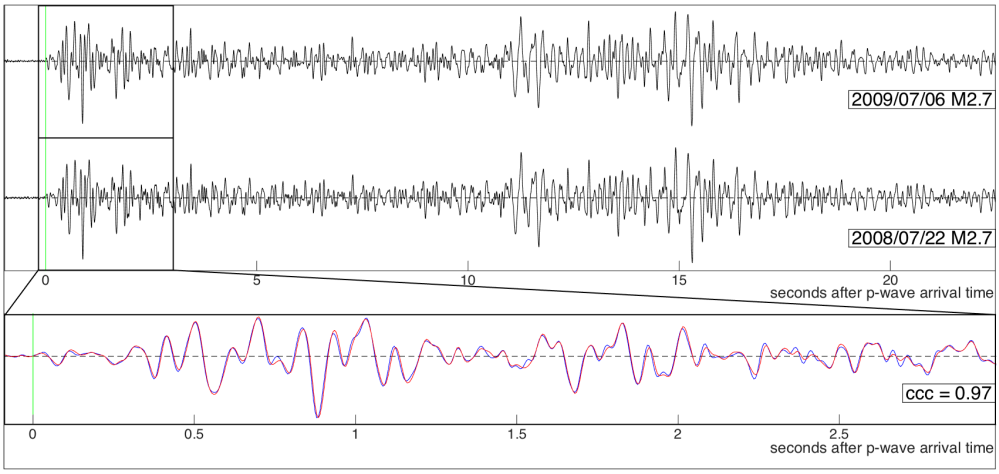

(b)

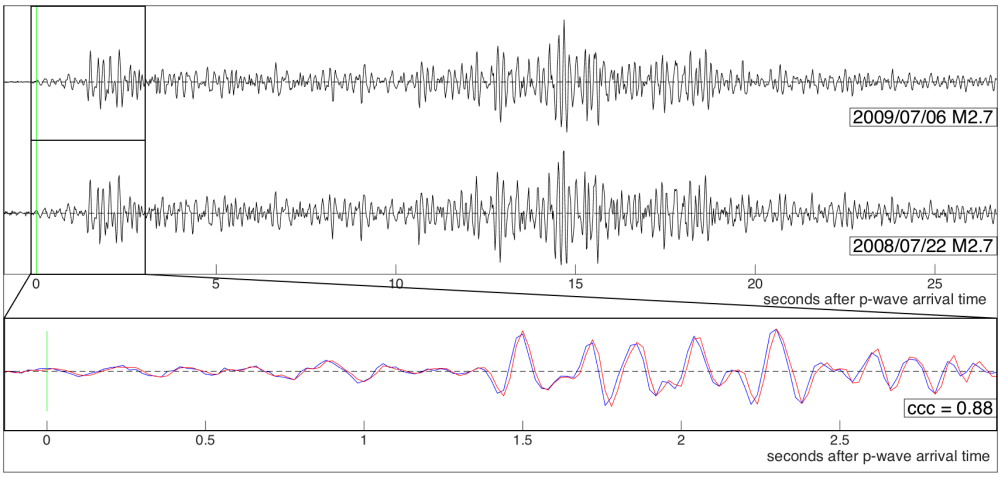

Figure 5.4.: (a) and (b) Waveform examples from the repeater pair identified within the Central Basin spatial seismicity cluster, recorded at stations (a) BYZN and (b) GONE. The entire waveform shown here was cross-correlated after applying a 3–23 Hz bandpass filter. The magnitude for both events is $M = 2.7$ and the cross-correlation coefficient for this event pair is 0.97 and 0.88, respectively. The lower section of both figures shows the zoomed P wave and its coda.

(a)

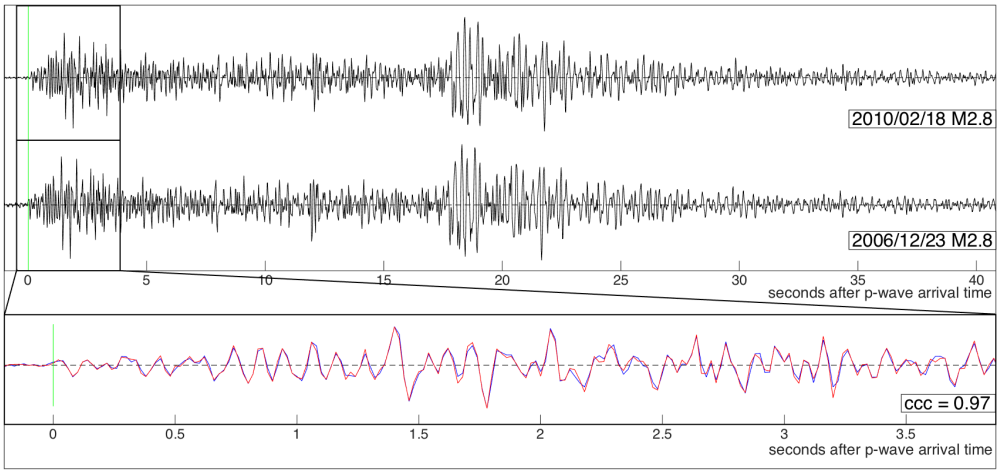

(b)

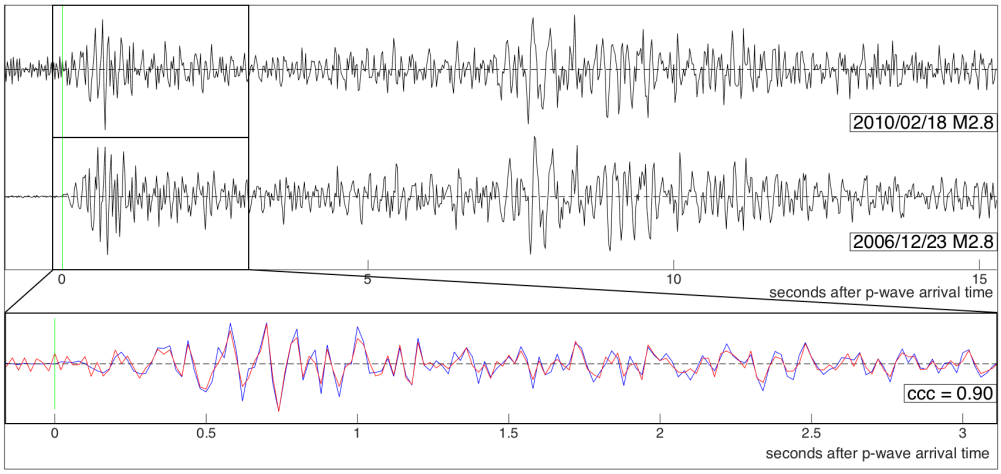

Figure 5.5.: (a) and (b) Waveform examples from the repeater pair identified within the Western High spatial seismicity cluster, recorded at stations (a) EDRB and (b) RKY. The entire waveform shown here was cross-correlated after applying a 3–23 Hz bandpass filter. The magnitude for both events is $M = 2.8$ and the cross-correlation coefficient for this event pair is 0.97 and 0.90, respectively. The lower section of both figures shows the zoomed P wave and its coda.

2010, their table 1). This allows estimating the amount of fault creep to be on the order of 25 per cent (Western High, where the recurrence time is 38 months) and 75 per cent (Central Basin, where the recurrence rate is 12 months). This clearly represents a first-order estimate of the amount of fault creep since we only consider one repetition time and those values may be refined in case further repeating events at these spots are observed in the future. For example, should there be further slightly smaller ($M < 2.7$) repeaters occurring along these fault spots, the recurrence time of the repeaters at the Western High might be as low as 12 months increasing the creep to as much as 75 per cent (the same value currently obtained for the Central Basin). Alternatively, if there were variations in the recurrence time of the repeaters then 25 per cent fault creep might turn out to be a representative value for the western Marmara section of the NAFZ. In any case, the observed repeaters and the derived values for fault creep of 25 per cent (Western High) and 75 per cent (Central Basin) along the western portion of the Marmara section of the NAFZ provide means to conclude on a partly creeping deformation status there.

Presumably, the observed repeating earthquakes are caused by patches of brittle material (asperities) on the fault that fail repeatedly as they are loaded by creep on the surrounding surface. Since our catalogue is restricted to four years, we did not detect further potential repeater candidates before 2006 or after 2010 preventing us from calculating average and thus more reliable recurrence times. However, the fact that the identified similar events fulfil all requirements for repeating events their observation is solid and seen as a strong indication for partial fault creep below the western portion of the NAFZ Marmara section. These findings are in good correspondence with the recently reported results for partial (Yamamoto et al. 2016) or total (Schmittbuhl et al. 2016) fault creep along this part of the Marmara section, especially since the amount of fault creep does not necessarily need to be constant over a large area but instead may vary even on a local scale along a specific fault segment.

The observed fault creep below the western Sea of Marmara has substantial implications for the seismic hazard assessment for the greater Istanbul metropolitan region. It suggests a reduced accumulation of stress along the western Marmara section due to partial creep. Thus, the probability that the pending Marmara earthquake would nucleate there with a rupture propagation towards Istanbul is reduced. In contrast, the eastern Marmara section along the Princes' Islands segment is believed to be locked down to at least 10 km and thus needs to be considered to host a potential nucleation point for the pending Marmara event. In that case, the early warning time for Istanbul would be a few seconds only given the short distance of only $\sim$ 20 km to the historic city centre. However, the rupture propagation would be primarily towards the west and thus away from the city, which limits the ground motion due to directivity effects.

5.5. Conclusions

We present a refined hypocentre catalogue for the Marmara region in north-western Turkey where a magnitude M up to 7.4 earthquake is expected in the near future. Based on that four-year catalogue and applying a waveform cross-correlation technique to selected spatial seismicity clusters below the Sea of Marmara we identify two magnitude $M \sim 2.8$ repeater pairs. These repeaters are located below the western part of the Marmara section of the NAFZ and are indicative of partial fault creep there. This is in contrast to the eastern and central portions of the Marmara section that are believed to be locked. Our results suggest that the probability for the pending Marmara earthquake to nucleate at the eastern – locked-Marmara section is possibly higher than at the western – partially creeping Marmara section. This is of central relevance since an eastward rupture propagation towards the Istanbul metropolitan region would result in a substantially higher seismic hazard and subsequent risk for the population centre Istanbul than in case of a westward rupture propagation.

5.A. Amendment

The here presented study on "Repeating Marmara Sea Earthquakes" (Bohnhoff et al. 2017a) was performed before the dataset was enlarged to its final size, i.e. before including the years 2011-2016. At the time, also the magnitudes had not been recalculated yet. Then their values reflected mostly durational magnitudes taken from the merged catalogues (see Sec. 2.2) resulting in a magnitude of completeness $M_c = 2.7$.

The cross correlation of waveforms recorded at individual stations from all pairs of different earthquakes was repeated for the entire time period from 2006–2016. As in the original study, the examined earthquakes stemmed from the two regions along the central Marmara Section (**WH** and **CB** in Fig. 5.2). Pairs of events potentially forming repeating earthquakes were selected using the same criteria as before.

In the period succeeding the time interval originally studied, i.e. from 2011 onwards, two more events could be associated with the repeater pair previously found in the Western High area (WH). There, two more independent pairs of earthquakes with similar waveforms were identified. One more independent repeater pair was found in the Cinarcik Basin (CB) too. Figure 5.6a depicts the moment magnitude as function of the origin time for all found repeaters. Figures 5.6b and 5.6c show their absolute hypocentres (from Wollin et al. 2018a) where each repeater sequence is individually coloured as in Fig. 5.6a. Details regarding the hypocentres of the involved earthquakes are listed in Table 5.1. Absolute hypocentre locations were chosen over the relatively relocated ones because the latter do not fully contain all sequences. For pairs of

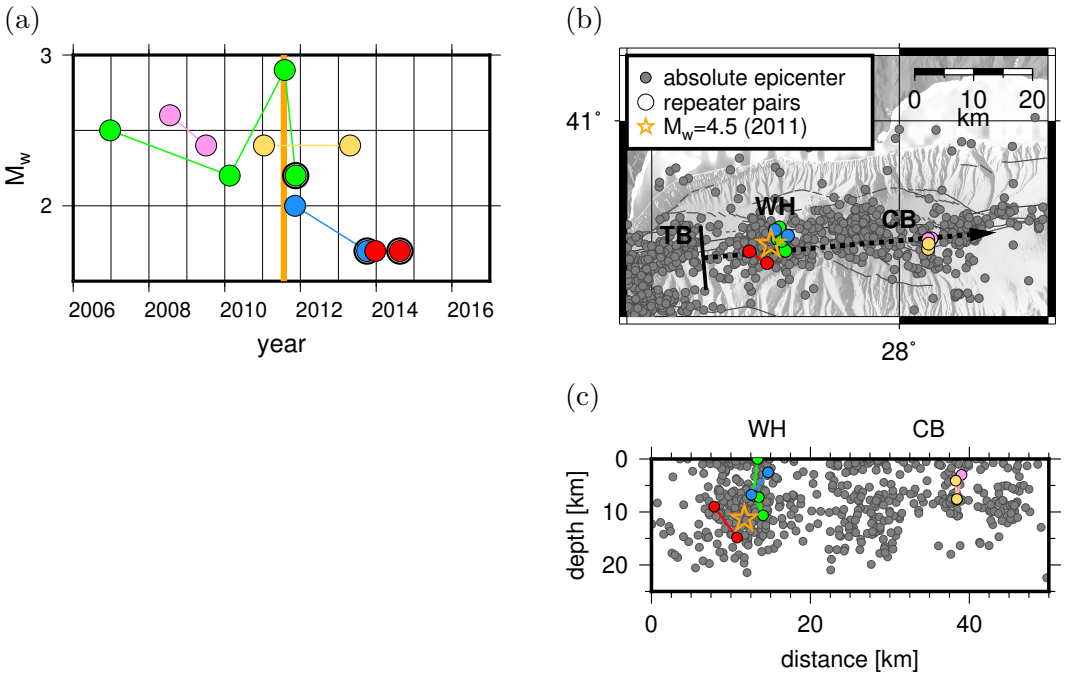

Figure 5.6.: (a) Moment magnitude over origin time of earthquakes categorized as repeating earthquakes. Markers of events with similar waveforms are joint and plotted in the same colour. (b) and (c) map view of the central Marmara Section and cross section through the same with absolute hypocentre locations. Repeating earthquakes are colour coded as in (a). Origin time and hypocentre of a moderate size earthquake in 2011 are indicated by an orange vertical line and orange stars in (a) and (b)+(c), respectively.

events involved in a repeater sequence, Figures 5.7a and 5.7b show the number of P-picks at a common station and the 68th percentile of all cross-correlation coefficients between the corresponding wavelets, respectively.

Whereas all epicentral inter-repeater distances are smaller than 4 km, the differences in hypocentral depth reflect the uncertainties of these offshore locations. Deviating locations within repeater clusters most likely stem from the usage of phase readings from different sets of stations (e.g. Fig. 5.7a). The earthquakes extending the repeater sequence previously found in the Western High both occur in the seismogenic layer indicating that the shallow focal depth of one of the earlier found earthquakes is erroneous (Fig. 5.6c). However, the two later found earthquakes of this sequence occur in temporal vicinity of a moderate size earthquake (#=42 in Table 4.5 and orange markers in Fig. 5.6), the first approximately after one week and the second within a significantly shortened recurrence interval of less than four months. Thus, both events are likely to have been activated as part of an aftershock sequence. The lack of further events after 2012 could be related to the increase of the sampling fre-

Table 5.1.: List of repeater pairs colour coded as in Fig. 5.6

#	cluster ID	event ID	origin time
1	1	2006357000000	23-Dec-2006 07:48:22
2	1	2010049000000	18-Feb-2010 04:56:13
3	1	2011215000000	03-Aug-2011 18:20:55
4	1	2011321000001	17-Nov-2011 23:08:11
5	2	2011314000000	10-Nov-2011 00:17:21
6	2	2013279000001	06-Oct-2013 20:01:29
7	3	2013358000003	24-Dec-2013 22:58:16
8	3	2014230000000	18-Aug-2014 21:18:47
9	5	2008204000000	22-Jul-2008 07:09:51
10	5	2009187000007	06-Jul-2009 18:41:38
11	6	2011015000009	15-Jan-2011 07:51:34
12	6	2013114000007	24-Apr-2013 16:24:20

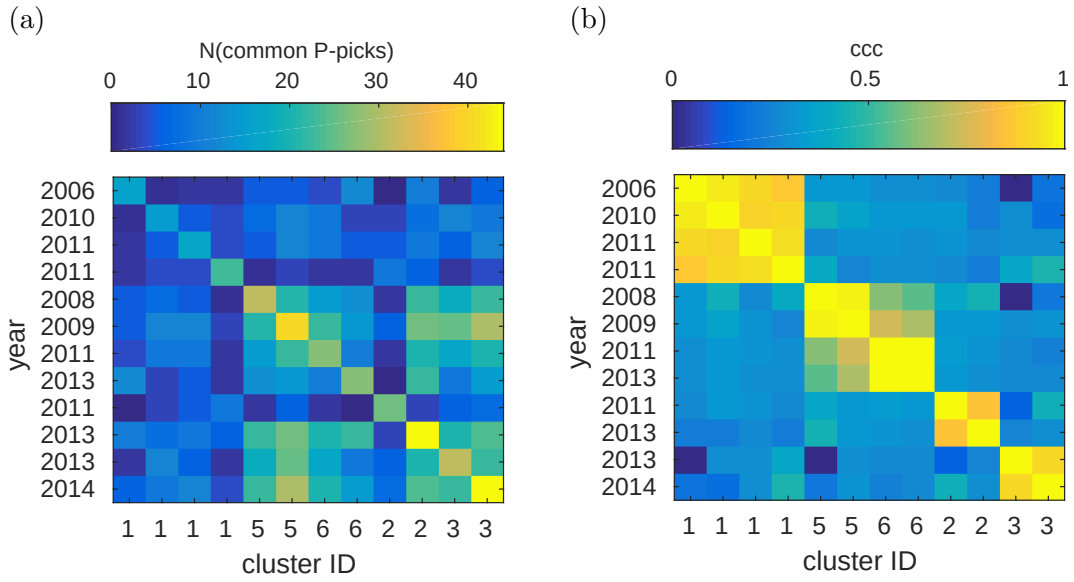

Figure 5.7.: (a) Number of P-picks at a common station and (b) cross-correlation coefficients (*ccc*) between the events involved in a repeater sequence (Table 5.1 and Fig. 5.6). The value of *ccc* equals the 68th percentile of all cross-correlation coefficients between wavelets with P-picks at common stations.

quency performed for a large fraction of the recording seismographs in 2013. Waveforms of different sampling frequency were not cross correlated.

The new numerical values for the moment magnitudes of earthquakes as presented in this thesis (and in Wollin et al. 2018a,b) for the entire 10-year period, are smaller on average resulting in $M_c = 2.1$ (see Sec. 4.3.1). The independent repeater pairs in the Western High have magnitudes smaller or equal M_c. For this reason further events associable with the sequence might be missing in the catalogue. The repeater pairs in the Cinarcik Basin have magnitudes larger than M_c. Due to the proximity of both pairs, their waveforms reach an intermediate similarity (clusters 5 and 6 in Fig. 5.7). However, both sequences are limited to pairs of events which indicates that these repeater sequences are of rather transient nature.

Our previous conclusions remain valid and longer recurrence periods of repeating earthquakes allow an estimation of the proportion of deformation being accommodated by creep. However, the loading of the respective micro-fault patches seems to be strongly mediated by moderate size earthquakes in the local vicinity. Seemingly transient repeater doublets show a substantial degree of similarity between pairs. This might either indicate the transfer of stress to a neighbouring fault patch, or, if both doublets occur on the same fault, it might indicate a rotation of the underlying stress field inducing pairwise different faulting mechanism. The occurrence of creep in this particular segment of the central Marmara Section could be be linked to gas seepages observed in the area (Tary et al. 2011). A very recent study suggests that this gas originates from over-pressured fluids in 2–5 km depth (Géli et al. 2018) which are likely to reduce normal stresses on the fault and might thus facilitate deformation and be responsible for the observation of partial creep.

6. Stress inversion of regional seismicity in the Sea of Marmara Region, Turkey[a]

Abstract In this study we derive the stress tensor and its local variations throughout the Marmara region, Turkey. Based on a recently compiled 10-year earthquake catalogue, we directly invert first-motion polarity data and quantify confidence intervals for the principal stress orientations. We find a combined strike-slip and normal faulting stress field for the Marmara region generally reflecting the overall transtensional setting. However, the results clearly show moderate local variations of the stress field. The largest (σ_1) and intermediate (σ_2) principal stresses show an average regional trend of N125°E and locally varying plunges. The least principal stress (σ_3) is well-resolved in its confidence interval and consistent throughout the region with an average trend of ∼N35°E and a subhorizontal plunge. The eastern Sea of Marmara shows local stress field orientations with pronounced strike-slip (northern part) and normal faulting (southern part) components. Along the central Marmara region, normal faulting tends to dominate, while a well-resolved strike-slip stress regime is found in the western Sea of Marmara region. Regarding the faulting mechanism of an earthquake with magnitude up to 7.4 which is expected in this area in direct vicinity of the Istanbul metropolitan region, our results imply that neither strike-slip nor normal faulting kinematics can be excluded.

[a]This chapter is an excerpt from a research article in Pure and Applied Geophysics: **C. Wollin**, M. Bohnhoff, V. Vavryčuk and P. Martínez-Garzón (2018b). "Stress Inversion of Regional Seismicity in the Sea of Marmara Region, Turkey". In: *Pure and Applied Geophysics*. https://doi.org/10.1007/s00024-018-1971-1. Received 09 May 2018, revised 01 August 2018, accepted 03 August 2018. Springer International Publishing.
The chapter is identical to the publication exept for the description of the tectonic setting of the Sea of Marmara which has been moved to the introduction of this thesis (Chapter 2.1).

6.1. Introduction

The vast majority of earthquakes are caused by failure of critically stressed faults within the seismogenic layer of the earth's crust and along active tectonic plate boundaries (e.g. Wallace 1951; Bott 1959; McKenzie 1969; Vavryčuk 2015; Hardebeck et al. 2018). Whether or not a particular fault is going to rupture is controlled by the fault's orientation with respect to the present stress field orientation thereby defining the preferred faulting mechanism to be expected in a future earthquake (Vavryčuk 2011). The Sea of Marmara region in northwestern Turkey is located along the plate-bounding North Anatolian Fault Zone (NAFZ) at the transition zone between the pure right-lateral part of the NAFZ to the east and the north-south extensional Aegean region to its southwest. This setting results in a first-order transtensional tectonic regime (McClusky et al. 2000; Le Pichon et al. 2015; Bohnhoff et al. 2016b) and in the opening of the Sea of Marmara as a pull-apart structure (e.g. Armijo et al. 1999; Le Pichon et al. 2001; Armijo et al. 2005). The submarine Marmara segment of the NAFZ currently represents a seismic gap capable of generating a major ($M > 7$) earthquake in the next decades (Parsons 2004; Bohnhoff et al. 2013; Murru et al. 2016). This translates into significant hazard and risk for the neighbouring Istanbul metropolitan area with its 15+ million inhabitants (Bas et al. 2008). Much progress has been achieved in characterizing the Marmara Section of the NAFZ with regard to potential nucleation points and rupture propagation (e.g. Hergert et al. 2011; Karabulut et al. 2011; Bohnhoff et al. 2013, 2017a). However, in order to quantify the earthquake and potential tsunami risk for the region (e.g. Yalçıner et al. 2002; Hébert et al. 2005; Latcharote et al. 2016), a key role is taken by the expected type of faulting. For its characterization, knowledge of the local and regional stress field orientation is crucial.

In this paper we study the stress field orientation in the broader Marmara region based on the recently published earthquake catalogue of Wollin et al. (2018a) which covers the time period of 2006-2016. Since the catalogue does not allow to determine a sufficiently high number of single-event focal mechanisms due to absence of moderate-size ($M > 3$) events, we calculate the stress tensor by a direct inversion of first-motion P-wave polarities of seismicity clusters throughout the study region. The resulting uncertainties of the resolved stress are discussed and expressed as intervals or areas of confidence of the marginal probability density functions (PDFs). The reliability of our results is quantified by synthetic modeling. We discuss which type of faulting can be expected for the pending Marmara earthquake and its potential consequences for seismic risk scenarios.

6.2. Data synthesis and methods

6.2.1. Earthquake catalogueand determination of first-motion polarities

Recently, Wollin et al. (2018a) combined seismic recordings (2006-2016) from the major permanent networks in the region (black dots in Fig. 2.1), including the two national networks (AFAD and KOERI), to ensure the best possible azimuthal coverage. This is crucial since the largest portion of the target fault lies below the Sea of Marmara, thus preventing the deployment of on-land near-fault seismic stations needed for the determination of reliable focal mechanisms of small to moderate earthquakes. To compile a waveform data base and subsequent hypocentre catalogue, Wollin et al. (2018a) re-picked the entire data set employing a novel automatized picking scheme. The new Marmara hypocentre catalogue reports 6,812 reliable hypocentres down to magnitude $M_w = 0.7$ for the time period 2006-2016, all of which are based on at least seven picks (including P- and S-picks) and have a maximum azimuthal gap $GAP \leq 270°$ as well as an error ellipse area of less than $A_{ell} \leq 256\,km^2$ (Wollin et al. 2018a). In this catalogue, each P-phase onset was assigned a first-motion polarity, if established with a sufficient confidence. Otherwise, the first motion was rated neutral. The signal-to-noise ratio (SNR) was used as a measure for the first-motion uncertainty and Fig. 6.1 shows the fraction of the P-wave onsets and first-motion polarities as a function of the SNR threshold. With the SNR threshold equaling 4, slightly more than half of the picks were assigned the first motion (blue distribution in Fig. 6.1a). In order to obtain a more homogeneous distribution of the first-motion measurements on the focal sphere, we later consider phase onsets measured within an epicentral distance of $\leq$ 60 km. In this way, we retained $\sim$ 50% of all picks, amongst which the fraction of well determined first motions is higher ($\sim$40% with respect to all picks, red distribution in Fig. 6.1a). Nevertheless, Wollin et al. (2018a) use 758 reference picks on 72 manually picked earthquakes to calculate the fraction of automatically determined first motions being equal or different to the manually derived values. The result of this analysis yields an error rate with respect to all measurements of $\sim$10%, i.e. on average $\sim$10% of all up- and down-polarities are erroneously flipped. Figure 6.2a and 6.2b show exemplary **U**p and **D**own first motions (i.e. compressional and dilatational or positive '+' and negative '-', respectively) of 75 P-wave onsets each, which were recorded from earthquakes of M_w between 1.7 and 3.8 at epicentral distances between 5 and 210 km.

In this study, we utilize P-wave polarities of 6,812 events. In general, the number of measured phase arrivals and first-motion polarities per event positively correlates with the moment magnitude (Fig. 6.3a and 6.3b). The bulk of earthquakes have a magnitude M_w in the range between 1.7 and 2.3 and are

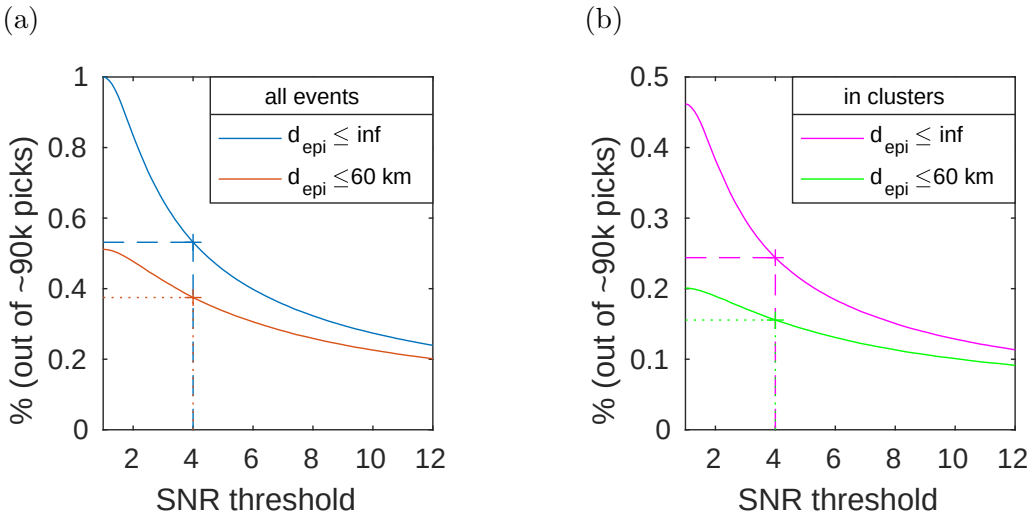

Figure 6.1.: Fraction of $\sim 90,000$ picked P-wave onsets as a function of the threshold for the signal-to-noise ratio (SNR). Picks with SNR$\geq$ 4 were assigned an up or down first motion. (a) shows onsets of all earthquakes in the catalog, (b) only those associated with a cluster for which the stress tensor was calculated. Both figures differentiate between all onsets and those measured within an epicentral distance of $d \leq 60$ km.

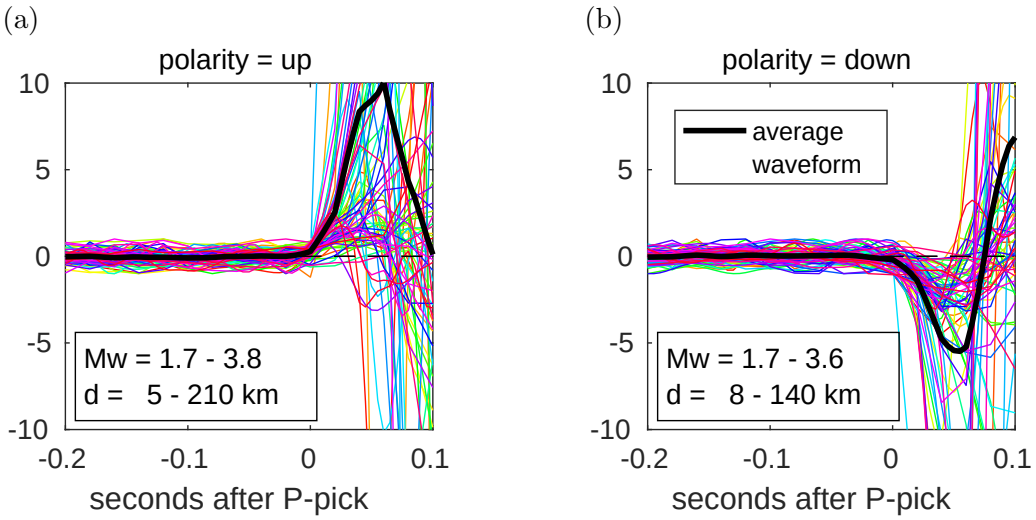

Figure 6.2.: Two sets of 75 exemplary P-wave onsets of events with M_w between 1.7 and 3.8 at epicentral distances d between 5 and 210 km with (a) down (negative) and (b) up (positive) first motions. The wavelets are normalized to the largest absolute value within 1 sec before the P-wave onset. The black graph shows the averaged wavelet.

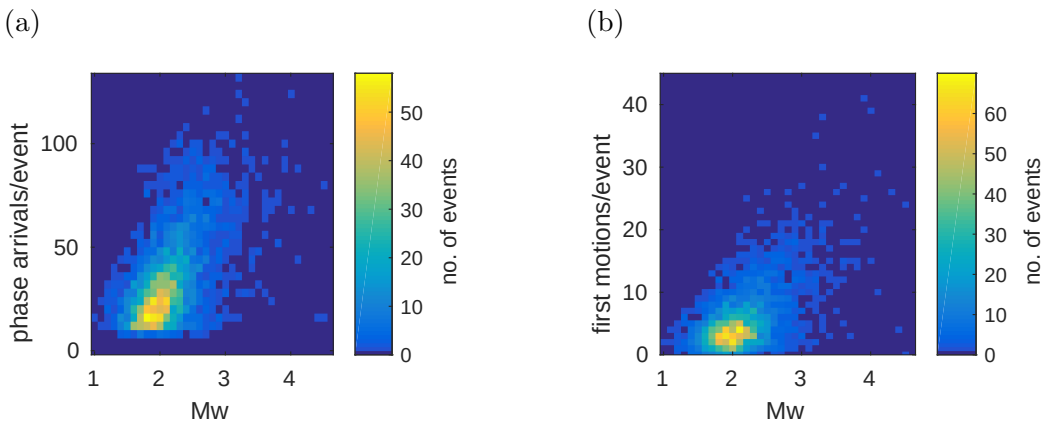

Figure 6.3.: Density plots of the number of earthquakes as a function of two parameters: (a) the moment magnitude M_w versus the number of phase arrivals (P- and S-waves) used per earthquake location, and (b) the moment magnitude M_w versus the number of acceptable "Up" or "Down" first-motion polarities per earthquake.

located with approximately 20 (P- and S-) phase readings on average. However, these events yield usually only 5 high quality first-motion polarities. This number is too small to calculate stable single-event focal mechanisms, but may be utilized to determine the stress tensor when directly inverting the combined P-wave polarities from many collocated earthquakes.

6.2.2. Clustering of seismicity and selection of polarity data

The results from the stress-tensor inversion strongly depend on the grouping of the underlying seismicity when investigating the spatial (or temporal) variations of the stress tensor (e.g. Hardebeck et al. 1999; Townend et al. 2001; Hardebeck et al. 2006; Martínez-Garzón et al. 2013; Ickrath et al. 2015; Öztürk et al. 2015; Martínez-Garzón et al. 2016a). In this study, we aim at investigating the stress field orientation along local tectonic features of particular interest as well as in areas with a pronounced spatially clustered seismic activity. We used rectangular polygons to select groups of earthquakes along fault segments and defined seismicity clusters with the '**D**ensity-**b**ased **s**patial **c**lustering of **a**pplications with **n**oise' (DBSCAN) method (Ester et al. 1996). This method essentially groups earthquakes according to the density of their occurrence, which is expressed by two parameters, N_c and r_c, the minimum number of elements and the maximum distance between elements, respectively. DBSCAN may identify arbitrarily shaped clusters and neither requires the a-priori estimation of the number of expected clusters nor some arbitrary initial clustering (k-means, Han et al. 2011) nor a termination condition (hierarchi-

Table 6.1.: DBSCAN parameters used in this study to cluster seismicity in the Sea of Marmara Region. The minimum number of events in a cluster, N_c, within a radius r_c (in km) constitute the average epicentral density in a seismicity cluster, ρ_c. Radius r_b (in km) is added to r_c to "blow up" the cluster boundary and to include some of the surrounding seismicity.

$\#_{DBSCAN}$	N_c	r_c	ρ_c	r_b
1	10	0.8	1.99	1.6
2	10	1.0	1.59	1.0
3	10	1.3	1.22	1.0
4	10	1.5	1.06	1.5
5	10	1.7	0.94	1.3
6	10	2.5	0.64	0.5
7	10	4.0	0.40	0.0

cal clustering, Han et al. 2011). We use the inter-epicentral distance as a metric and choose seven sets of N_c and r_c with decreasing density $\rho_c = \frac{r_c}{N_c}$, thus obtaining 207 nested clusters. The cloud-shaped boundary of a seismicity cluster may be defined by the union of the r_c neighbourhoods of all events associated to the respective cluster. For all cluster densities we require a minimum cluster size of $N_c = 10$ events. However, clusters of only 10 events are too small for any accurate stress inversion. After the density based clustering we thus add events located in the wider neighbourhood of a cluster defined by $r_c + r_b$ (for numeric values of the parameters see Table 6.1). Some clusters contain a similar subset of events and we only kept the largest representative and only those clusters which contain between 100 and 1000 events (see Appendix 6.A for more details regarding the usage of DBSCAN in this study and examples of the cloud-shaped cluster boundaries in dependence of different parameter sets in Fig. 6.13). In this way we obtain a set of 20 nested and overlapping clusters representing earthquake agglomerations of different epicentral density and distributional scale, potentially suitable for a stress-tensor inversion. We include three seismogenic volumes by defining longitudinal and latitudinal intervals delineating crucial portions of the Marmara Section, from east to west namely the western Basins, the central Marmara Section and the Princes' Islands Segment.

The stress-tensor inversion using the first-motion polarities requires a uniform sampling of the focal sphere. Refracted P-wave rays are emitted within narrow angle intervals and they tend to form dense concentric rings when mapped onto the focal sphere. Therefore, we predominantly used upward radiated (e.g. direct) rays for the inversion. For a source at 12 km depth, which is an average depth of the seismicity in the Marmara region, the velocity model of Karabulut et al. (2011) predicts direct rays up to an epicentral distance of 50 km. Thus, we only processed the first-motion polarities measured along

the ray paths covering epicentral distances of less than 60 km and emerging from events in the depth interval of $8 - 16$ km. This procedure significantly decreases the available first-motion measurements (Fig. 6.1b) but produces more reliable results for the resolved stress tensor.

In order to avoid oversampling of rays measured by densely collocated seismic stations, we assigned the corresponding first motion to one station, if more than 3/4 of the first motions measured at the neighbouring stations have the same sign. In the eastern Sea of Marmara, this affected the PIRES (Bohnhoff et al. 2013) and the GONAF (Bohnhoff et al. 2017b) networks, which consist of several dense near-fault seismograph arrays. The PIRES network includes local five-station arrays on the islands of Yassiada and Sivriada in direct vicinity to the Princes' Islands Segment as part of the Marmara Section (Fig. 2.1). Furthermore, the GONAF vertical arrays are distributed throughout the eastern Sea of Marmara region in near-shore locations or on the Princes' Islands (Sivriada and Büyakada) (Fig. 2.1). We processed earthquake clusters only if they contained more than 250 reliable first-motion polarities. In this way, we remained with 18 seismicity clusters which consisted of 37 to 310 earthquakes and yielded between 256 and 3118 first-motion polarities.

6.2.3. Inversion for stress from first-motion polarities

The local stress tensor is inverted from data of the spatial seismicity clusters and the selected fault branches using software package MOTSI (First **MOT**ion Polarity **S**tress **I**nversion) of Abers et al. (2001). The stress field is described by the normalized deviatoric stress tensor and the MOTSI performs a non-linear inversion with two nested grid searches. The outer search loops over the parameter space of the principal stress axis orientations and the shape ratio

$$R = \frac{\sigma_2 - \sigma_1}{\sigma_3 - \sigma_1} \,, \tag{6.1}$$

where $\sigma_1 \geq \sigma_2 \geq \sigma_3$ are the principal stress magnitudes and their positive values mean compression (Zoback 2007). For every possible stress tensor, Abers et al. (2001) calculate a set of "stress consistent focal mechanisms" and select the best synthetic focal mechanisms fitting the first-motion polarities of an individual event. The fit of observations to each imposed stress field is expressed by a score, which translates into marginal PDFs for the stress field orientations and the shape ratio. The method is not capable of determining absolute stress values.

The advantage of the approach proposed by Abers et al. (2001) is that it circumvents uncertainties, which are usually inherent in the determination of focal mechanisms and which are typically not less than 10° regarding the orientation of either of the fault planes (e.g. Bohnhoff et al. 2004). Focal mechanisms are particularly uncertain for $M < 3.5$ earthquakes, which constitute the bulk

of events used in this study (Fig. 6.3). Thus, the approach allows to include individual events with only few reliable first-motion polarities that would not lead to a reliable single-event focal mechanism otherwise. The possibility of determining the stress field from such events with $M \leq 3$ was confirmed by e.g. Robinson et al. (2000) and Ickrath et al. (2015).

We investigate how well the input data match the theoretical prediction of a synthetic first-motion distribution consistent with the stress tensor retrieved during the inversion. Uncertainties in the stress field parameters, which are expressed as marginal PDFs, may stem from: (1) insufficient observational constraints, for instance in the case of a limited directional diversity of recorded ray coverage, (2) inaccurate first-motion measurements, (3) deviations from the assumption of stress-field homogeneity within the considered cluster area, or (4) a non-negligible stress interaction between the events. Under the premise that MOTSI maximizes the fit of the searched stress-field parameters to the underlying first-motion data-set, we may quantify the adequacy of our input data with respect to the combined effects of (2)–(4).

Theoretical first-motion distributions were calculated following the approach of Vavryčuk (2011). The approach can be summarized as follows: whereas Abers et al. (2001) consider all possible plane orientations as potentially activated, Vavryčuk (2011) restricts the variety of potentially activated faults to orientations satisfying the Mohr-Coulomb failure criterion and assumes activation of a representative set of such critically stressed faults (also see Vavryčuk 2014; Martínez-Garzón et al. 2016b). The first-motion polarities along the combined rays of all sources yield polarity distributions which are characterized by three types of areas: the first and second areas display only positive and negative first motions, respectively, and the third area shows an overlap of both (Fig. 6.4c). This overlap is due to the first motions belonging to seismic events activated with a variety of different focal mechanisms. The details as well as examples of first-motion distributions in dependence of the shape ratio R are presented in Appendix 6.B.

We obtained synthetic first-motion distributions by calculating polarities along measured ray paths with respect to the stress field retrieved by MOTSI. A measured distribution and the corresponding synthetic first-motion distribution are shown in Fig. 6.4a and 6.4b. For the quantitative comparison of both distributions, we perform a weighted cross-correlation (see Appendix 6.C), where the correlated vectors are composed of the differences of fractions of up and down polarities (Eq. 6.4 and 6.5). A difference of fractions of up and down polarities was evaluated along uniformly distributed directions, where each difference of fractions may take any value between -1 and 1. Compared to a normal cross-correlation, the weighted cross-correlation C_W (Eq. 6.6) puts more emphasis on areas of the focal sphere, which are more densely populated by measured first motions, thus reducing the uncertainty of the corresponding difference of fractions. A correlation with a random first-motion distribution

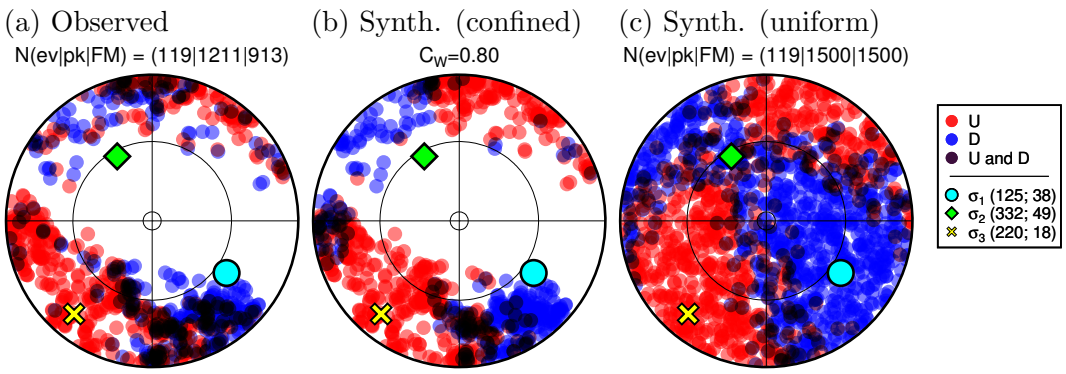

Figure 6.4.: Distributions of up and down first motions on the lower hemisphere in equal-area projection. (a) 913 first motions out of 1211 picked P-wave arrivals observed along the Princes' Islands Segment for a total of 119 seismic events. (b) and (c) show synthetically calculated first motion distributions consistent with the stress tensor, which was obtained from the inversion of the data shown in (a). Azimuths and takeoff-angles in (b) and (c) are confined to those observed (913 in total) and uniformly distributed (1500 in total), respectively.

throughout the focal sphere would yield $C_W = 0$. Areas of two first-motion distributions with opposing differences of fractions of up and down first motions yield negative contributions, such that $C_W < 0$ express dissimilarity. Values of C_W larger than 0.5 display a significant similarity.

6.3. Results and Discussion

We calculated the deviatoric stress tensor for a number of spatial seismicity clusters following the previously described methodology. In the following, we present and discuss the results for the individual study areas. First, we analyse the Princes' Islands Segment, for which we provide all methodological details. Then, we present the results for all other analysed regions.

6.3.1. The Princes' Islands Segment

Seismicity along the Princes' Islands Segment is distributed along a ∼50 km long and ∼10 km wide stripe (Fig. 6.5) parallel and south of the fault escarpment, which strikes WNW-ESE. The seafloor expression of this fault segment is situated only ∼5 km south of the Princes' Islands (Figs. 2.1 and 6.5 and Bohnhoff et al. 2013; Wollin et al. 2018a). This fault covers a prominent part of the Marmara seismic gap as it is situated in close proximity to Istanbul. It has been found to host a locked fault patch and thus represents a potential nucleation point of the pending Marmara earthquake (Bohnhoff et al. 2013;

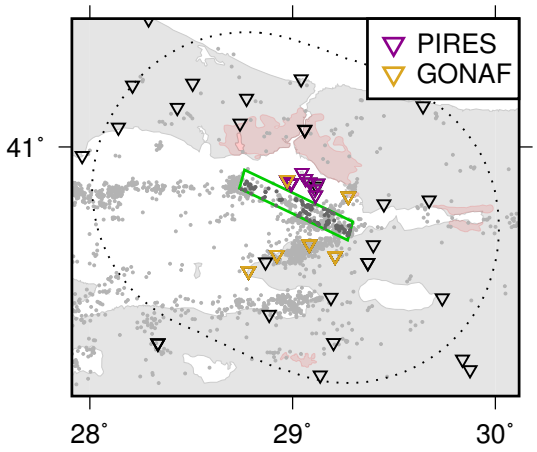

Figure 6.5.: Map of the Princes' Islands Segment with the investigated volume delineated by a coloured boundary. The contained seismicity used for the inversion is plotted in darker grey. First motions were only considered if measured at a station within 60 km epicentral distance. The corresponding stations (triangles) are situated within the dotted boundary. The permanent seismic networks with densely spaced stations, PIRES and GONAF, are marked by coloured triangles.

Ergintav et al. 2014; Wollin et al. 2018a). The stress tensor inversion for this area was based on a total of 913 first-motion polarities of 119 local earthquakes spread along the fault. Due to the seismic gap, the epicentral distribution displays large earthquake densities at the northwestern and southeasten tip of the segment. For this reason, the DBSCAN either associates the tips to different clusters or merges them along with seismicity agglomerations further to the south-east. In order to jointly investigate the stress field along the entire Princes' Islands Segment, we select seismicity located within a polygon of the above given measurements and recorded by ∼30 stations (Fig. 6.4a).

The orientations of the largest (σ_1) and smallest (σ_3) principal stress axes are given by the global maxima of the marginal PDFs obtained with MOTSI and read $(az, pl)_{\sigma_1} = (125°, 38°)$ and $(az, pl)_{\sigma_3} = (220°, 18°)$ (Fig. 6.6), thus constraining $(az, pl)_{\sigma_2} = (332°, 49°)$. The area delineated by the 95% confidence limit of the σ_3-axis orientation, $A_{95\%}(\sigma_3)$, is small and bounded to an approximately circular patch showing that the σ_3-axis is well-resolved. By contrast, the orientation of the σ_1-axis is less well-resolved as indicated by the shape and size of the corresponding area of confidence, $A_{95\%}(\sigma_1)$ (for the size, also see Table 6.2). The trend is well bound along (N125° ± 10°E), but the plunge is more uncertain. The marginal PDF for the shape ratio has a maximum at $R = 0.5$. The 95% confidence intervals stretch widely being skewed towards lower values, namely the left and right confidence limit reach zero and 0.8, respectively (Fig. 6.7).

In a mixed normal and strike-slip faulting, i.e. transtensional, environment,

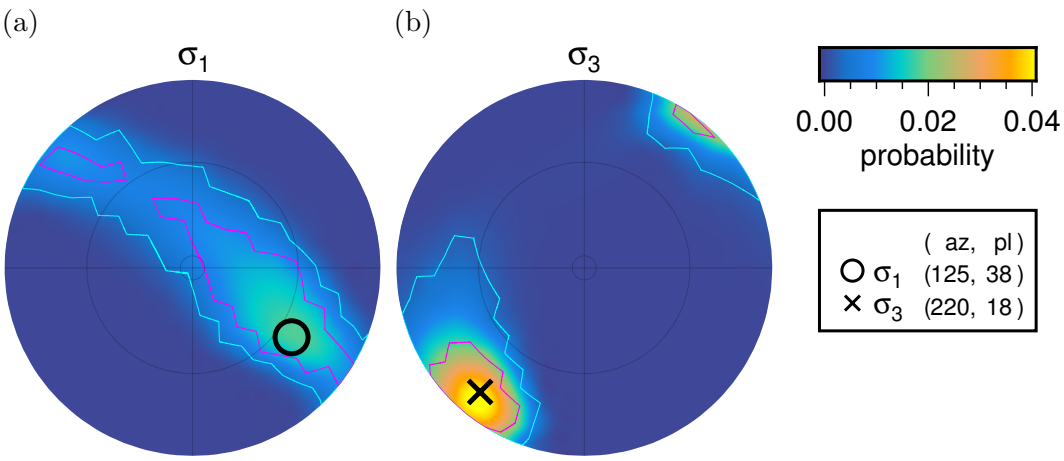

Figure 6.6.: Marginal probability distributions of orientations of the σ_1 and σ_3 principal stress axis on the lower hemisphere in equal area projection calculated for seismicity at the Princes' Islands Segment (Fig. 6.5). Contour lines delineate the 68% and 95% confidence limits where the colour scheme is as in Fig. 6.7.

low values of R indicate similar magnitudes of σ_1 and σ_2. Vanishing R is equivalent to $\sigma_1 = \sigma_2$ (Eq. 6.1) and would mean that the orientations of the σ_1 and σ_2 axes are not uniquely defined. Consequently, values of $R < 0.5$ lead to an elongated area of confidence for the σ_1-axis (which develops into a ring of constant probability in the limit of $R = 0$) and a value of $R = 0.5$ should yield circular areas of confidence for both σ_3 and σ_1 axis. The elongated marginal PDF of σ_1 might also be caused by missing observations along a ring-like area of the focal sphere. However, the trend of the σ_1-axis marginal PDF and the ring-like observational gap are noticeably different and the latter might thus only impede the proper numeric constraint of R.

In order to investigate the resolution of the stress tensor recovered for the Princes' Islands Segment, we performed additional numerical tests. We perturbed the stress-axes orientations and the shape ratios and calculated synthetic first-motion distributions (Fig. 6.8). These were again inverted using the MOTSI-software package. The simulated stress tensors had shape-ratios varying from $R = 0$ to $R = 0.8$ (corresponding to the 68% and 95% confidence intervals of the marginal probability distribution of R shown in Fig. 6.7) and stress axes which were rotated by 45° around the well resolved and thus fixed σ_3-axis. The first motions were evaluated along the observed rays and, before the inversion, 10% were randomly selected and their polarities reversed.

The results are summarized in Fig. 6.9 and show that the direction of the σ_3 is accurately retrieved in all cases. The direction of the σ_1 is well retrieved in all cases except for the $R = 0$ when the σ_1 and σ_2 have the same values and their directions cannot, in principal, be determined uniquely. However, the correct

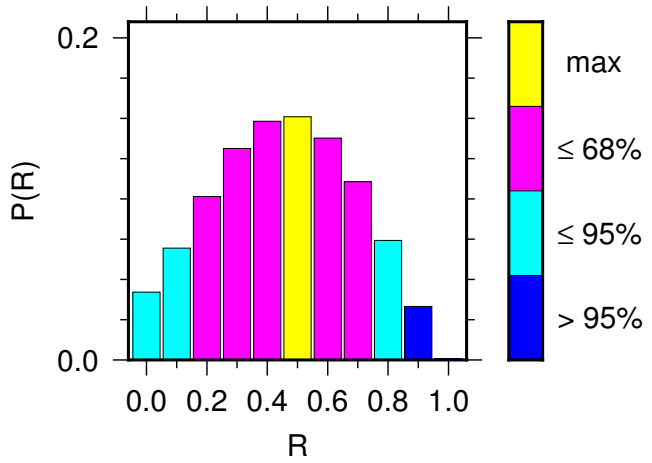

Figure 6.7.: Marginal probability distribution of the shape ratio R for seismicity at the Princes' Islands Segment (Fig. 6.5). Bar colors indicate the extent of the 68^{th} and 95^{th} percentiles.

value of the shape ratio R is not retrieved in most cases. The histograms display a stable pattern with its maximum around $R = 0.5$ irrespective of the imposed value of R. This is an indication that the histograms are misleading and we will not present them when studying other fault segments in the Sea of Marmara. As seen from Fig. 6.9, some indication about the value of R is provided by the shape of the confidence areas of the σ_1-axis. This is expressed in a smeared and ring-like shaped 68% confidence area as for $R = 0$ and nearly horizontal σ_1.

Between the synthetic first-motion distribution obtained on the bases of the stress-inversion result and the corresponding measured distribution, the weighted cross-correlation coefficient reads $C_W = 0.81$ expressing a high similarity. The remaining differences may have three reasons: (1) We expected 10% of false polarities (Sec. 6.2.1). In a first-motion distribution composed of many different seismic events, false polarities can be identified in areas that are otherwise strictly dominated by the opposite first motion, e.g. a single down first motion was falsely determined in the south-east near zero plunge (Fig. 6.4a). (2) Systematic differences may be attributed to a violation of the stress homogeneity. (3) The shape ratio R was badly resolved by the inversion. Figure 6.14 shows that the largest change in the difference of fractions of up and down first motions occurs in the neighbourhood of the piercing point of the σ_2-axis. For the first-motion distribution inverted for the Princes' Islands Segment, this area lies near the observational gap described above and thus might explain the poorly resolved shape ratio. However, a low shape ratio also provokes a broad overlap of areas with up and down first motions as observed here.

In summary, the synthetic and measured first-motion distributions display a

large similarity along the Princes' Islands Segment. This verifies the inversion results for the stress-axis orientations, particularly for the well constrained σ_3-axis. The differences between the measured and simulated first-motion distributions are rather systematic and cannot be explained by erroneous polarities. They more likely originate in an inaccurate recovery of the shape ratio R or an inhomogeneous stress field. The σ_1-axis displays a strike-slip orientation with a slight normal component and its smeared 68% confidence area indicates a transtensional stress regime.

These results imply that neither a pure strike-slip nor pure normal faulting can be predicted for the pending activation of the Princes' Islands Segment, They are in agreement with the stress tensor orientation of this region directly after the 1999 Izmit earthquake (Bohnhoff et al. 2006). The stress field orientation recovered along the Princes' Islands Segment is generally congruent with earlier findings by Örgülü (2011) who also report transtension[1] and a sub-horizontal NE-SW orientation of the σ_1-axis including a minor normal component. The NW-SE striking σ_3-axis reported here is also in accordance with observations by Öztürk et al. (2015). Their results for the σ_1-axis, however, show a vertical plunge, which supports our findings of it being weakly constrained not only due to a systematic observational gap, but also due to transtension.

[1] Using (a different definition than us) $R = \frac{\sigma_2 - \sigma_3}{\sigma_1 - \sigma_2}$, Örgülü (2011) observes $R \approx 0.7$ for the entire Sea of Marmara.

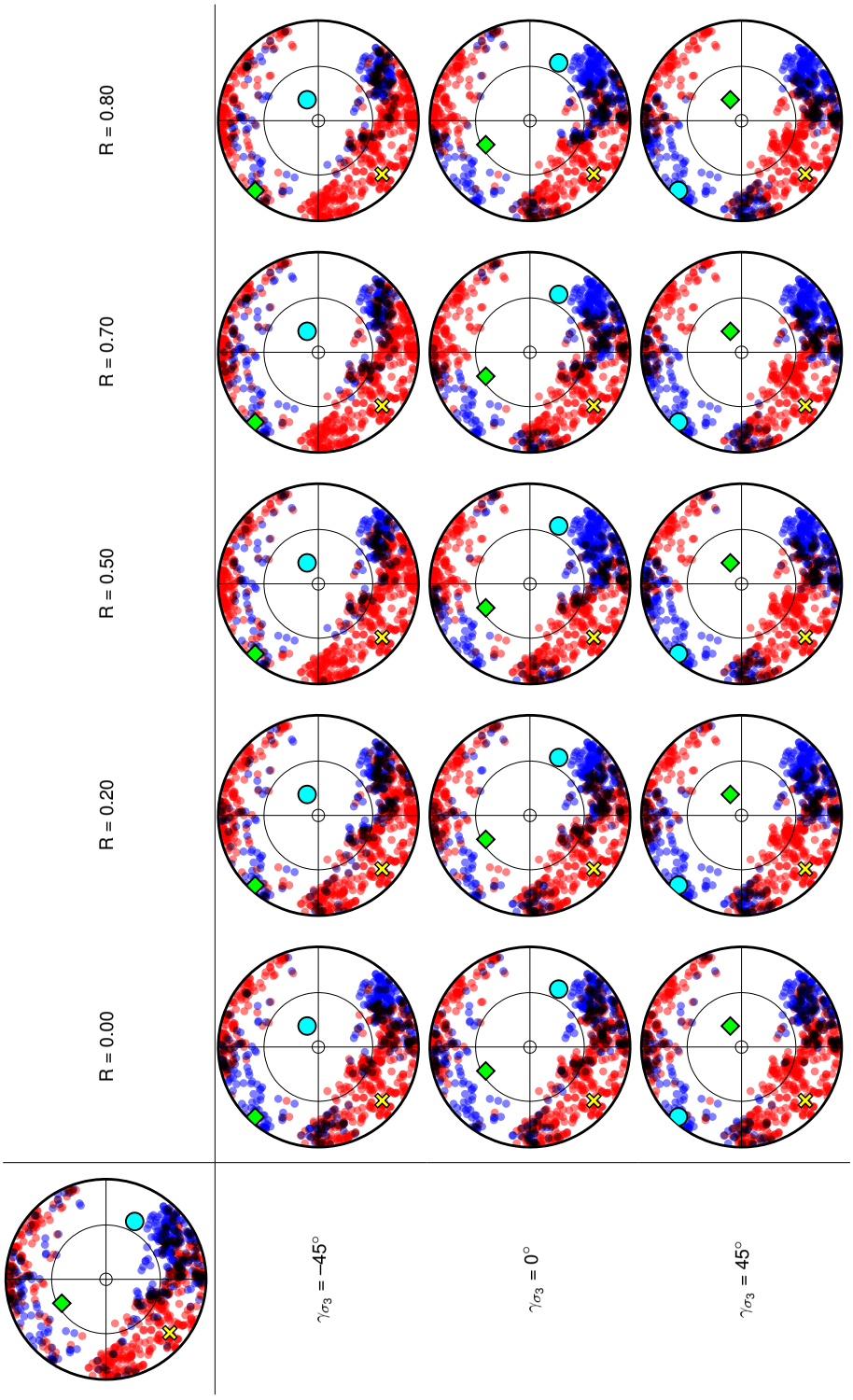

Figure 6.8.: Caption is on the next but one page.

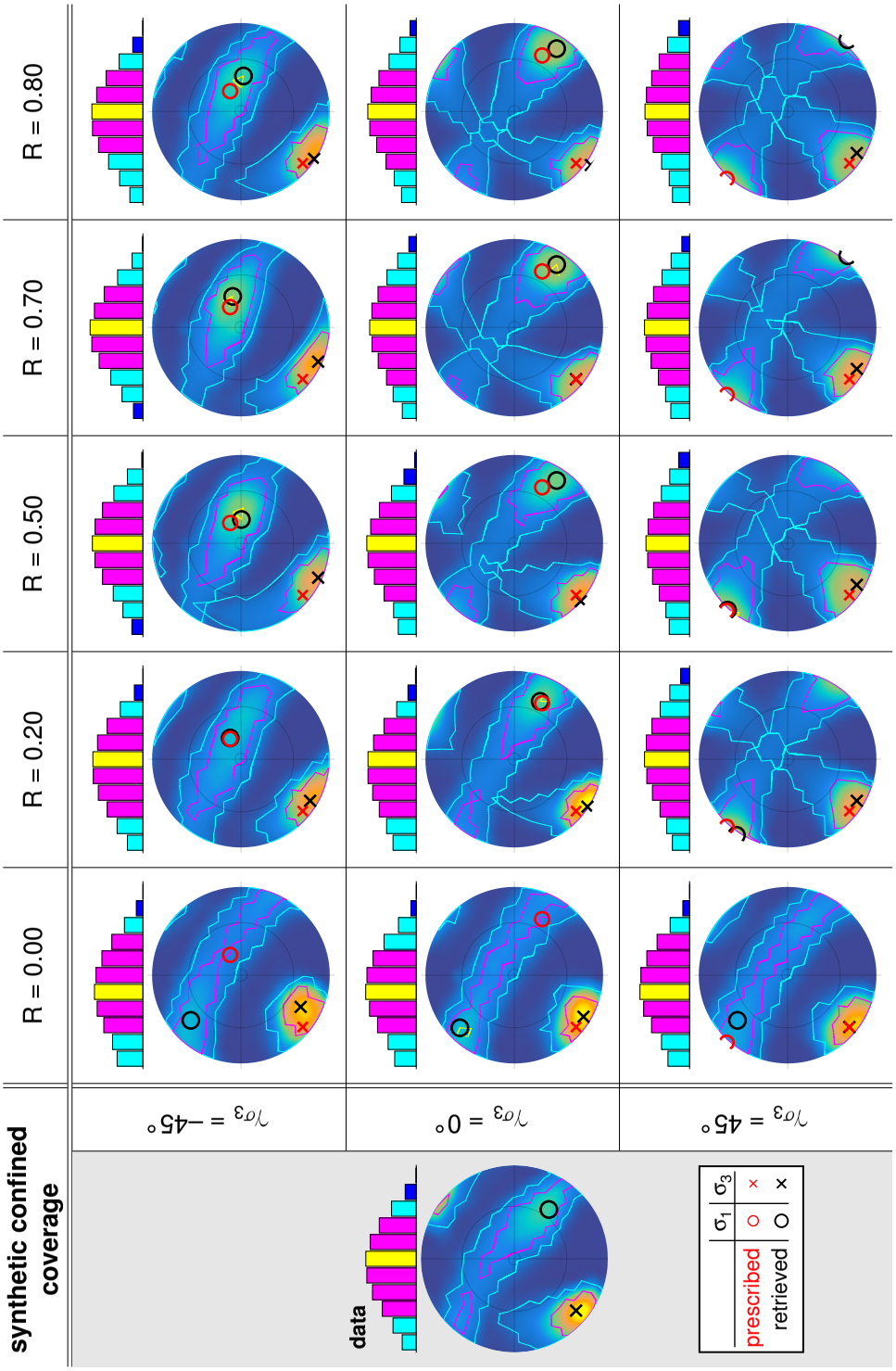

Figure 6.9.: Caption is on the next page.

Figure 6.8.: Simulated first-motion distributions representing different stress tensors with the same ray coverage as for observations. The stress axes are marked as in Fig. 6.4. Columns and rows show different shape ratios and different stress-axes orientations rotated round the σ_3-axis by the angle γ_{σ_3}. The measured first-motion distribution and the stress axes retrieved from measurements are shown in the upper left panel.

Figure 6.9.: Stress-tensor inversions of the simulated first-motion distributions shown in Fig. 6.8 where the marginal PDFs of σ_1 and σ_3 are combined. The prescribed and retrieved stress axes are indicated by red and black symbols, respectively. The stress tensor inverted from the measured data is shown in the left column.

6.3.2. Stress field in the Sea of Marmara

We found a regionally consistent well-constrained SW-NE striking σ_3-axis for all local seismicity clusters in the study area. All deviations of σ_3-axis orientations lie within the uncertainties delineated by the boundary of the area of 68% confidence. This is in correspondence with a transtensional regional stress regime as indicated by the GPS-derived velocity field (Reilinger et al. 2006) and geological findings describing the Sea of Marmara region as a pull-apart structure (Armijo et al. 2005; Acarel et al. 2014). Except for the westernmost areas of the region, the orientation of the σ_1-axis is consistent in its trend of about N125°E but generally less well constrained in its plunge, the 95% confidence interval of its marginal PDF forming a great circle in the plane spanned with the σ_2-axis. This indicates that σ_1 and σ_2 do not differ substantially in their magnitudes. Unambiguous interpretation is aggravated by observational gaps in the first-motion distributions foremost preventing the numerical constrain of the shape ratio R, which is thus not further interpreted (also see Sec. 6.3.1).

However, we obtain a significant correlation between the measured and the corresponding synthetic first-motion distributions, C_W ranging between 0.62 and 0.91, and we conclude that the first-motion measurements (1) were reliably determined, (2) fulfil the assumption of stress-field homogeneity to a large degree and (3) are representative for the calculated stress tensor within the areas of confidence. All measured first-motion distributions and the corresponding stress-inversion results are summarized in Fig. 6.10 and 6.11, respectively. Results for individual seismicity clusters are shown in Figs. 16–33 of Wollin et al. (2018b) (supplementary material) and numeric results are listed in Table 6.2 where the inversions can be identified by the abbreviation of the seismicity clusters' name in bold letters. For each stress tensor, we also calculated the 95% confidence intervals of S_{Hmax} following Lund et al. (2007). The results are summarized in Fig. 6.12 where the different faulting regimes are categorized after Zoback (1992).

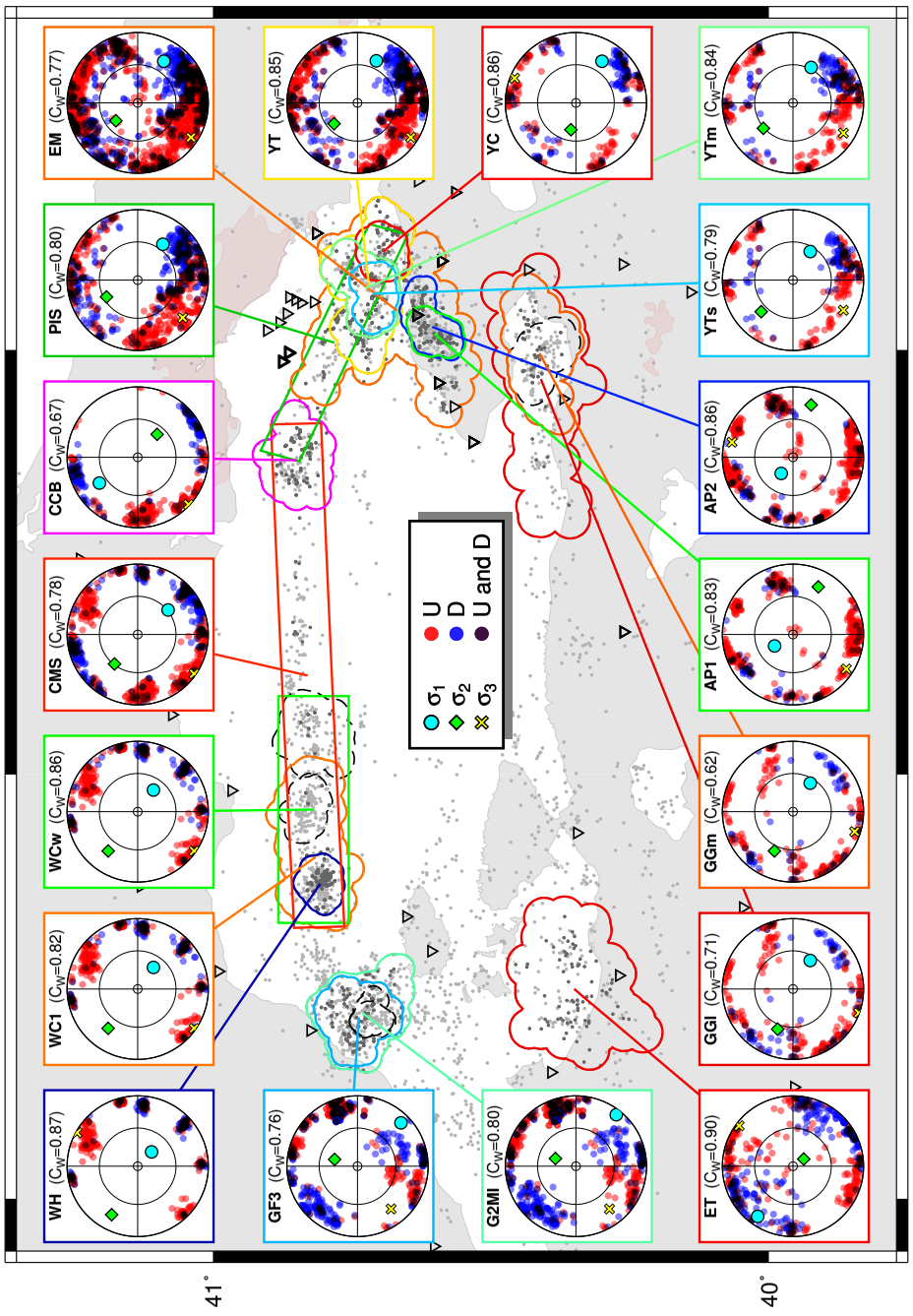

Figure 6.10.: Caption is on the next but one page.

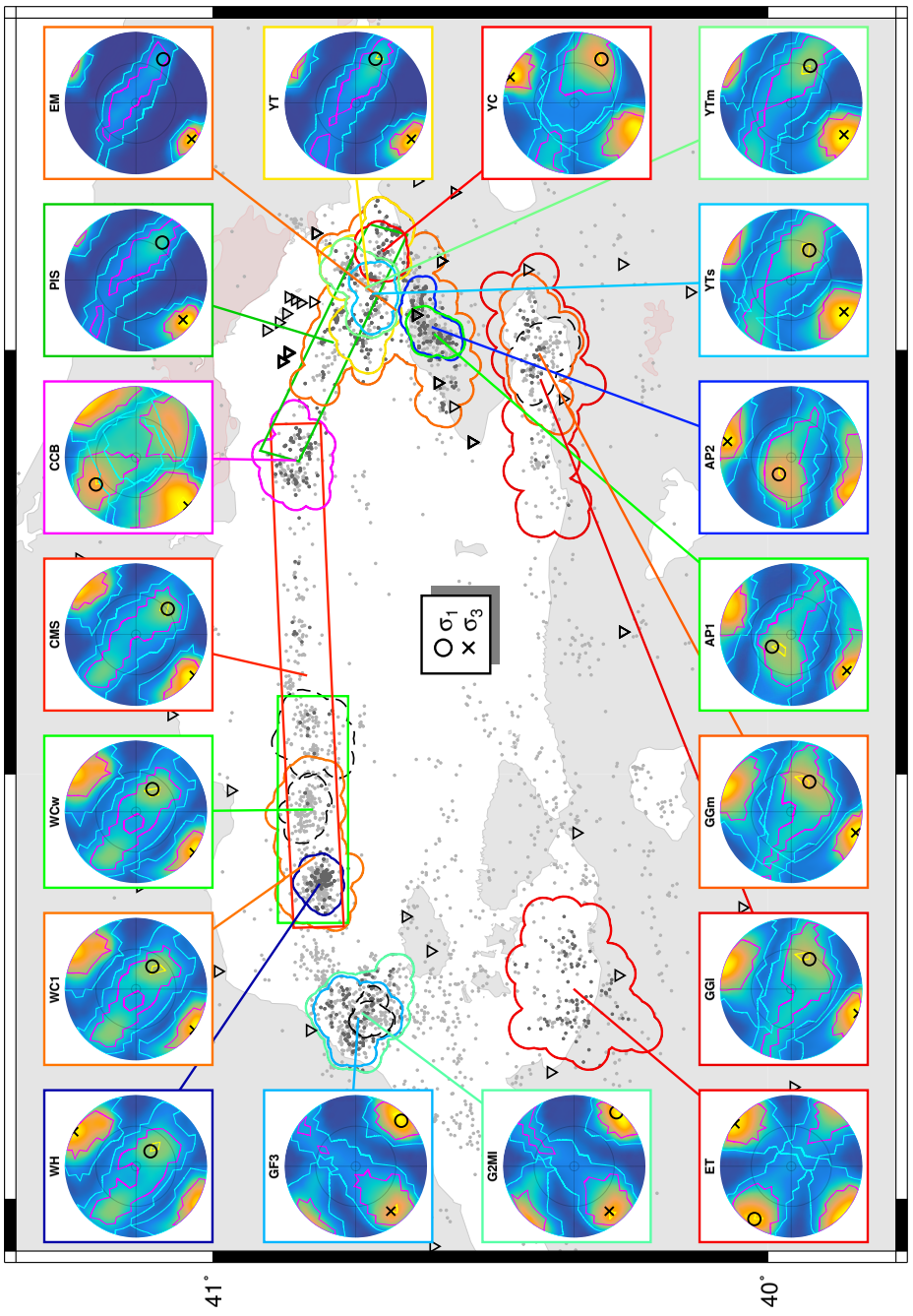

Figure 6.11.: Caption is on the next page.

Figure 6.10.: The insets show the measured first-motion distributions of local seismicity clusters in the Sea of Marmara. The clusters are delineated in the colour of the insets' frame. The title of each inset indicates the abbreviation of the cluster name in bold letters (see Tab. 6.2) and the weighted cross-correlation coefficient with the corresponding synthetic first-motion distribution, C_W.

Figure 6.11.: The insets show the combined marginal PDFs for the σ_1- and σ_3-axis orientations as obtained from the stress inversion of local seismicity clusters in the Sea of Marmara. The frame of each inset is coloured as the corresponding polygon delineating the seismicity used for an inversion. The corresponding first-motion distributions are shown in Fig. 6.10 and the numeric results are summarized in Tab. 6.2.

Eastern Sea of Marmara region

Compared to the Princes' Islands Segment (**PIS**, dark green), the σ_1- and σ_3-axis in the eastern Sea of Marmara between Yalova and Tuzla (**YT**, yellow) are slightly rotated counter-clockwise. This corresponds with the changing strike of the main fault branch further east, where it rotates from ESE-WNW to E-W. The Yalova-Tuzla cluster (**YT**, yellow) consists of several sub-clusters, of medium and small size (**YTm** and **YTs**) as well as a cluster at the coast of Yalova (**YC**). The stress-inversion results yield larger areas of 95% confidence for the principal stress axes ($A_{95\%}(\sigma_1)$ and $A_{95\%}(\sigma_3)$ in Tab. 6.2), which is likely to stem from fewer observations per cluster. The results for these sub-clusters are congruent with those obtained for the parent and the Princes' Islands cluster (**YT** and **PIS**).

Stress tensors from seismicity clusters located on the Armutlu Peninsula (**AP1** and **AP2**) indicate a predominant normal faulting stress regime with strike-slip components. This is in agreement with earlier studies observing a substantial amount of normal faulting events (Örgülü 2011; Kinscher et al. 2013; Öztürk et al. 2015). However, a substantial number of positive first-motion polarities around the pole (Wollin et al. 2018b, Fig. 27a–28a in) indicate that this region shows a spatially heterogeneous tectonic setting observed also in focal mechanisms of the 1999 Izmit aftershocks (Bohnhoff et al. 2006). In general, the weighted cross-correlation between the distributions of observed and synthetic polarities yields a high similarity coefficient ($C_W = 0.86$).

A joint inversion of the polarities from seismicity in the entire eastern Sea of Marmara (**EM**, orange) results in a stress tensor congruent with the results of the sub-clusters. The large number and the spread of seismicity over a large area leads to a dense first-motion distribution covering large parts of the focal sphere. Whilst the σ_3-axis orientation is the best resolved in the entire study, the confidence interval of the σ_1-axis delineates a ring-like area crossing the pole and striking ENE-WSW. Despite large uncertainties in the inversion results

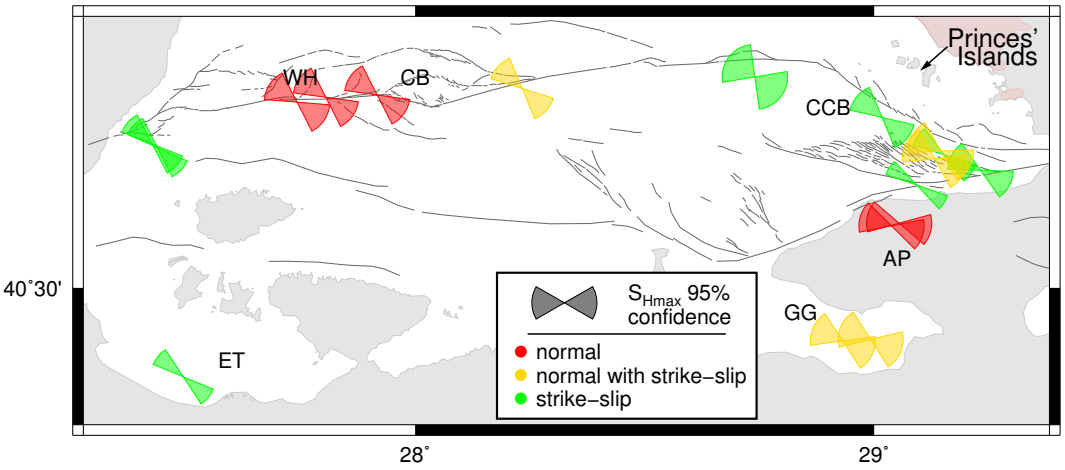

Figure 6.12.: 95% confidence intervals of S_{Hmax} for all derived stress tensors. As in Fig. 6.11, the wedges are situated at the centroids of the corresponding clusters. Different faulting regimes are colour coded and the regional abbreviations are as in Fig. 2.1.

for the individual small sub-clusters, the results indicate the decomposition of the eastern Sea of Marmara into two stress regimes, one in the north tending towards strike-slip with a normal faulting component and one in the south tending towards normal faulting, respectively (Fig. 6.12). The orientations of the least compressive stress axes (σ_3) are the same for both stress regimes.

The two seismicity clusters in the Gulf of Gemlik (**GGm** and **GGl**) south of the Armutlu Peninsula have comparatively fewer observations. The results for both marginal PDFs for the principal stress orientations are very similar and congruent with the values obtained for the offshore clusters north of the Armutlu peninsula. The stress field orientation derived for the Gulf of Gemlik is dominantly NE-SW extensional strike-slip faulting with a significant normal component (Fig. 6.12). The extended confidence intervals show, however, a larger uncertainty. Still, the measured first-motion distribution is representative for the recovered stress-field as it shows significant similarity with the corresponding synthetic first-motion distribution, i.e. $C_W = 0.62$ for the medium and even $C_W = 0.74$ for the larger cluster.

Central Marmara Section

The central Marmara Section is subject to large observational gaps. Hence, we can only perform stress inversions for three individual seismicity clusters. Two are located in proximity to the Western High (**WH** and **WC1**), and a third under the northwestern part of the Cinarcik Basin at the Istanbul Bend (**CCB**). To resolve the local stress field orientation in the best possible way, we also invert polarities along two manually selected stripes along the central

Marmara Section (**WCw** and **CMS**). The stress inversion for two seismicity clusters (two black-dashed polygons in Fig. 6.11) located at the edges of the Central Basin (CB in Fig. 2.1) were omitted due to lack of sufficient intermediate range first-motion observations. All first-motion distributions inverted here lack first-motion observations with plunge larger than 45° (Figs. 16a–20a Wollin et al. 2018b).

The resolved stress-field orientation along the central Marmara segment indicates a first-order NE-SW normal faulting stress regime with a well-constrained σ_3-axis and a bimodal marginal PDF for the σ_1-axis where the two maximums approximately enclose an angle of 90°. No pure strike-slip component is observed while the oblique plunge of σ_1 indicates a dominantly normal faulting regime (Fig. 6.12). Below the northwestern part of the Cinarcik Basin at the Istanbul Bend the stress inversion displays large uncertainties. The maximum of the marginal PDF for the σ_3-axis orientation is in agreement with that of the neighbouring central Marmara Section and the Princes' Islands Segment. However, the 68% confidence area stretches over almost 40°. The marginal PDF of the σ_1-axis is bimodal indicating a trend of about N125°E. Although the measured and synthetic first-motion distributions display a significant similarity, the weighted cross-correlation coefficient $C_W = 0.67$ is low and comparable to the C_W-values observed in the Gulf of Gemlik where the stress inversion was performed with only half as many first-motion observations. A possible explanation for the badly constrained stress field in the northwestern Cinarcik Basin is a prevalent stress heterogeneity at the Istanbul Bend where the fault changes strike abruptly and reverse faulting has been observed (Pinar et al. 2003).

Western Sea of Marmara

In the western Sea of Marmara, we performed stress inversions for: (1) a prominent offshore seismicity cluster at the eastern termination of the 1912 Ganos-rupture, and (2) scattered seismic activity around the Erdek-Tombolo region (between GM and TB as well as ET in Fig. 2.1). In contrast to all other stress regimes presented in the eastern and central Marmara region, this area displays a clear predominant strike-slip stress field with thrust components. Further, the stress tensors retrieved for two seismicity clusters offshore the Ganos Mountains (**GF3** is contained in **G2MI**, Fig. 6.11) show an elongated uncertainty of the σ_3-axis orientation which indicates a stress field with a transpressional component. While the obtained stress field clearly separates from all other areas of the region, it is in agreement with previous studies reporting transpression at this part of the Marmara Section Armijo et al. (1999, 2002), Pinar et al. (2003), Janssen et al. (2009), and Örgülü (2011). Generally, the distributions of measured and synthetic first motions show a high similarity with $C_W \approx 0.78$ (Table 6.2), supporting the reliability of our results.

The stress regime in the Erdek Tombolo (**ET**) region along the southwestern shore of the Sea of Marmara is well-resolved despite the fact that seismicity in this region is less spatially clustered than in all other regions considered here. This probably indicates a homogeneous stress field. The stress orientation is similar to that in the Tekirdak-Ganos region further to the north showing a predominant strike-slip stress regime. The 68% confidence areas of both σ_1- and σ_3-axis form circular regions.

6.4. Conclusions

We determine the stress field in the Sea of Marmara region along the main branch of the North Anatolian Fault Zone, where a major ($M > 7$) earthquake is pending in direct vicinity to the Istanbul population centre. The stress field was calculated by inverting first-motion polarities of earthquakes reported in a recently published 10-year earthquake catalogue and we tested the reliability of our results by comparing measured and synthetic first-motion distributions.

Our results show a combined strike-slip and normal faulting regime reflecting the overall transtensional setting of the region. Whereas the orientation of the least compressive principal stress (σ_3) is well-resolved and almost constant throughout the region with an average trend of ∼N35°E and a subhorizontal plunge, the largest (σ_1) and intermediate (σ_2) principal stresses show a similar trend of N125°E on average but locally varying plunges. Local variations of the stress field orientation are found throughout the region. Synthetic tests show that the shape ratio R (also called the relative stress magnitude) cannot be well constrained. However, a transtensional stress regime might be indicated by observations of elongated confidence intervals of the σ_1- and σ_2-axis.

In the eastern Sea of Marmara, the Armutlu Peninsula displays a normal faulting regime. To its north and south, around the Princes' Islands Segment and the Gulf of Gemlik, strike-slip regimes with minor or more pronounced normal faulting components prevail. Along the central Marmara Section, normal faulting tends to dominate while a strike-slip stress regime is found in the western Sea of Marmara region. Regarding the pending major Marmara earthquake, the results indicate that neither a pure strike-slip nor a pure normal faulting mechanism is to be expected. Rather, a combination of both faulting styles needs to be considered with implications to local hazard and subsequent risk. It is conceivable that several en-echelon normal faulting earthquakes in contrast to an earthquake with a significant strike-slip component, would expose the near coastal areas to a tsunami and areas further inland to substantial ground motions, respectively. Our results could be used to calculate the traction of individual faults whose strike and dip are known, to further constrain their potential faulting style.

Table 6.2.: Stress-tensor results for individual clusters.The caption continuous on the next page.

#	abrev.	name	N_{events}	N_{Picks}	N_{FMs}	C_W	az_{σ_1}	pl_{σ_1}	$A_{95\%}(\sigma_1)$	az_{σ_3}	pl_{σ_3}	$A_{95\%}(\sigma_3)$	R	$\Delta_{95\%}(R)_{l,r}$	$\#_{DBSCAN}$
1	**WH**	Western High	64	538	405	0.88	134	67	0.49	29	2	0.34	0.5	-0.4, 0.4	1
2	**WC1**	Western High to Central Basin 1	72	602	453	0.82	126	59	0.48	215	3	0.33	0.5	-0.4, 0.4	6
3	**WCw**	Western High to Central Basin wide	79	657	493	0.86	126	59	0.48	215	3	0.33	0.5	-0.4, 0.4	NaN
4	**CMS**	Central Marmara Section	138	1263	965	0.78	141	44	0.44	215	3	0.29	0.5	-0.4, 0.4	NaN
5	**CCB**	Cinarcik Basin	52	550	435	0.67	326	35	0.57	223	2	0.60	0.5	-0.4, 0.5	6
6	**PIS**	Princes' Islands Segment	119	1211	913	0.81	125	38	0.36	220	18	0.22	0.5	-0.5, 0.3	NaN
7	**EM**	Eastern-Marmara	310	3118	2484	0.76	122	31	0.31	213	11	0.12	0.4	-0.3, 0.4	6
8	**YT**	Yalova-Tuzla	155	1584	1223	0.85	114	35	0.37	213	11	0.18	0.4	-0.4, 0.4	5
9	**YC**	Yalova Coast	43	412	326	0.86	122	31	0.50	22	7	0.40	0.5	-0.5, 0.4	4
10	**YTm**	Yalova-Tuzla (medium)	56	554	392	0.84	117	43	0.45	211	18	0.37	0.5	-0.5, 0.4	4
11	**YTs**	Yalova-Tuzla (small)	39	389	282	0.79	121	51	0.49	211	18	0.42	0.5	-0.5, 0.4	3
12	**AP2**	Armutlu 2	104	1007	839	0.86	306	67	0.41	14	12	0.32	0.5	-0.4, 0.4	2
13	**AP1**	Armutlu 1	79	753	627	0.83	328	65	0.45	213	11	0.33	0.5	-0.4, 0.4	1
14	**GGm**	Golf of Gemlik (medium)	37	310	256	0.61	121	51	0.48	198	9	0.45	0.5	-0.5, 0.4	6
15	**GGl**	Gulf of Gemlik (large)	42	351	285	0.72	121	51	0.49	200	1	0.42	0.5	-0.4, 0.4	7
16	**ET**	Erdek Tombolo	74	679	499	0.91	305	14	0.44	37	5	0.39	0.5	-0.4, 0.5	7
17	**G2MI**	Ganos to Marmara Island	102	871	682	0.79	128	8	0.31	232	24	0.40	0.5	-0.3, 0.4	4
18	**GF3**	Ganos Fault 3	86	741	583	0.76	135	14	0.32	232	24	0.40	0.5	-0.3, 0.4	3

Table 6.2.: The rows are sorted according to the insets' appearance in clockwise sense in Fig. 6.11, beginning with the inset in the upper left corner. Azimuths (az) and plunges (pl) are given in degrees (°). $A_{95\%}$ is the fraction of the area on the unit sphere that the 95% confidence limits of the stress axes σ_1 and σ_3 occupy, and $\Delta_{95\%,l/r}$ are the left and right limits of the 95% confidence interval of the shape ratio R. The column $\#_{DBSCAN}$ identifies the parameters used during the density based clustering to define the local selection of seismic events (Tab. 6.1). Manual selection of the seismicity is marked by NaN.

6.A. Density based clustering

Given a set of elements for which a metric is defined, **D**ensity-**b**ased **s**patial **c**lustering of **a**pplications with **n**oise (DBSCAN) (Ester et al. 1996) uses two parameters, (1) N_c, the minimum number of elements, and (2) r_c, the maximum distance between elements, to define a cluster-density and to group the set of elements. DBSCAN categorizes the set of elements into three groups: (1) core-points define a cluster of elements where the sets of core-points of different clusters are disjunct; (2) border-points may belong to several clusters and (3) noise are outliers that are not associable to any cluster. The algorithm is deterministic regarding the separation of core-points and a boundary including core- and border-points may be defined by the union of the r_c neighbourhoods of the core-points. We "blew up" the set of events associated to a cluster by calculating the union of $r_c + r_b$ neighbourhoods of its core- and border-points. We added all events within this boundary to a cluster, condoning the intersection of clusters. An example of how these three parameters may define clusters of different size and density is given in Fig. 6.13 for four sets of N_c, r_c and r_b (the parameters used in this study are summarized in Table 6.1). Despite being calculated with different sets of parameters, some of the "blown up" clusters consist of almost the same subset of earthquakes. We define the similarity of two subsets as the fraction of the number of earthquakes in their intersection over those in their union. If this fraction is larger than 0.9, the two subsets are considered similar and only the larger one is kept as a representative.

6.B. Synthetic first-motion polarity distributions

We apply the theory on the mechanics of faulting as presented in Vavryčuk (2011) and Vavryčuk (2015) (see also Martínez-Garzón et al. 2016b) to derive distributions of first-motion polarities on the focal sphere from stress field parameters.

Given the orientation and shape ratio of the principal stresses, the shear and normal stresses acting on an arbitrary plane are functions of its orientation.

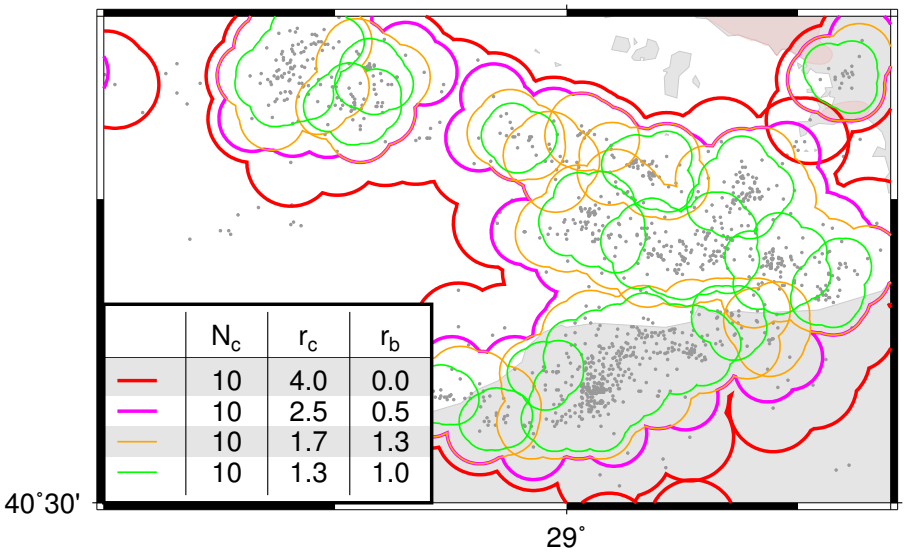

Figure 6.13.: Results of density based clustering (DBSCAN) applied to the seismicity in the eastern Sea of Marmara with four different sets of parameters N_c, r_c and r_b emphasizing clusters of increasing density. N_c is the minimum number of earthquakes within an epicentral distance r_c, and r_b is an additional radius that defines the cluster boundary.

In the Mohr-Circle diagram every pair of shear and normal stress represents a possible fault orientation. For activated faults, the shear stress should exceed the critical threshold t_c given by the Mohr-Coulomb failure-criterion

$$t_c = C + \mu(\sigma_n - p), \tag{6.2}$$

where σ_n denotes the normal stress, i.e. the normal component of the traction $\boldsymbol{t}$. Here compressional stress has positive sign (convention in rock mechanics Shearer 1999; Zoback 2007) and the parameters in this equation are dimensionless, because we normalize the stress tensor by fixing the stress magnitudes to the values $\sigma_1 = 2$ and $\sigma_3 = 0$ (e.g. Vavryčuk 2015; Martínez-Garzón et al. 2016b). The friction $\mu = 0.6$ is chosen to reflect commonly accepted values (Byerlee 1978; Zoback 2007; Vavryčuk 2015; Martínez-Garzón et al. 2016b) and the cohesion $C = 0.2$ and the pore pressure $p = 0.5$ are adapted such that the Mohr-Coulomb failure-criterion well penetrates into the outer Mohr-Circle of normalized stress magnitudes. The slip vector is parallel to the shear stress and together with the fault normal constrains a focal mechanism. The first-motion polarity of a P-wave along some ray $\boldsymbol{x}$ was then calculated after Shearer (1999),

$$f(\boldsymbol{x}) = sign(\boldsymbol{x} \cdot \dot{\boldsymbol{M}} \cdot \boldsymbol{x}) \tag{6.3}$$

where $\dot{\boldsymbol{M}}$ is the time derivative of the moment tensor and $f = \pm 1$ is equivalent

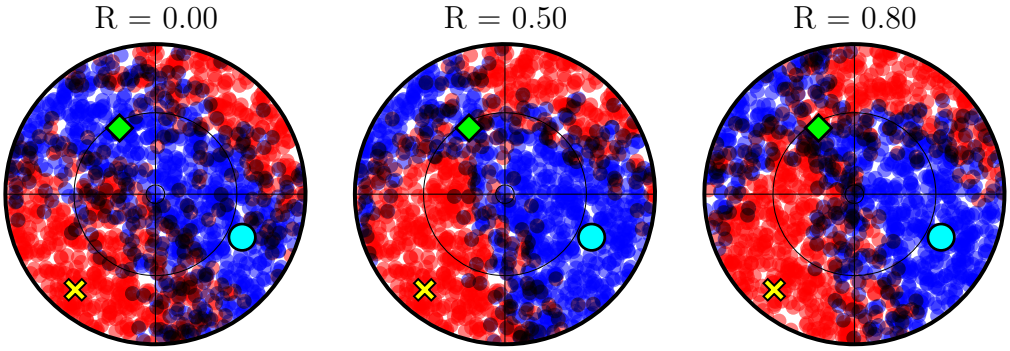

Figure 6.14.: Synthetic first-motion distributions for three different shape ratios (Eq. 6.1). Symbols are as in Fig. 6.4.

to an up and down first motion, respectively.

Figure 6.14 shows three exemplary synthetic first-motion distributions calculated for the same stress-axis orientations but for three different values of the shape ratio R (Eq. 6.1) where the first motions were evaluated along uniformly distributed rays. The distribution for $R = 0$ is rotationally symmetric around the σ_3 axis (yellow 'x') and represents a pure transtensional stress regime. With increasing R the neighbourhood of the σ_2-axis is increasingly populated with positive first motions until, towards a transpressional stress regime at $R = 0.8$, they begin to dominate there. At $R = 1.0$, the rotational symmetry would be established around the σ_1-axis.

6.C. Weighted cross-correlation of first-motion distributions

Let us consider a circular patch P of the focal sphere which is centred around the piercing point of some unit vector $\boldsymbol{r}$. We then search the rays with an up polarity piercing the focal sphere within this patch and define their total number as $N_u(P)$. Accordingly the number of down first motions piercing the focal sphere through the patch P is given by $N_d(P)$. The difference of fractions of first-motion polarities within P is then given by

$$\varrho(P) = \frac{N_u(P) - N_d(P)}{N_u(P) + N_d(P)} , \tag{6.4}$$

which is not defined for patches without any piercing rays. If the nonempty patch P contains for instance

1. only up-polarities, i.e. $N_d(P) = 0$, then $\varrho(P) = 1$,
2. only down-polarities, i.e. $N_u(P) = 0$, then $\varrho(P) = -1$,

3. as many up- as down-polarities, then $\varrho(P) = 0$.

For a set of M equally sized, non-overlapping and non-empty patches P_m, i.e. patches pierced by at least one ray, where $m = 1, ..., M$, we obtain a vector of differences of fractions

$$\boldsymbol{\varrho} = (\varrho_1, ..., \varrho_M) \; . \tag{6.5}$$

The weighted cross-correlation coefficient between two first-motion distributions represented by the vectors $\boldsymbol{\varrho}_1$ and $\boldsymbol{\varrho}_2$ finally reads

$$C_W(\boldsymbol{\varrho}_1, \boldsymbol{\varrho}_2) = \frac{\sum_{m=1}^{M} \varrho_{1m} \cdot \varrho_{2m} \cdot N(P_m)}{\sqrt{\sum_{m=1}^{M} {\varrho_{1m}}^2 \cdot N(P_m)} \sqrt{\sum_{m=1}^{M} {\varrho_{2m}}^2 \cdot N(P_m)}} \quad , \tag{6.6}$$

where $N(P_m) = N_u(P) + N_d(P)$ represent the total number of first-motion polarities (up or down) measured within the m^{th} patch P_m such that their sum $\sum_{m=1}^{M} N(P_m)$ equals the total number of rays or polarities constituting a first-motion distribution. C_W thus emphasizes patches containing many rays for which a better estimate of the difference of fractions of up and down first motions ϱ_m can be assumed.

7. Closing remarks and outlook

And Scheherezade perceived the dawn of day and ceased saying her permitted say. Then quoth Dunyazad, “O my sister, how pleasant is thy tale, and how tasteful; how sweet, and how grateful!” And Scheherezade replied, “And where is this compared with that I could tell thee this coming night, if I live and the King spares me?”

Said the King in himself, “By Allah, I will not slay her until I hear her story, for her tale telling truly is wondrous.”

Arabian Nights, translated by Sir Richard F. Burton

Sea of Marmara The aim of this thesis was to shed light on the seismotectonic setting of the Sea of Marmara region which is presumably developing towards a major (magnitude $M > 7$) earthquake posing a significant risk to the second largest European urban agglomeration, Istanbul. As a core result, the thesis presents an improved earthquake catalogue for the Sea of Marmara region which covers a $\sim 10\frac{1}{2}$ year period (2006–2016). The catalogue is based on the automatic evaluation of seismic waveform recordings from several permanent seismic networks. These include the two major national networks which had been operated and evaluated separately for the respective time period. Application of a modified automatic picking scheme which was tuned with manual reference picks, allowed for the consistent timing of P- and S-wave onsets. By means of an iterative travel-time inversion, earthquake locations were obtained for over one half of the previously detected earthquakes. Apart from illuminating active fault segments and their kinematics, the catalogue draws the contours of several quiescent fault patches and serves as an input for two subsequent studies which report (1) on the detection of micro earthquakes repeatedly activating the same fault (so called repeating earthquakes) and presumably indicating the creeping deformation of the surrounding fault structure along the western fault segment in the Sea of Marmara and (2) on the underlying stress field around local seismicity clusters in the area which varies between strike slip and normal faulting orientation and is of transtensional nature on the large scale.

The more active northern branch of the North Anatolian Fault, termed Marmara Section here, runs offshore. Thus, long term measurements of the elastic response or long-term strain of the seabed, as usually performed by means of stationary surface equipment like seismometers or GPS receivers, or methods involving remote sensing, are challenged or inhibited by the extended water body of the Sea of Marmara. Any long term study involving time periods exceeding the operational lifetime of any ocean bottom equipment must rely on a dense, land based station network which reduces azimuthal gaps as much as possible. For our seismological study, the joint evaluation of the two largest seismological networks, the national networks of AFAD[1] and KOERI[2], particularly improved the epicentral accuracy of earthquake locations. Nevertheless, uncertainties in the focal depth for earthquakes located "under the open sea", as for instance along the Marmara Section between the Western and Central High, are larger than in areas with adequate station coverage like around the Princes' Islands or the extended Ganos Segment.

The modified automatic picking scheme processed ~ 560.000 three component waveforms and timed ~ 360.000 P- and S-phases. Out of these, ~ 165.000 were selected during an iterative travel-time inversion for earthquake hypocentres. In this way, we obtained 6812 absolute and 4407 relatively relocated

[1] Disaster and Emergency Management Presidency of Turkey
[2] Kandilli Observatory and Earthquake Research Institute

hypocentre locations forming a consistent long term observation of regional seismic activity in the Sea of Marmara. The seismicity distribution confirms the existence of an aseismic patch along the Princes' Island Segment and allows for the identification of two other aseismic patches along the central Marmara Section further to the west.

A recent study by Jiang et al. (2016) distinguishes between strike-slip faults hosting earthquakes smaller or larger than $M \sim 7$ and discusses the possibility that the rupture planes of the latter might extend into the upper mantle not only inducing a larger stress-drop. According to their model, both scenarios would also cause distinct seismic responses during the early and intermediate loading phase of the fault, the earlier producing noticeably more microseismicity than the latter which appears almost quiescent due to a prolonged loading of the seismogenic crust. As an example for this behaviour the authors list the 1999 Izmit earthquake amongst others. With respect to our results for the Marmara Section, it is worth noting, that the aseismic patches identified in the west and east (around Tekirdag Basin and the Princes' Islands, respectively) are clearly underlined with seismicity whereas this behaviour is much less pronounced at the aseismic patch below the Central High.

The newly calculated focal mechanisms in a bulk, suggest a transtensional stress-field for the region. Individual reverse faulting mechanisms indicate the existence of subsidiary faults and fault step overs (possibly similar to those described by Vavryčuk et al. 2018) which are likely attributed to the ongoing structure development in the Sea of Marmara. These results are congruent with the results from the stress-tensor inversion of first-motion polarities measured on local earthquake clusters. Synthetic tests show that although the numeric value of the shape ratio (or relative stress magnitude, R) is not well constrained, the transtensional character of the central and eastern Sea of Marmara may be indicated by elongated confidence intervals of the largest and intermediate principal stresses (σ_1 and σ_2, respectively). The same tests also show, that the stress axis orientations were reliably recovered within the confidence intervals. In the eastern and western Sea of Marmara Region strike-slip regimes dominate. Predominantly normal stress-field orientations are observed along the central Marmara Section and the Armutlu Peninsula.

On the basis of the here presented catalogue, several sequences of repeating earthquakes were identified in the Western High and the Central Basin. Along the San Andreas Fault, the recurrence interval and the magnitude of a so called repeater sequence have been related to the fraction of large scale deformation being accommodated by creep. However, the consulted repeater sequences there are of at least one order of magnitude smaller and consequently display a regular recurrence. The repeater sequences in the Western High with $M_w < 2.0$ are likely to be incomplete and the recurrence interval of another sequence with $M_w \sim 2.5$ is mediated by an event of moderate magnitude. Interestingly, the locations of the repeater sequences in the Sea of Marmara spatially correlate

with areas where substantial gas-seepage has been detected. A recent study reports that the seepages are related to over pressurized fluids in 2–5 km depth and to shallow seismicity in the area (Géli et al. 2018). It is conceivable that these fluids are also responsible for the partial creep observed in this study although the repeaters and the mediating intermediate seismicity occur in larger depths and the here presented catalogue of relative relocations indicates a separation of deep and shallow seismicity.

The observation of partial fault creep in the western central Marmara Section spatially correlates with a normal faulting stress regime which is framed by strike-slip stress regimes to the east and west. For the framed fault segment this suggests a reduced stress accumulation from the right-lateral far field deformation and in consequence a reduced probability for hosting the nucleation of the pending major earthquake. Nucleation seems more likely in one of the identified aseismic patches adjacent to the creeping segment in the west or further in the east, below the Kumburgaz Basin or along the Princes' Islands Segment, respectively. An increased probability for a nucleation towards the east is ambivalent regarding the hazard for the city of Istanbul. Whereas it inflicts a shortened response time on the one hand, on the other it reduces the implications from a rupture directed towards Istanbul, which would have an increased peak ground acceleration as a consequence.

The overall transtensional stress regime in the area segregates into strike-slip as well as normal faulting regimes along the fault system. This indicates that beyond the end-members of discussed faulting types for the pending major earthquake, namely a pure strike-slip or a pure normal faulting, also combinations of the two must be taken into consideration with their individual consequences for ground shaking and tsunami generation. Our results could be used to estimate the instability of faults if their geometries are known (Vavryčuk 2015).

Several tomographic studies have been conducted in the Sea of Marmara. Most prominent are a 2-D wide-angle seismic profile (Bécel et al. 2009) and a 3-D velocity model for the sediment basins. However, in order to further increase the accuracy of earthquake hypocentres a 3-D velocity model for the seismogenic layers is needed. Such project seems most feasible in the eastern Sea of Marmara, where the PIRES and GONAF networks provide near-fault coverage and overall station density is large. A tomographic study in this area could possibly confirm results of a recently build 3-D lithospheric-scale structural model based on gravity measurements and indicating that gravitational anomalies there stem from density contrasts in the upper-middle crust (Gholamrezaie et al. 2018).

Any extension of these efforts to the entire Sea of Marmara would require seismic measurements on the sea floor. Numerous researchers and institutions have launched campaigns deploying Ocean Bottom Seismometers (OBS) (Sato et al. 2004; Schmittbuhl et al. 2015; Yamamoto et al. 2015; Géli et al. 2018)

including KOERI. However, the operational intervals are comparatively short (2–4 months) and the targeted recording density proved difficult to meet due to regular failure of the stations. Anyway, mainly the short term nature of these campaigns reduces the chance to collect sufficient data that is equally well recorded on the surrounding land based seismometers, which impedes joint evaluation. An alternative approach is to further increase the density of land based stations in coastal areas favourably in the form of borehole arrays following the example of the GONAF[3] borehole network in the eastern Sea of Marmara (Bohnhoff et al. 2017b) where the deeply buried sensors achieve an additional reduction both, in noise and in the detection threshold in vicinity of the station array. However, in order to extend a significantly reduced detection threshold into offshore areas in immediate proximity to the fault, recordings from the seabed are indispensable. A favourable but ambitious possibility to realize this would be a sea-based borehole array where the currently existing borehole network would be best complemented with an installation near the Princes' Islands fault segment, possibly centred between the Islands and the Armutlu Peninsula.

The recently emerging technique of using telecommunication optical fibre cables for earthquake detection could also proof of high benefit to permanently sample seismic signals from the floor of the Sea of Marmara. Different approaches allow (1) for a dense spatial sampling of ground motion along the full length of the cable over up to 100 km (distributed acoustic sensing or DAS, e.g. Lindsey et al. 2017; Jousset et al. 2018) but also (2) for single event detection along transoceanic installations (frequency metrology interferometry, Marra et al. 2018). Whereas the latter method is intended to detect earthquakes in the oceanic plates, the former has only been tested on land. However, as telecommunication fibre optic cables already exist in the Sea of Marmara too (TeleGeography 2018), this highly relevant and seismic risk prone region could serve as a laboratory to test the acquisition system with regard to micro seismicity below sea floor for the first time. As for the oceans, the capability to record seismicity in the long term from the otherwise widely inaccessible sea floor in the Sea of Marmara would be invaluable for further seismotectonic studies there.

Methods An automatic P- and S-phase picker is developed and applied to regional seismicity. Relatively few parameters had to be adapted for its application to local seismicity. At the core of this picking algorithm is the Akaike Information Criterion (AIC, after Maeda 1985) which is applied to rolling as well as to nested windows of the examined waveform. This procedure allowed for the definition of left- and right-sided uncertainty bounds of P- and S-picks.

The here proposed and applied algorithm iteratively uses a set of characteristic functions to map windows of the recorded wavelet to other time series, e.g.

[3]Geophysical Observatory at the North Anatolian Fault

kurtosis (4th order higher order statistics) and AIC. This is done with the aim to emphasize the features of seismic phase onsets in such a way that the latter can ultimately be defined by some logical expression, e.g. in simple words: "the phase onset is the minimum of the AIC when applied to the wavelet in the temporal neighbourhood of the kurtosis maximum." Although the algorithmic design was guided by possibly broad applicability, the approach strictly defines the decision process towards the pick of a phase onset. This has the advantage that the conclusion of an individual result can be easily retraced. On the other hand, spuriously picked phase onsets are frequently obtained and must be sorted out by superordinate rules, like for instance certain demands regarding a wavelet's energy distribution or regarding the consistency within a set of picks after travel-time inversion.

However, contemporary developments in computer science have established the wide spread use of so called machine-learning algorithms which in order to achieve efficient categorization intrinsically "learn" to extract the decisive features of the targeted objects. This approach relies on very large datasets and, during the training phase, on the correlation of preliminary and expected categorization results. A widely discussed drawback of applied machine learning is that the features on which categorization decisions are finally based on, are not necessarily intuitive and that the process resembles a black box.

Still, as this data driven approach not only promises precise and fast onset determination but also a high degree of generalization capability, it would be desirable to use machine-learning algorithms to time seismic phases. Yet, recent seismological applications of machine learning have focused on spatial categorization, i.e. on crude location of earthquakes, or forecasting of aftershocks (DeVries et al. 2018; Perol et al. 2018), and early propositions for picking algorithms which relied on the machine-learning strategy of neural trees, did not find wide spread application (e.g. Gentili et al. 2006). Possibly, a renewed attempt could be done by using the here proposed rolling Akaike Information Criterion and its characteristic behaviour around a seismic phase onset, to feed a Hidden Markov Model approach. The latter has already been used in a similar way to detect volcanic tremors (Beyreuther et al. 2008; Hammer et al. 2012).

Stress-inversion results obtained through direct inversion of first-motion polarities were independently verified using synthetic first-motion distributions. These were calculated by integrating the first motions of many critically stressed fault planes where criticality obeyed the Mohr-Coulomb failure criterion. Measured and synthetic first-motion distributions were compared via the difference of fractions of Up and Down first-motion polarities within a patch of the focal sphere. Assuming exclusively correct fist-motion measurements, the deviation from the measured to the synthetic distribution allows the inference of how accurately the physical assumptions are met which the inversion requires, i.e. most importantly for instance the stress-field homogeneity. The

presented synthetic first-motion distributions could also be used to perform a "truly direct" stress-tensor inversion from first-motion polarities[4]. As in this study, such an approach is advantageous in situations where many earthquake locations but only few reliably determined first motions per event are available and the calculation of focal mechanisms would yield very large uncertainties.

[4]This is in contrast to the software used in this study (MOTSI, Abers et al. 2001) which performs a "detour" by searching for a focal mechanism that fits best to the first-motion distribution belonging to an individual event.

A. Appendix

A.1. Automatic picking of seismic phases of induced earthquakes

In order to achieve near real-time supervision of seismicity during a hydraulic stimulation, a simple but fast STA/LTA trigger was applied in order to automatically pick P-wave onsets (Kwiatek et al., 2018)[1]. These P-picks which were obtained from 22 sensors in total, usually yielded sufficiently precise hypocentre locations to reliably estimate earthquake magnitudes. The thus acquired rate of seismicity and the moment release successfully formed the basis for the regulation of the stimulation which was guided by an action plan categorized into three stages of alert. However, manual reprocessing which included picking of several S-wave onsets, regularly improved locations and magnitude estimates and was thus mandatory for $M_w \geq 1$ events located near the injection well. Although manual picking of hundreds of events with $M_w \geq 0.5$ during a post-processing campaign, and the subsequent relative relocation of earthquakes yielded precise insights into the seismicity distribution around the well, further analysis of its spatio-temporal development is planed. However, this requires the timing of the S-phases of several thousands of further earthquakes to improve their hypocentre locations.

The feasibility to reduce the workload by applying the here developed automatic picker based on the rolling AIC, was tested on a subset of $\sim$200 events. These events had been accurately manually processed in order to obtain a more detailed overview of the aftershock distribution of one of the earlier and larger earthquakes ($M_w = 1.5$) which occurred during the stimulation. The scope of application required substantial adaptation of the algorithm's parameters as the magnitude ranges and the sensor network of the two scenarios substantially differ, i.e. approximately $1.0 \leq M_w \leq 4.5$ vs. $-1.0 \leq M_w \leq 1.9$ and $250 \cdot 100$ km^2 vs. $5 \cdot 5$ km^2 at the North Anatolian Fault Zone in the Sea of Marmara (in the years between 2006–2016) and during the hydraulic stimulation, respectively.

Figure A.1a shows the timing residuals between automatic (obtained with the here presented rolling AIC) and manual picks on $\sim$200 events of the afore mentioned main-shock after-shock sequence. The algorithm captures more

[1] A manuscript describing the real-time supervision of the hydraulic stimulation has been submitted to *Science*.

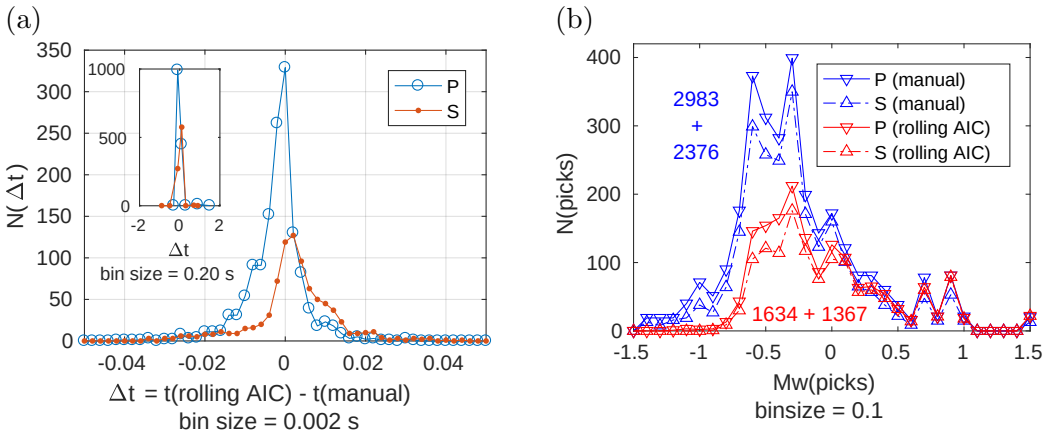

Figure A.1.: Picking residuals between automatic (rolling AIC) and manual P- and S-wave onsets. The inset shows the same distribution for a larger residual interval. Here only values larger than zero are shown. (b) Frequencies of automatic (rolling AIC) and manual P- and S-picks as functions of the corresponding earthquake magnitude. The integers in the colour of the corresponding picking algorithm indicate the total number P- and S-picks.

than half of the manual picks in total ($\sim$ 3000 out of $\sim$ 5300, Fig. A.1b) and almost all comparable automatic P- and S-picks are within 0.02 s of the corresponding manual pick. Most of the onsets not picked by the algorithm, belong to events with $M_w \leq 0.2$.

Application of the here developed automatic picker (rolling AIC) to 2710 events with M_w between -0.6 and 0.5 increased the number of P-Picks by $\sim$ 165 %, leaving $\sim$ 4 % from the original STA/LTA triggers unpicked (Fig. A.2a). 15 % out of all possible picks ($\sim$60.000) were picked by neither of the two algorithms. The P-picks from the rolling AIC-algorithm are sightly but systematically earlier than those from the STA/LTA trigger (Fig. A.2b. This is due to the causal averaging performed in the latter algorithm. S-picks could not be compared with each other, because the real-time STA/LTA-picker did not yield S-picks.

The automatic picker based on the rolling AIC reproduces more than one half of the manual picks with high accuracy. Compared to the STA/LTA trigger, it adds a significant number of further P-picks. The majority of onsets picked by both algorithms are within 0.06 s. This shows the versatility of the here developed and presented algorithm. Table A.1 compares the parameter sets applied to the two different datasets.

Table A.1.: Parameters for the rolling-AIC P- and S-picker in a local and regional application.

	hydaulic stimulation (local)	Sea of Marmara (regional)
preprocessing		
window around mean trigger [s]	[-3, 6]	[-40, 140]
P-pick 1		
bandpass 1 [Hz]	[20, 120]	[2, 12]
running kurtosis width [s]	0.2000	2
AIC win. width [s]	0.3000	8
AIC overlap around kurtosis max. [s]	0.1000	1
bandpass 2 [Hz]	[20, 180]	[1, 33]
P-pick 2		
min. err. bound around 1st pick [s]	0.0500	1
min. AIC win. width for 2nd pick [s]	0.3000	6
AIC overlap around 1st pick [s]	0.0100	0.2000
P-quality assessment		
min. SNR(amplitude)	10	3
$t(P1) < t_{min}$ is too early [s]	-2.25	-30
$t(P2) < t_{min}$ is too late [s]	6	100
min. vert. to horz. ampl. ratio around P-pick	3	2
win. to integrate energy	0.0500	4
min. ratio of signal to noise energy	10	5
bounds for temporal mean of energy distr.	[1.5, 5.5]	[25, 125]
max. temporal std. dev. of energy distr.	2	51
First motion		
noise win. [s]	[-0.50, -0.005]	[-1.00, -0.05]
signal win. [s]	[0.00, 0.200]	[0.00, 0.30]
min. SNR(std. dev.)	2	2
S-pick		
band pass 1 [Hz]	[25, 120]	[2, 12]
band pass 2 [Hz]	[20, 180]	[1, 16]
max. epicentral distance [km]	15	400
average v_p [km/s]	5.6	6
min. time gap to P-pick [s]	0.1	0.8
min. win. before CF max. [s]	0.2000	1
min. overlap after CF max [s]	0.1	1
noise win. [s]	[-0.50, -0.005]	[-1.00, -0.05]
signal win. [s]	[0.00, 0.200]	[0.00, 0.30]
acceptable ratio of P-coda level of horz. comp.s	3.5000	5
S-quality assessment		
min SNR(amplitude)	2	1.2
win. to integrate energy [s]	0.0500	4
min. ratio of signal to noise energy	5	5
bound for deviation in Wadati diagram [multiples of std. dev.]	3	1

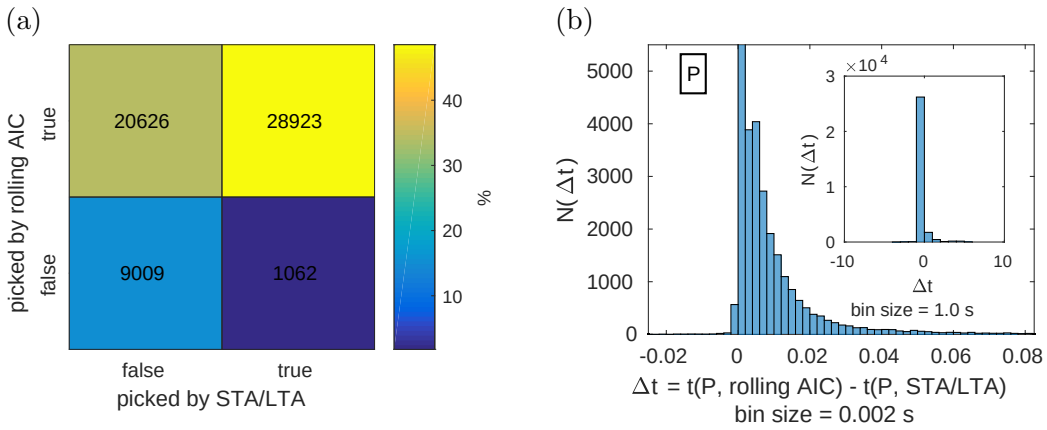

Figure A.2.: (a) Comparison of the picking rate of the two automatic picking algorithms, STA/LTA and rolling AIC, by event and sensor, i.e. out of $2710 \cdot 22 = 59.620$ possible picks in total. (b) Timing residual between the two picking algorithms. The inset shows the same distribution for a larger residual interval.

Bibliography

Abers, Geoffrey A. and John W. Gephart (2001). "Direct Inversion of Earthquake First Motions for Both the Stress Tensor and Focal Mechanisms and Application to Southern California". In: *Journal of Geophysical Research: Solid Earth* 106.B11, pp. 26523–26540. DOI: 10.1029/2001JB000437. URL: http://dx.doi.org/10.1029/2001JB000437.

Acarel, Diğdem, Fatih Bulut, Marco Bohnhoff, and Recai Kartal (2014). "Coseismic Velocity Change Associated with the 2011 Van Earthquake (M7.1): Crustal Response to a Major Event". In: *Geophysical Research Letters* 41.13. 2014GL060624, pp. 4519–4526. DOI: 10.1002/2014GL060624. URL: http://dx.doi.org/10.1002/2014GL060624.

Akaike, Hirotugu (1971). "Autoregressive Model Fitting for Control". In: *Annals of the Institute of Statistical Mathematics* 23.1, pp. 163–180. DOI: 10.1007/BF02479221. URL: http://dx.doi.org/10.1007/BF02479221.

Akaike, Hirotugu and Hirotugu Akaike (1974). "Markovian Representation of Stochastic Processes and Its Application to the Analysis of Autoregressive Moving Average Processes". In: *Annals of the Institute of Statistical Mathematics* 26.1, pp. 363–387. DOI: 10.1007/BF02479833. URL: http://dx.doi.org/10.1007/BF02479833.

Ambraseys, N. N. (1970). "Some Characteristic Features of the Anatolian Fault Zone". In: *Tectonophysics* 9.2–3, pp. 143–165. DOI: http://dx.doi.org/10.1016/0040-1951(70)90014-4. URL: http://www.sciencedirect.com/science/article/pii/0040195170900144.

Andrews, D. J. (1986). "Objective Determination of Source Parameters and Similarity of Earthquakes of Different Size". In: *Earthquake Source Mechanics*. American Geophysical Union, pp. 259–267. URL: http://dx.doi.org/10.1029/GM037p0259.

Ansal, A., A. Akinci, G. Cultrera, M. Erdik, V. Pessina, G. Tönük, and G. Ameri (2009). "Loss Estimation in Istanbul Based on Deterministic Earthquake Scenarios of the Marmara Sea Region (Turkey)". In: *Soil Dynamics and Earthquake Engineering* 29.4, pp. 699–709. DOI: https://doi.org/10.1016/j.soildyn.2008.07.006. URL: http://www.sciencedirect.com/science/article/pii/S0267726108001279.

Armijo, Rolando, Bertrand Meyer, Aurélia Hubert, and Aykut Barka (1999). "Westward Propagation of the North Anatolian Fault into the Northern Aegean: Timing and Kinematics". In: *Geology* 27.3, pp. 267–270.

Armijo, Rolando, Bertrand Meyer, Sébastien Navarro, Geoffrey King, and Aykut Barka (2002). "Asymmetric Slip Partitioning in the Sea of Marmara Pull-Apart: A Clue to Propagation Processes of the North Anatolian Fault?" In: *Terra Nova* 14.2, pp. 80–86. DOI: 10.1046/j.1365-3121.2002.00397.x. URL: http://dx.doi.org/10.1046/j.1365-3121.2002.00397.x.

Armijo, Rolando et al. (2005). "Submarine Fault Scarps in the Sea of Marmara Pull-Apart (North Anatolian Fault): Implications for Seismic Hazard in Istanbul". In: *Geochemistry, Geophysics, Geosystems* 6.6, n/a–n/a. DOI: 10.1029/2004GC000896. URL: http://dx.doi.org/10.1029/2004GC000896.

Aster, Richard C. and Jennifer Scott (1993). "Comprehensive Characterization of Waveform Similarity in Microearthquake Data Sets". In: *Bulletin of the Seismological Society of America* 83.4, p. 1307. URL: http://dx.doi.org/.

Barka, A. (1992). "The North Anatolian Fault Zone". In: *Annales Tectonicae*. Vol. 6, pp. 164–195.

Barka, A. et al. (2002). "The Surface Rupture and Slip Distribution of the 17 August 1999 İzmit Earthquake (M 7.4), North Anatolian Fault". In: *Bulletin of the Seismological Society of America* 92.1, p. 43. DOI: 10.1785/0120000841. URL: +%5C%0020http://dx.doi.org/10.1785/0120000841.

Bas, M. and M. Ö. Yăgci (2008). "Disaster Prevention Mitigation Studies for a Safer Urban Life Measures for Preventing Disaster of Istanbul Metropolitan Municipality". In: *Megacity Istanbul Megacity Project Reports, Municipality Disaster Management Center (AKOM), Istanbul, Turkey*. URL: http://www.cedim.de/download/Megacity_Istanbul_Final_Report2008.pdf.

Bécel, Anne, Mireille Laigle, Béatrice de Voogd, Alfred Hirn, Tuncay Taymaz, Audrey Galvé, Hideki Shimamura, Yoshio Murai, Jean-Claude Lépine, Martine Sapin, and Serdar Özalaybey (2009). "Moho, Crustal Architecture and Deep Deformation under the North Marmara Trough, from the SEISMARMARA Leg 1 Offshore–onshore Reflection–refraction Survey". In: *Tectonophysics* 467.1–4, pp. 1–21. DOI: 10.1016/j.tecto.2008.10.022. URL: http://www.sciencedirect.com/science/article/pii/S0040195108005192.

Beyreuther, Moritz and Joachim Wassermann (2008). "Continuous earthquake detection and classification using discrete Hidden Markov Models". In: *Geophysical Journal International* 175.3, pp. 1055–1066. DOI: 10.1111/j.1365-246X.2008.03921.x. URL: http://dx.doi.org/10.1111/j.1365-246X.2008.03921.x.

Bohnhoff, Marco, Stefan Baisch, and Hans-Peter Harjes (2004). "Fault Mechanisms of Induced Seismicity at the Superdeep German Continental Deep Drilling Program (KTB) Borehole and Their Relation to Fault Structure and Stress Field". In: *Journal of Geophysical Research: Solid Earth* 109.B2.

B02309, n/a–n/a. DOI: 10.1029/2003JB002528. URL: http://dx.doi.org/10.1029/2003JB002528.

Bohnhoff, Marco, Fatih Bulut, Georg Dresen, Peter E. Malin, Tuna Eken, and Mustafa Aktar (2013). "An Earthquake Gap South of Istanbul". In: *Nat Commun* 4. URL: http://dx.doi.org/10.1038/ncomms2999.

Bohnhoff, Marco, Georg Dresen, William L. Ellsworth, and Hisao Ito (2010). "Passive Seismic Monitoring of Natural and Induced Earthquakes: Case Studies, Future Directions and Socio-Economic Relevance". In: *New Frontiers in Integrated Solid Earth Sciences*. Ed. by Sierd Cloetingh, Jörg Negendank, and Springer. Dordrecht; New York: Springer, pp. 261–285. DOI: 10.1007/978-90-481-2737-5_7. URL: http://pubs.er.usgs.gov/publication/70158981.

Bohnhoff, Marco, Helmut Grosser, and Georg Dresen (2006). "Strain Partitioning and Stress Rotation at the North Anatolian Fault Zone from Aftershock Focal Mechanisms of the 1999 Izmit Mw= 7.4 Earthquake". In: *Geophysical Journal International* 166.1, pp. 373–385. DOI: 10.1111/j.1365-246X.2006.03027.x. URL: http://dx.doi.org/10.1111/j.1365-246X.2006.03027.x.

Bohnhoff, Marco, Hans-Peter Harjes, and Thomas Meier (2005). "Deformation and Stress Regimes in the Hellenic Subduction Zone from Focal Mechanisms". In: *Journal of Seismology* 9.3, pp. 341–366. DOI: 10.1007/s10950-005-8720-5. URL: https://doi.org/10.1007/s10950-005-8720-5.

Bohnhoff, Marco, Michèle Ickrath, and Georg Dresen (2016a). "Seismicity Distribution in Conjunction with Spatiotemporal Variations of Coseismic Slip and Postseismic Creep along the Combined 1999 Izmit-Düzce Rupture". In: *Tectonophysics* 686, pp. 132–145. DOI: 10.1016/j.tecto.2016.07.029. URL: http://www.sciencedirect.com/science/article/pii/S0040195116303122.

Bohnhoff, Marco, Patricia Martínez-Garzón, Fatih Bulut, Eva Stierle, and Yehuda Ben-Zion (2016b). "Maximum Earthquake Magnitudes along Different Sections of the North Anatolian Fault Zone". In: *Tectonophysics* 674, pp. 147–165. DOI: http://dx.doi.org/10.1016/j.tecto.2016.02.028. URL: http://www.sciencedirect.com/science/article/pii/S0040195116001256.

Bohnhoff, Marco, Christopher Wollin, Dorina Domigall, Ludger Küperkoch, Patricia Martínez-Garzón, Grzegorz Kwiatek, Georg Dresen, and Peter E. Malin (2017a). "Repeating Marmara Sea Earthquakes: Indication for Fault Creep". In: *Geophysical Journal International* 210.1, pp. 332–339. DOI: 10.1093/gji/ggx169. URL: http://dx.doi.org/10.1093/gji/ggx169.

Bohnhoff, Marco et al. (2017b). "GONAF – the Borehole Geophysical Observatory at the North Anatolian Fault in the Eastern Sea of Marmara". In: *Scientific Drilling* 22, pp. 19–28. DOI: 10.5194/sd-22-19-2017. URL: https://www.sci-dril.net/22/19/2017/.

Bott, Martin Harold Phillips (1959). "The Mechanics of Oblique Slip Faulting". In: *Geological Magazine* 96.2, pp. 109–117. URL: http://geolmag.geoscienceworld.org/content/96/2/109.

Brudy, M., M. D. Zoback, K. Fuchs, F. Rummel, and J. Baumgärtner (1997). "Estimation of the Complete Stress Tensor to 8 Km Depth in the KTB Scientific Drill Holes: Implications for Crustal Strength". In: *Journal of Geophysical Research: Solid Earth* 102.B8, pp. 18453–18475. DOI: 10.1029/96JB02942. URL: http://dx.doi.org/10.1029/96JB02942.

Bulut, Fatih and Mustafa Aktar (2007a). "Accurate Relocation of İzmit Earthquake (Mw = 7.4, 1999) Aftershocks in Çınarcık Basin Using Double Difference Method". In: *Geophysical Research Letters* 34.10. DOI: 10.1029/2007GL029611. URL: https://agupubs.onlinelibrary.wiley.com/doi/abs/10.1029/2007GL029611.

Bulut, Fatih, Marco Bohnhoff, Mustafa Aktar, and Georg Dresen (2007b). "Characterization of Aftershock-Fault Plane Orientations of the 1999 İzmit (Turkey) Earthquake Using High-Resolution Aftershock Locations". In: *Geophysical Research Letters* 34.20. DOI: 10.1029/2007GL031154. URL: http://dx.doi.org/10.1029/2007GL031154.

Bulut, Fatih, Marco Bohnhoff, Tuna Eken, Christoph Janssen, Tuğbay Kılıç, and Georg Dresen (2012). "The East Anatolian Fault Zone: Seismotectonic Setting and Spatiotemporal Characteristics of Seismicity Based on Precise Earthquake Locations". In: *Journal of Geophysical Research: Solid Earth* 117.B7, n/a–n/a. DOI: 10.1029/2011JB008966. URL: http://dx.doi.org/10.1029/2011JB008966.

Bulut, Fatih, Marco Bohnhoff, William L. Ellsworth, Mustafa Aktar, and Georg Dresen (2009). "Microseismicity at the North Anatolian Fault in the Sea of Marmara Offshore Istanbul, NW Turkey". In: *Journal of Geophysical Research: Solid Earth* 114.B9. DOI: 10.1029/2008JB006244. URL: http://dx.doi.org/10.1029/2008JB006244.

Bulut, Fatih, William L. Ellsworth, Marco Bohnhoff, Mustafa Aktar, and Georg Dresen (2011). "Spatiotemporal Earthquake Clusters along the North Anatolian Fault Zone Offshore Istanbul". In: *Bulletin of the Seismological Society of America* 101.4, pp. 1759–1768. DOI: 10.1785/0120100215. URL: http://www.bssaonline.org/content/101/4/1759.abstract.

Byerlee, J. (1978). "Friction of Rocks". In: *Pure and Applied Geophysics* 116.4, pp. 615–626. DOI: 10.1007/BF00876528. URL: https://doi.org/10.1007/BF00876528.

Cakir, Ziyadin, Semih Ergintav, Ahmet M. Akoğlu, Rahsan Çakmak, Orhan Tatar, and Mustapha Meghraoui (2014). "InSAR velocity field across the North Anatolian Fault (eastern Turkey): Implications for the loading and release of interseismic strain accumulation". In: *Journal of Geophysical Re-*

search: Solid Earth 119.10, pp. 7934–7943. DOI: 10.1002/2014JB011360. URL: https://doi.org/10.1002/2014JB011360.

Chaussard, E., R. Bürgmann, H. Fattahi, R. M. Nadeau, T. Taira, C. W. Johnson, and I. Johanson (2015). "Potential for Larger Earthquakes in the East San Francisco Bay Area Due to the Direct Connection between the Hayward and Calaveras Faults". In: *Geophysical Research Letters* 42.8, pp. 2734–2741. DOI: 10.1002/2015GL063575. URL: https://doi.org/10.1002/2015GL063575 (visited on 08/08/2018).

Cros, Estelle and Louis Geli L. (2013). *Caracterisation of Microseimicity in the Western Sea of Marmara: Implications in Terms of Seismic Monitoring*. Tech. rep. Ifremer. DOI: 10.13155/38916. URL: http://archimer.ifremer.fr/doc/00278/38916/.

DeVries, Phoebe M. R., Fernanda Viégas, Martin Wattenberg, and Brendan J. Meade (2018). "Deep learning of aftershock patterns following large earthquakes". In: *Nature* 560.7720, pp. 632–634. URL: https://doi.org/10.1038/s41586-018-0438-y.

Diehl, T., E. Kissling, S. Husen, and F. Aldersons (2009a). "Consistent Phase Picking for Regional Tomography Models: Application to the Greater Alpine Region". In: *Geophysical Journal International* 176.2, pp. 542–554. DOI: 10.1111/j.1365-246x.2008.03985.x. URL: http://dx.doi.org/10.1111/j.1365-246x.2008.03985.x.

Diehl, Tobias, N Deichmann, Edi Kissling, and S Husen (2009b). "Automatic S-Wave Picker for Local Earthquake Tomography". In: 99, pp. 1906–1920.

Eken, Tuna, Marco Bohnhoff, Fatih Bulut, Birsen Can, and Mustafa Aktar (2013). "Crustal Anisotropy in the Eastern Sea of Marmara Region in Northwestern Turkey". In: *Bulletin of the Seismological Society of America* 103.2A, pp. 911–924. DOI: 10.1785/0120120156. URL: http://bssa.geoscienceworld.org/content/103/2A/911.

Ergintav, S., R. E. Reilinger, R. Çakmak, M. Floyd, Z. Cakir, U. Doğan, R. W. King, S. McClusky, and H. Özener (2014). "Istanbul's Earthquake Hot Spots: Geodetic Constraints on Strain Accumulation along Faults in the Marmara Seismic Gap". In: *Geophysical Research Letters* 41.16. 2014GL060985, pp. 5783–5788. DOI: 10.1002/2014GL060985. URL: http://dx.doi.org/10.1002/2014GL060985.

Ester, Martin, Hans-Peter Kriegel, Jörg Sander, and Xiaowei Xu (1996). "A Density-based Algorithm for Discovering Clusters a Density-based Algorithm for Discovering Clusters in Large Spatial Databases with Noise". In: *Proceedings of the Second International Conference on Knowledge Discovery and Data Mining*. KDD'96. Portland, Oregon: AAAI Press, pp. 226–231. URL: http://dl.acm.org/citation.cfm?id=3001460.3001507.

Flerit, Frédéric, Rolando Armijo, Geoffrey King, and Bertrand Meyer (2004). "The Mechanical Interaction between the Propagating North Anatolian Fault and the Back-Arc Extension in the Aegean". In: *Earth and Planetary*

Science Letters 224.3, pp. 347–362. DOI: https://doi.org/10.1016/j.epsl.2004.05.028. URL: http://www.sciencedirect.com/science/article/pii/S0012821X04003486.

Geiger, Ludwig (1912). "Probability Method for the Determination of Earthquake Epicenters from the Arrival Time Only". In: *Bull. St. Louis Univ* 8.1, pp. 56–71.

Géli, L. et al. (2018). "Gas and Seismicity within the Istanbul Seismic Gap". In: *Scientific Reports* 8.1, p. 6819. DOI: 10.1038/s41598-018-23536-7. URL: https://doi.org/10.1038/s41598-018-23536-7.

Gentili, S. and A. Michelini (2006). "Automatic picking of P and S phases using a neural tree". In: *Journal of Seismology* 10.1, pp. 39–63. URL: https://doi.org/10.1007/s10950-006-2296-6.

Gholamrezaie, E., Scheck-Wenderoth M., and O. Heidbach (2018). "3D structural model of the Sea of Marmara". In: *Geophysical Research Abstracts*. Ed. by Vienna General Assembly European Geosciences Union. Vol. 20. EGU2018-10434-1. URL: http://gfzpublic.gfz-potsdam.de/pubman/item/escidoc:3107910.

Grigoli, Francesco, Simone Cesca, Ortensia Amoroso, Antonio Emolo, Aldo Zollo, and Torsten Dahm (2014). "Automated Seismic Event Location by Waveform Coherence Analysis". In: *Geophysical Journal International* 196.3, p. 1742. DOI: 10.1093/gji/ggt477. URL: +%5C%0020http://dx.doi.org/10.1093/gji/ggt477.

Hammer, Conny, Moritz Beyreuther, and Matthias Ohrnberger (2012). "A Seismic-Event Spotting System for Volcano Fast-Response Systems". In: *Bulletin of the Seismological Society of America* 102.3, pp. 948–960. DOI: 10.1785/0120110167. URL: http://dx.doi.org/10.1785/0120110167.

Han, J., J. Pei, and M. Kamber (2011). *Data Mining: Concepts and Techniques*. The Morgan Kaufmann Series in Data Management Systems. LCCB: 2011010635. Elsevier Science. URL: https://books.google.de/books?id=pQws07tdpjoC.

Hanks, Thomas C. and Hiroo Kanamori (1979). "A Moment Magnitude Scale". In: *Journal of Geophysical Research: Solid Earth* 84.B5, pp. 2348–2350. DOI: 10.1029/JB084iB05p02348. URL: http://dx.doi.org/10.1029/JB084iB05p02348.

Hardebeck, Jeanne L. and Egill Hauksson (1999). "Role of Fluids in Faulting Inferred from Stress Field Signatures". In: *Science* 285.5425, pp. 236–239. DOI: 10.1126/science.285.5425.236. URL: http://science.sciencemag.org/content/285/5425/236.

Hardebeck, Jeanne L. and Andrew J. Michael (2006). "Damped Regional-Scale Stress Inversions: Methodology and Examples for Southern California and the Coalinga Aftershock Sequence". In: *Journal of Geophysical Research: Solid Earth* 111.B11. B11310, n/a–n/a. DOI: 10.1029/2005JB004144. URL: http://dx.doi.org/10.1029/2005JB004144.

Hardebeck, Jeanne L. and Tomomi Okada (2018). "Temporal Stress Changes Caused by Earthquakes: A Review". In: *Journal of Geophysical Research: Solid Earth*. 2017JB014617, n/a–n/a. DOI: 10.1002/2017JB014617. URL: http://dx.doi.org/10.1002/2017JB014617.

Hardebeck, Jeanne L. and Peter M. Shearer (2002). "A New Method for Determining First-Motion Focal Mechanisms". In: *BULLETIN OF THE SEISMOLOGICAL SOCIETY OF AMERICA* 92.6, pp. 2264–2276. DOI: 10.1785/0120010200. URL: http://dx.doi.org/10.1785/0120010200.

Hébert, Hélène, Francois Schindelé, Yildiz Altinok, Bedri Alpar, and Cem Gazioglu (2005). "Tsunami Hazard in the Marmara Sea (Turkey): A Numerical Approach to Discuss Active Faulting and Impact on the Istanbul Coastal Areas". In: *Marine Geology* 215.1. Tsunamis in the Pacific, in the Atlantic and in Europe: relevant cases and hazard evaluation, pp. 23–43. DOI: https://doi.org/10.1016/j.margeo.2004.11.006. URL: http://www.sciencedirect.com/science/article/pii/S0025322704003238.

Hergert, Tobias and Oliver Heidbach (2010). "Slip-Rate Variability and Distributed Deformation in the Marmara Sea Fault System". In: *Nature Geoscience* 3.2, pp. 132–135.

Hergert, Tobias, Oliver Heidbach, Anne Bécel, and Mireille Laigle (2011). "Geomechanical Model of the Marmara Sea Region—I. 3-D Contemporary Kinematics". In: *Geophysical Journal International* 185.3, pp. 1073–1089. DOI: 10.1111/j.1365-246X.2011.04991.x. URL: http://dx.doi.org/10.1111/j.1365-246X.2011.04991.x.

Hickman, Stephen and Mark Zoback (2004). "Stress Orientations and Magnitudes in the SAFOD Pilot Hole". In: *Geophysical Research Letters* 31.15. L15S12, n/a–n/a. DOI: 10.1029/2004GL020043. URL: http://dx.doi.org/10.1029/2004GL020043.

Ickrath, Michèle, Marco Bohnhoff, Georg Dresen, Patricia Martınez-Garzón, Fatih Bulut, Grzegorz Kwiatek, and Oliver Germer (2015). "Detailed Analysis of Spatiotemporal Variations of the Stress Field Orientation along the Izmit-Düzce Rupture in NW Turkey from Inversion of First-Motion Polarity Data". In: *Geophysical Journal International* 202.3, pp. 2120–2120. DOI: 10.1093/gji/ggv273. URL: http://dx.doi.org/10.1093/gji/ggv273.

Janssen, C., M. Bohnhoff, Y. Vapnik, E. Görgün, F. Bulut, B. Plessen, D. Pohl, M. Aktar, A. I. Okay, and G. Dresen (2009). "Tectonic Evolution of the Ganos Segment of the North Anatolian Fault (NW Turkey)". In: *Journal of Structural Geology* 31.1, pp. 11–28. DOI: http://dx.doi.org/10.1016/j.jsg.2008.09.010. URL: http://www.sciencedirect.com/science/article/pii/S0191814108001636.

Jiang, Junle and Nadia Lapusta (2016). "Deeper penetration of large earthquakes on seismically quiescent faults". In: *Science* 352.6291, pp. 1293–1297. DOI: 10.1126/science.aaf1496. URL: http://science.sciencemag.org/content/352/6291/1293.

Jousset, Philippe, Agus Budi-Santoso, Arthur D. Jolly, Marie Boichu, Surono, S. Dwiyono, Sri Sumarti, Sri Hidayati, and Pierre Thierry (2013). "Signs of Magma Ascent in {LP} and {VLP} Seismic Events and Link to Degassing: An Example from the 2010 Explosive Eruption at Merapi Volcano, Indonesia". In: *Journal of Volcanology and Geothermal Research* 261. Merapi eruption, pp. 171–192. DOI: http://dx.doi.org/10.1016/j.jvolgeores.2013.03.014. URL: http://www.sciencedirect.com/science/article/pii/S0377027313000905.

Jousset, Philippe, Thomas Reinsch, Trond Ryberg, Hanna Blanck, Andy Clarke, Rufat Aghayev, Gylfi P. Hersir, Jan Henninges, Michael Weber, and Charlotte M. Krawczyk (2018). "Dynamic strain determination using fibre-optic cables allows imaging of seismological and structural features". In: *Nature Communications* 9.1, pp. 2509–. URL: https://doi.org/10.1038/s41467-018-04860-y.

Karabulut, Hayrullah, Marie-Paule Bouin, Michel Bouchon, Michel Dietrich, Cécile Cornou, and Mustafa Aktar (2002). "The Seismicity in the Eastern Marmara Sea after the 17 August 1999 İzmit Earthquake". In: *Bulletin of the Seismological Society of America* 92.1, pp. 387–393. DOI: 10.1785/0120000820. URL: http://bssa.geoscienceworld.org/content/92/1/387.

Karabulut, Hayrullah, J. Schmittbuhl, S. Özalaybey, O. Lengliné, A. Kömec-Mutlu, V. Durand, M. Bouchon, G. Daniel, and M. P. Bouin (2011). "Evolution of the Seismicity in the Eastern Marmara Sea a Decade before and after the 17 August 1999 Izmit Earthquake". In: *Tectonophysics* 510.1–2, pp. 17–27. DOI: http://dx.doi.org/10.1016/j.tecto.2011.07.009. URL: http://www.sciencedirect.com/science/article/pii/S0040195111002903.

Kennett, B. L. N., E. R. Engdahl, and R. Buland (1995). "Constraints on seismic velocities in the Earth from traveltimes". In: *Geophysical Journal International* 122.1, pp. 108–124. DOI: 10.1111/j.1365-246X.1995.tb03540.x. URL: http:https://doi.org/10.1111/j.1365-246X.1995.tb03540.x.

Ketin, Ihsan (1948). "Über Die Tektonisch-Mechanischen Folgerungen Aus Den Großen Anatolischen Erdbeben Des Letzten Dezenniums". In: *Geologische Rundschau* 36.1, pp. 77–83. DOI: 10.1007/BF01791916. URL: https://doi.org/10.1007/BF01791916.

Kinscher, J., F. Krüger, H. Woith, B.G. Lühr, E. Hintersberger, T.S. Irmak, and S. Baris (2013). "Seismotectonics of the Armutlu Peninsula (Marmara Sea, NW Turkey) from Geological Field Observation and Regional Moment Tensor Inversion". In: *Tectonophysics* 608, pp. 980–995. DOI: 10.1016/j.tecto.2013.07.016. URL: http://www.sciencedirect.com/science/article/pii/S0040195113004575.

Kiratzi, Anastasia A. (2002). "Stress Tensor Inversions along the Westernmost North Anatolian Fault Zone and Its Continuation into the North Aegean Sea". In: *Geophysical Journal International* 151.2, pp. 360–376. DOI: 10.1046/j.1365-246X.2002.01753.x. URL: http://dx.doi.org/10.1046/j.1365-246X.2002.01753.x.

Klein, E., Z. Duputel, F. Masson, H. Yavasoglu, and P. Agram (2017). "Aseismic Slip and Seismogenic Coupling in the Marmara Sea: What Can We Learn from Onland Geodesy?" In: *Geophysical Research Letters* 44.7. 2017GL072777, pp. 3100–3108. DOI: 10.1002/2017GL072777. URL: http://dx.doi.org/10.1002/2017GL072777.

Kleist, Heinrich von (1807). *The Earthquake in Chili*. Ed. by David Luke and Nigel Reeves. Vol. "Marquise of O - and Other Stories". Penguin Classics 1978.

Küperkoch, L. (2011). "Automated Recognition, Phase Arrival Time Estimation, and Location of Local and Regional Earthquakes". dissertation. Ruhr-Universität Bochum. URL: http://www-brs.ub.ruhr-uni-bochum.de/netahtml/HSS/Diss/KueperkochLudger/diss.pdf.

Küperkoch, L., T. Meier, A. Brüstle, J. Lee, W. Friederich, and EGELADOS Working Group (2012). "Automated Determination of S-Phase Arrival Times Using Autoregressive Prediction: Application to Local and Regional Distances". In: *Geophysical Journal International* 188.2, pp. 687–702. DOI: 10.1111/j.1365-246x.2011.05292.x. URL: http://dx.doi.org/10.1111/j.1365-246x.2011.05292.x.

Küperkoch, L., T. Meier, J. Lee, W. Friederich, and EGELADOS Working Group (2010). "Automated Determination of P-Phase Arrival Times at Regional and Local Distances Using Higher Order Statistics". In: *Geophysical Journal International* 181.2, pp. 1159–1170. DOI: 10.1111/j.1365-246X.2010.04570.x. URL: http://dx.doi.org/10.1111/j.1365-246X.2010.04570.x.

Latcharote, Panon, Anawat Suppasri, Fumihiko Imamura, Betul Aytore, and Ahmet Cevdet Yalciner (2016). "Possible Worst-Case Tsunami Scenarios around the Marmara Sea from Combined Earthquake and Landslide Sources". In: *Pure and Applied Geophysics* 173.12, pp. 3823–3846. DOI: 10.1007/s00024-016-1411-z. URL: https://doi.org/10.1007/s00024-016-1411-z.

Le Pichon, X, Ni Chamot-Rooke, C Rangin, and AMC Sengör (2003). "The North Anatolian Fault in the Sea of Marmara". In: *Journal of Geophysical Research: Solid Earth* 108.B4.

Le Pichon, X, Caner İmren, Claude Rangin, A.M.Celâl Sengör, and Muzaffer Siyako (2014). "The South Marmara Fault". English. In: *International Journal of Earth Sciences* 103.1, pp. 219–231. DOI: 10.1007/s00531-013-0950-0. URL: http://dx.doi.org/10.1007/s00531-013-0950-0.

Le Pichon, X, AMC Sengör, E Demirbăg, C Rangin, C Imren, R Armijo, N Görür, N Căgatay, B Mercier De Lepinay, B Meyer, R. Saatcılare, and B. Tok (2001). "The Active Main Marmara Fault". In: *Earth and Planetary Science Letters* 192.4, pp. 595–616. DOI: http://dx.doi.org/10.1016/S0012-821X(01)00449-6. URL: http://www.sciencedirect.com/science/article/pii/S0012821X01004496.

Le Pichon, X, AMC Şengör, and T Taymaz (1999). "The Marmara Fault and the Future Istanbul Earthquake". In: ed. by M. Karaca and D.N. Ural. Istanbul Technical University, Turkey, pp. 41–54.

Le Pichon, X, A.M.Celâl Şengör, Julia Kende, Caner İmren, Pierre Henry, Céline Grall, and Hayrullah Karabulut (2015). "Propagation of a Strike Slip Plate Boundary within an Extensional Environment: The Westward Propagation of the North Anatolian Fault". In: *Canadian Journal of Earth Sciences* ja, null–null. DOI: 10.1139/cjes-2015-0129. URL: http://dx.doi.org/10.1139/cjes-2015-0129.

Leonard, M. and B. L. N. Kennett (1999). "Multi-Component Autoregressive Techniques for the Analysis of Seismograms". In: *Physics of the Earth and Planetary Interiors* 113.1–4, pp. 247–263. DOI: http://dx.doi.org/10.1016/S0031-9201(99)00054-0. URL: http://www.sciencedirect.com/science/article/pii/S0031920199000540.

Lindsey, Nathaniel J., Eileen R. Martin, Douglas S. Dreger, Barry Freifeld, Stephen Cole, Stephanie R. James, Biondo L. Biondi, and Jonathan B. Ajo-Franklin (2017). "Fiber-Optic Network Observations of Earthquake Wavefields". In: *Geophysical Research Letters* 44.23, pp. 11, 792–11, 799. DOI: 10.1002/2017GL075722. URL: http://dx.doi.org/10.1002/2017GL075722.

Lisowski, M., J. C. Savage, and W. H. Prescott (1991). "The velocity field along the San Andreas Fault in central and southern California". In: *J. Geophys. Res.* 96.B5, pp. 8369–8389. DOI: 10.1029/91JB00199. URL: https://doi.org/10.1029/91JB00199.

Lund, Björn and John Townend (2007). "Calculating Horizontal Stress Orientations with Full or Partial Knowledge of the Tectonic Stress Tensor". In: *Geophysical Journal International* 170.3, pp. 1328–1335. DOI: 10.1111/j.1365-246X.2007.03468.x. URL: http://dx.doi.org/10.1111/j.1365-246X.2007.03468.x.

Maeda, Naoki (1985). "A Method for Reading and Checking Phase Time in Auto-Processing System of Seismic Wave Data". In: *Zisin (Journal of the Seismological Society of Japan. 2nd ser.)* 38.3, pp. 365–379.

Marra, Giuseppe, Cecilia Clivati, Richard Luckett, Anna Tampellini, Jochen Kronjäger, Louise Wright, Alberto Mura, Filippo Levi, Stephen Robinson, André Xuereb, Brian Baptie, and Davide Calonico (2018). "Ultrastable laser interferometry for earthquake detection with terrestrial and submarine cables". In: *Science* 361.6401, pp. 486–490. DOI: 10.1126/science.

aat4458. URL: http://science.sciencemag.org/content/361/6401/486.

Martínez-Garzón, Patricia, Yehuda Ben-Zion, Niloufar Abolfathian, Grzegorz Kwiatek, and Marco Bohnhoff (2016a). "A Refined Methodology for Stress Inversions of Earthquake Focal Mechanisms: Refined Stress Inversion Methodology". In: *Journal of Geophysical Research: Solid Earth*.

Martínez-Garzón, Patricia, Marco Bohnhoff, Grzegorz Kwiatek, and Georg Dresen (2013). "Stress Tensor Changes Related to Fluid Injection at The Geysers Geothermal Field, California". In: *Geophysical Research Letters* 40.11, pp. 2596–2601. DOI: 10.1002/grl.50438. URL: http://dx.doi.org/10.1002/grl.50438.

Martínez-Garzón, Patricia, Václav Vavryčuk, Grzegorz Kwiatek, and Marco Bohnhoff (2016b). "Sensitivity of Stress Inversion of Focal Mechanisms to Pore Pressure Changes". In: *Geophysical Research Letters* 43.16. 2016GL070145, pp. 8441–8450. DOI: 10.1002/2016GL070145. URL: http://dx.doi.org/10.1002/2016GL070145.

McClusky, S. et al. (2000). "Global Positioning System Constraints on Plate Kinematics and Dynamics in the Eastern Mediterranean and Caucasus". In: *Journal of Geophysical Research: Solid Earth* 105.B3, pp. 5695–5719. DOI: 10.1029/1999JB900351. URL: http://dx.doi.org/10.1029/1999JB900351.

McKenzie, Dan P. (1969). "The Relation between Fault Plane Solutions for Earthquakes and the Directions of the Principal Stresses". In: *Bulletin of the Seismological Society of America* 59.2, pp. 591–601. URL: http://bssa.geoscienceworld.org/content/59/2/591.

Motagh, Mahdi, Jörn Hoffmann, Bert Kampes, Marzieh Baes, and Jochen Zschau (2007). "Strain Accumulation across the Gazikoy–Saros Segment of the North Anatolian Fault Inferred from Persistent Scatterer Interferometry and GPS Measurements". In: *Earth and Planetary Science Letters* 255.3, pp. 432–444. DOI: http://dx.doi.org/10.1016/j.epsl.2007.01.003. URL: http://www.sciencedirect.com/science/article/pii/S0012821X07000040.

Müller, Gerhard and Michael Weber (2007). *Theory of elastic waves*. Scientific technical report / GeoForschungsZentrum Potsdam. MAB0014.001: STR 07/03. Potsdam: GeoForschungsZentrum. URL: urn:nbn:de:kobv:b103-07037.

Murru, M., A. Akinci, G. Falcone, S. Pucci, R. Console, and T. Parsons (2016). "M≥7 Earthquake Rupture Forecast and Time-Dependent Probability for the Sea of Marmara Region, Turkey". In: *Journal of Geophysical Research: Solid Earth* 121.4. 2015JB012595, pp. 2679–2707. DOI: 10.1002/2015JB012595. URL: http://dx.doi.org/10.1002/2015JB012595.

Nadeau, R. M., W. Foxall, and T. V. McEvilly (1995). "Clustering and Periodic Recurrence of Microearthquakes on the San Andreas Fault at Parkfield,

California". In: *Science* 267.5197, pp. 503–507. DOI: 10.1126/science.267.5197.503. URL: http://science.sciencemag.org/content/267/5197/503.

Nadeau, R. M. and T. V. McEvilly (2004). "Periodic pulsing of characteristic microearthquakes on the San Andreas Fault". In: *Science* 303.5655, pp. 220–222. DOI: 10.1126/science.1090353. URL: http://science.sciencemag.org/content/303/5655/220.

Najdahmadi, B., M. Bohnhoff, and Y. Ben-Zion (2016). "Bimaterial Interfaces at the Karadere Segment of the North Anatolian Fault, Northwestern Turkey". In: *Journal of Geophysical Research: Solid Earth* 121.2. 2015JB012601, pp. 931–950. DOI: 10.1002/2015JB012601. URL: http://dx.doi.org/10.1002/2015JB012601.

Oglesby, David D., P. Martin Mai, Kuvvet Atakan, and Stefano Pucci (2008). "Dynamic models of earthquakes on the North Anatolian fault zone under the Sea of Marmara: Effect of hypocenter location". In: *Geophys. Res. Lett.* 35.18. DOI: 10.1029/2008GL035037. URL: https://doi.org/10.1029/2008GL035037.

Örgülü, G. (2011). "Seismicity and Source Parameters for Small-Scale Earthquakes along the Splays of the North Anatolian Fault (NAF) in the Marmara Sea". In: *Geophysical Journal International* 184.1, pp. 385–404. DOI: 10.1111/j.1365-246X.2010.04844.x. URL: http://gji.oxfordjournals.org/content/184/1/385.abstract.

Öztürk, Yasemin Korkusuz, Nurcan Meral Özal, and Ali Děger Özbakir (2015). "States of Local Stresses in the Sea of Marmara through the Analysis of Large Numbers of Small Earthquakes". In: *Tectonophysics* 665, pp. 37–57. DOI: http://dx.doi.org/10.1016/j.tecto.2015.09.027. URL: http://www.sciencedirect.com/science/article/pii/S0040195115005284.

Page, R. (1968). "Aftershocks and Microaftershocks of the Great Alaska Earthquake of 1964". In: *Bull. Seismol. Soc. Am.* 58.3. cited By 168, pp. 1131–1168.

Parsons, Tom (2004). "Recalculated Probability of M7 Earthquakes beneath the Sea of Marmara, Turkey". In: *Journal of Geophysical Research: Solid Earth* 109.B5. B05304. DOI: 10.1029/2003JB002667. URL: http://dx.doi.org/10.1029/2003JB002667.

Perol, Thibaut, Michaäl Gharbi, and Marine Denolle (2018). "Convolutional neural network for earthquake detection and location". In: *Science Advances* 4.2. URL: http://advances.sciencemag.org/content/4/2/e1700578.abstract.

Pinar, Ali, Yoshimori Honkura, and Keiko Kuge (2001). "Seismic Activity Triggered by the 1999 Izmit Earthquake and Its Implications for the Assessment of Future Seismic Risk". In: *Geophysical Journal International* 146.1, F1–F7. DOI: 10.1046/j.0956-540x.2001.01476.x. URL: http://dx.doi.org/10.1046/j.0956-540x.2001.01476.x.

Pinar, Ali, Keiko Kuge, and Yoshimori Honkura (2003). "Moment Tensor Inversion of Recent Small to Moderate Sized Earthquakes: Implications for Seismic Hazard and Active Tectonics beneath the Sea of Marmara". In: *Geophysical Journal International* 153.1, pp. 133–145. DOI: 10.1046/j.1365-246X.2003.01897.x. URL: +%5C%0020http://dx.doi.org/10.1046/j.1365-246X.2003.01897.x.

Poupinet, G., W. L. Ellsworth, and J. Frechet (1984). "Monitoring Velocity Variations in the Crust Using Earthquake Doublets: An Application to the Calaveras Fault, California". In: *Journal of Geophysical Research: Solid Earth* 89.B7, pp. 5719–5731. DOI: 10.1029/JB089iB07p05719. URL: https://agupubs.onlinelibrary.wiley.com/doi/abs/10.1029/JB089iB07p05719.

Prevedel, Bernhard, Fatih Bulut, Marco Bohnhoff, Christina Raub, Recai F. Kartal, Fatih Alver, and Peter E. Malin (2015). "Downhole Geophysical Observatories: Best Installation Practices and a Case History from Turkey". In: *International Journal of Earth Sciences* 104.6, pp. 1537–1547. DOI: 10.1007/s00531-015-1147-5. URL: https://doi.org/10.1007/s00531-015-1147-5.

Raub, Christina, Marco Bohnhoff, Bojana Petrovic, Stefano Parolai, Peter Malin, Kenan Yanik, Recai Feyiz Kartal, and Tuğbay Kiliç (2016). "Seismic-Wave Propagation in Shallow Layers at the GONAF-Tuzla Site, Istanbul, Turkey". In: *Bulletin of the Seismological Society of America*. DOI: 10.1785/0120150216. URL: http://bssa.geoscienceworld.org/content/early/2016/05/20/0120150216.

Raub, Christina, Patricia Martınez-Garzón, Grzegorz Kwiatek, Marco Bohnhoff, and Georg Dresen (2017). "Variations of Seismic B-Value at Different Stages of the Seismic Cycle along the North Anatolian Fault Zone in Northwestern Turkey". In: *Tectonophysics* 712, pp. 232–248. DOI: http://dx.doi.org/10.1016/j.tecto.2017.05.028. URL: http://www.sciencedirect.com/science/article/pii/S0040195117302251.

Reilinger, Robert et al. (2006). "GPS Constraints on Continental Deformation in the Africa-Arabia-Eurasia Continental Collision Zone and Implications for the Dynamics of Plate Interactions". In: *Journal of Geophysical Research: Solid Earth* 111.B5. B05411, n/a–n/a. DOI: 10.1029/2005JB004051. URL: http://dx.doi.org/10.1029/2005JB004051.

Robinson, Russell and Peter J. McGinty (2000). "The Enigma of the Arthur's Pass, New Zealand, Earthquake: 2. The Aftershock Distribution and Its Relation to Regional and Induced Stress Fields". In: *Journal of Geophysical Research: Solid Earth* 105.B7, pp. 16139–16150. DOI: 10.1029/2000JB900012. URL: http://dx.doi.org/10.1029/2000JB900012.

Ross, Z. E. and Y. Ben-Zion (2014). "Automatic Picking of Direct P, S Seismic Phases and Fault Zone Head Waves". In: *Geophysical Journal International*

199.1, pp. 368–381. DOI: 10.1093/gji/ggu267. URL: +%5C%0020http://dx.doi.org/10.1093/gji/ggu267.

Ross, Zachary E., Egill Hauksson, and Yehuda Ben-Zion (2017). "Abundant off-fault seismicity and orthogonal structures in the San Jacinto fault zone". In: *Science Advances* 3.3. DOI: 10.1126/sciadv.1601946. URL: http://advances.sciencemag.org/content/3/3/e1601946.

Rubinstein, J.L. and W.L. Ellsworth (2010). "Precise Estimation of Repeating Earthquake Moment: Example from Parkfield, California". In: *Bulletin of the Seismological Society of America* 100.5 A, pp. 1952–1961. DOI: 10.1785/0120100007. URL: http://pubs.er.usgs.gov/publication/70037629.

Sakic, P., H. Piété, V. Ballu, J.-Y. Royer, H. Kopp, D. Lange, F. Petersen, M. S. Özeren, S. Ergintav, L. Geli, P. Henry, and A. Deschamps (2016). "No Significant Steady State Surface Creep along the North Anatolian Fault Offshore Istanbul: Results of 6 Months of Seafloor Acoustic Ranging". In: *Geophysical Research Letters* 43.13. 2016GL069600, pp. 6817–6825. DOI: 10.1002/2016GL069600. URL: http://dx.doi.org/10.1002/2016GL069600.

Sato, Toshinori, Junzo Kasahara, Tuncay Taymaz, Masakazu Ito, Aya Kamimura, Tadaaki Hayakawa, and Onur Tan (2004). "A Study of Microearthquake Seismicity and Focal Mechanisms within the Sea of Marmara (NW Turkey) Using Ocean Bottom Seismometers (OBSs)". In: *Tectonophysics* 391.1. Active Faulting and Crustal Deformation in the Eastern Mediterranean Region, pp. 303–314. DOI: https://doi.org/10.1016/j.tecto.2004.07.018. URL: http://www.sciencedirect.com/science/article/pii/S0040195104002379.

Schmittbuhl, J., H. Karabulut, O. Lengliné, and M. Bouchon (2015). "Seismicity Distribution and Locking Depth along the Main Marmara Fault, Turkey". In: *Geochemistry, Geophysics, Geosystems* 17.3, pp. 954–965. DOI: 10.1002/2015GC006120. URL: http://dx.doi.org/10.1002/2015GC006120.

Schmittbuhl, J., H. Karabulut, O. Lengliné, and M. Bouchon (2016). "Long-Lasting Seismic Repeaters in the Central Basin of the Main Marmara Fault". In: *Geophysical Research Letters* 43.18. 2016GL070505, pp. 9527–9534. DOI: 10.1002/2016GL070505. URL: http://dx.doi.org/10.1002/2016GL070505.

Schumann, Coco (1997). *Der Ghetto-Swinger*. Deutscher Taschenbuchverlag. Chap. 12.

Schweitzer, Johannes (2001). "HYPOSAT — An Enhanced Routine to Locate Seismic Events". English. In: *Monitoring the Comprehensive Nuclear-Test-Ban Treaty: Sourse Location*. Ed. by Frode Ringdal and BrianL.N. Kennett. Pageoph Topical Volumes. Birkhäuser Basel, pp. 277–289. URL: http://dx.doi.org/10.1007/978-3-0348-8250-7_17.

Şengör, A.M. Celâl, Naci Görür, and Fuat Sarŏglu (1985). "Strike-Slip Faulting and Related Basin Formation in Zones of Tectonic Escape: Turkey as a Case Study". In: *Society of Economic Paleontologists and Mineralogists*.

Şengör, A.M. Celâl, Céline Grall, Caner İmren, Xavier Le Pichon, Naci Görür, Pierre Henry, Hayrullah Karabulut, and Muzaffer Siyako (2014). "The Geometry of the North Anatolian Transform Fault in the Sea of Marmara and Its Temporal Evolution: Implications for the Development of Intracontinental Transform Faults". In: *Can. J. Earth Sci.* 51.3, pp. 222–242. DOI: 10.1139/cjes-2013-0160. URL: http://dx.doi.org/10.1139/cjes-2013-0160.

Şengör, A.M. Celâl, Okan Tüysüz, Caner İmren, Mehmet Sakınç, Haluk Eyidoğan, Naci Görür, Xavier Le Pichon, and Claude Rangin (2005). "The North Anatolian Fault: A New Look". In: *Annual Review of Earth and Planetary Sciences* 33.1, pp. 37–112. DOI: 10.1146/annurev.earth.32.101802.120415. URL: https://doi.org/10.1146/annurev.earth.32.101802.120415.

Shearer, Peter M. (1999). *Introduction to Seismology*. Cambridge: Cambridge University Press. URL: http://www.worldcat.org/isbn/0521669537.

Sippl, C. et al. (2013). "Geometry of the Pamir-Hindu Kush Intermediate-Depth Earthquake Zone from Local Seismic Data". In: *Journal of Geophysical Research: Solid Earth* 118.4, pp. 1438–1457. DOI: 10.1002/jgrb.50128. URL: http://dx.doi.org/10.1002/jgrb.50128.

Sleeman, Reinoud and Torild van Eck (1999). "Robust Automatic P-Phase Picking: An on-Line Implementation in the Analysis of Broadband Seismogram Recordings". In: *Physics of the Earth and Planetary Interiors* 113.1–4, pp. 265–275. DOI: http://dx.doi.org/10.1016/S0031-9201(99)00007-2. URL: http://www.sciencedirect.com/science/article/pii/S0031920199000072.

Snoke, J. A. (1987). "Stable Determination of (Brune) Stress Drops". In: *Bulletin of the Seismological Society of America* 77.2, pp. 530–538. URL: http://www.bssaonline.org/content/77/2/530.abstract.

Spagnuolo, E., A. Akinci, A. Herrero, and S. Pucci (2016). "Implementing the Effect of the Rupture Directivity on PSHA for the City of Istanbul, TurkeyImplementing the Effect of the Rupture Directivity on PSHA for the City of Istanbul, Turkey". In: *Bulletin of the Seismological Society of America* 106.6, p. 2599. DOI: 10.1785/0120160020. URL: http://dx.doi.org/10.1785/0120160020.

Storchak, D. A., J. Schweitzer, and P. Bormann (2003). "The IASPEI Standard Seismic Phase List". In: *Seismological Research Letters* 74.6, pp. 761–772. DOI: 10.1785/gssrl.74.6.761. URL: http://dx.doi.org/10.1785/gssrl.74.6.761.

Tary, J. B., L. Géli, P. Henry, B. Natalin, L. Gasperini, M. Çomoğlu, N. Çağatay, and T. Bardainne (2011). "Sea-Bottom Observations from the

Western Escarpment of the Sea of Marmara". In: *Bulletin of the Seismological Society of America* 101.2, p. 775. DOI: 10.1785/0120100014. URL: +%5C%0020http://dx.doi.org/10.1785/0120100014.

TeleGeography (2018). *The 2018 Submarine Cable Map*. URL: https://www.submarinecablemap.com/#/landing-point/istanbul-turkey.

Tibi, R., G. Bock, Y. Xia, M. Baumbach, H. Grosser, C. Milkereit, S. Karakisa, S. Zünbül, R. Kind, and J. Zschau (2001). "Rupture Processes of the 1999 August 17 Izmit and November 12 Düzce (Turkey) Earthquakes". In: *Geophysical Journal International* 144.2, F1–F7. DOI: 10.1046/j.1365-246x.2001.00360.x. URL: http://dx.doi.org/10.1046/j.1365-246x.2001.00360.x.

Townend, John and Mark D. Zoback (2001). "Implications of Earthquake Focal Mechanisms for the Frictional Strength of the San Andreas Fault System". In: *Geological Society, London, Special Publications* 186.1, pp. 13–21. DOI: 10.1144/GSL.SP.2001.186.01.02. URL: http://sp.lyellcollection.org/content/186/1/13.

Vavryčuk, Václav (2011). "Principal Earthquakes: Theory and Observations from the 2008 West Bohemia Swarm". In: *Earth and Planetary Science Letters* 305.3, pp. 290–296. DOI: https://doi.org/10.1016/j.epsl.2011.03.002. URL: http://www.sciencedirect.com/science/article/pii/S0012821X11001373.

Vavryčuk, Václav (2014). "Iterative Joint Inversion for Stress and Fault Orientations from Focal Mechanisms". In: *Geophysical Journal International* 199.1, pp. 69–77. DOI: 10.1093/gji/ggu224. URL: http://dx.doi.org/10.1093/gji/ggu224.

Vavryčuk, Václav (2015). "Earthquake Mechanisms and Stress Field". In: *Encyclopedia of Earthquake Engineering*. Ed. by Michael Beer, Ioannis A. Kougioumtzoglou, Edoardo Patelli, and Siu-Kui Au. Berlin, Heidelberg: Springer Berlin Heidelberg, pp. 728–746. URL: https://doi.org/10.1007/978-3-642-36197-5_295-1.

Vavryčuk, Václav and Petra Adamová (2018). "Detection of stress anomaly produced by interaction of compressive fault steps in the West Bohemia swarm region, Czech Republic". In: *Tectonics*. accepted.

Vidale, J. E. (1986). "Complex Polarization Analysis of Particle Motion". In: *Bulletin of the Seismological Society of America* 76.5, pp. 1393–1405. URL: http://dx.doi.org/.

Vidale, J. E., W. L. Ellsworth, A. Cole, and C. Marone (1994). "Variations in Rupture Process with Recurrence Interval in a Repeated Small Earthquake". In: *Nature* 368, p. 624. URL: http://dx.doi.org/10.1038/368624a0.

Waldhauser, Felix and William L. Ellsworth (2000). "A Double-Difference Earthquake Location Algorithm: Method and Application to the Northern Hayward Fault, California". In: *Bulletin of the Seismological Society*

of America 90.6, pp. 1353–1368. DOI: 10.1785/0120000006. URL: http://bssa.geoscienceworld.org/content/90/6/1353.

Waldhauser, Felix and William L. Ellsworth (2002). "Fault Structure and Mechanics of the Hayward Fault, California, from Double-Difference Earthquake Locations". In: *Journal of Geophysical Research: Solid Earth* 107.B3, ESE 3–1–ESE 3–15. DOI: 10.1029/2000JB000084. URL: http://dx.doi.org/10.1029/2000JB000084.

Wallace, Robert E. (1951). "Geometry of Shearing Stress and Relation to Faulting". In: *The Journal of Geology* 59.2, pp. 118–130. DOI: 10.1086/625831. URL: https://doi.org/10.1086/625831.

Wessel, Paul, Walter H. F. Smith, Remko Scharroo, Joaquim Luis, and Florian Wobbe (2013). "Generic Mapping Tools: Improved Version Released". In: *Eos, Transactions American Geophysical Union* 94.45, pp. 409–410. DOI: 10.1002/2013EO450001. URL: http://dx.doi.org/10.1002/2013EO450001.

Wiemer, Stefan and Max Wyss (2000). "Minimum Magnitude of Completeness in Earthquake Catalogs: Examples from Alaska, the Western United States, and Japan". In: *Bulletin of the Seismological Society of America* 90.4, p. 859. DOI: 10.1785/0119990114. URL: http://dx.doi.org/10.1785/0119990114.

Wollin, Christopher, Marco Bohnhoff, Patricia Martínez-Garzón, Ludger Küperkoch, and Christina Raub (2018a). "A Unified Earthquake Catalogue for the Sea of Marmara Region, Turkey, Based on Automatized Phase Picking and Travel-Time Inversion: Seismotectonic Implications". In: *Tectonophysics*. DOI: https://doi.org/10.1016/j.tecto.2018.05.020. URL: http://www.sciencedirect.com/science/article/pii/S004019511830204X.

Wollin, Christopher, Marco Bohnhoff, Václav Vavryčuk, and Patricia Martínez-Garzón (2018b). "Stress Inversion of Regional Seismicity in the Sea of Marmara Region, Turkey". In: *Pure and Applied Geophysics*. DOI: 10.1007/s00024-018-1971-1. URL: https://doi.org/10.1007/s00024-018-1971-1.

Yalçıner, Ahmet Cevdet, Bedri Alpar, Yıldız Altınok, İlknur Özbay, and Fumihiko Imamura (2002). "Tsunamis in the Sea of Marmara: Historical Documents for the Past, Models for the Future". In: *Marine Geology* 190.1, pp. 445–463. DOI: https://doi.org/10.1016/S0025-3227(02)00358-4. URL: http://www.sciencedirect.com/science/article/pii/S0025322702003584.

Yamamoto, R., M. Kido, Y. Ohta, N. Takahashi, Y. Yamamoto, D. Kalafat, A. Pinar, H. Ozener, M. S. Ozeren, and K. Yoshiyuki (2016). "Estimating Slip Deficit of the North Anatolian Fault beneath the Sea of Marmara, Turkey, Using on- and off-Shore Geodetic Data". In: *AGU Fall Meeting Abstracts*.

Yamamoto, Y., N. Takahashi, A. Pinar, D. Kalafat, S. Citak, M. Comoglu, R. Polat, and Y. Kaneda (2017). "Geometry and Segmentation of the North Anatolian Fault beneath the Marmara Sea, Turkey, Deduced from Long-Term Ocean Bottom Seismographic Observations". In: *Journal of Geophysical Research: Solid Earth*. 2016JB013608. DOI: 10.1002/2016JB013608. URL: http://dx.doi.org/10.1002/2016JB013608.

Yamamoto, Yojiro, Narumi Takahashi, Seckin Citak, Dǒgan Kalafat, Ali Pinar, Cemil Gurbuz, and Yoshiyuki Kaneda (2015). "Offshore Seismicity in the Western Marmara Sea, Turkey, Revealed by Ocean Bottom Observation". In: *Earth, Planets and Space* 67.1, p. 147. DOI: 10.1186/s40623-015-0325-9. URL: http://dx.doi.org/10.1186/s40623-015-0325-9.

Zhang, Haijiang, Clifford Thurber, and Charlotte Rowe (2003). "Automatic P-Wave Arrival Detection and Picking with Multiscale Wavelet Analysis for Single-Component Recordings". In: *Bulletin of the Seismological Society of America* 93.5, pp. 1904–1912. DOI: 10.1785/0120020241. URL: http://www.bssaonline.org/content/93/5/1904.abstract.

Zoback, Mark D. (2007). *Reservoir Geomechanics*. Cambridge University Press.

Zoback, Mary Lou (1992). "First- and Second-Order Patterns of Stress in the Lithosphere: The World Stress Map Project". In: *Journal of Geophysical Research: Solid Earth* 97.B8, pp. 11703–11728. DOI: 10.1029/92JB00132. URL: http://dx.doi.org/10.1029/92JB00132.

List of Figures

List of Tables

Acknowledgements

First of all, I thank my supervisor Prof. Marco Bohnhoff for initially taking me on board and thus providing me with the opportunity to work as a researcher in an unique environment. I also thank him for his accessibility to discuss my progress as well as the friendly and professional support. His encouraging optimism and trust repeatedly motivated me and finally guided me to finish this work.

Within the GONAF project which he leads, Marco Bohnhoff enabled me to participate in three field trips to the Istanbul area in the frame of the GONAF project, and with his support I was also put in the position to present my work at two international and several national conferences, like AGU, SSA as well as DGG. I am very thankful for these opportunities, during which I made many inspiring and friendly acquaintances that not only put forward my research but also were very rich glimpses into the respective countries and their people.

I thank all my collaborators for the fruitful joint venture which helped me to publish two research papers as main author and one as co-author, Marco Bohnhoff, Václav Vavryčuk, Christina Raub, Patricia Martinéz-Garzón, Ludger Küpperkoch as well as Dorina Domigal. I thank Václav Vavryčuk for his invitation to the Institute of Geophysics of the Czech Academy of Sciences in Prague as well as Ludger Küperkoch for inviting me to the Bestec GmbH in Landau. Many thanks go to Filiz Tuba Kadirioğlu, Recai Kartal and Kenan Yanık from AFAD and Claudius Marx for preparing waveform recordings and to Birsen Can from KOERI for visiting me and sharing data and her expertise. I also thank Michèle Ickrath, Felix Schneider, Fatih Bulut, Eva Stierle, Christina Raub and Ludger Küperkoch, for helping me to get a grasp on some of the seismologist's tools – a new field to me at the time. Christina Raub, Bita Najdahmadi, Diğdem Acarel, Claudius Marx and Joachim Schweitzer are thanked for their readiness to help me out with minor and major software and coding issues.

I thank the DFG, GFZ and the Freie Universität for financial support. I was very glad to recently be involved with Fastloc GmbH and I thank Georg Dresen, Gregorz Kwiatek and Felix Blümle for their shared expertise, trust and friendly cooperation. I also thank Rita Hamlischer for facilitating all my journeys, the travel expense accounting and the working contracts as well as the hot wire to the IT-department. I thank all the members of section 4.2 for many lively discussions and the amicable atmosphere in which we conducted them, I was very happy to share offices with Maike Schäbitz, Vanessa Helpa and Manuel

Kienast as well as Roman Rahner and Marc Rück and most recently with Felix Blümle and Chanpeng Yu and I enjoyed with great pleasure discussions with other members of GFZ, Philippe Jousset, Christian Sippl, Sophia Kufner, Sebastian Specht, Peter Evans and Tuna Eken.

I thank the Helmholtz Association and the PhD representatives for organizing several interesting events, lectures and seminars during which I was able to learn many different facades of contemporary (earth) science. I thank them members of the fellowships to the plate boundary observatory of the North Anatolian Fault for their shared expertise, thorough looks into the blind spot and onto the map as well as a cordial hospitality, Peter Malin, Marco Bohnhoff, Bita Najdahmadi, Patricia Martinéz-Garzón, Stephan Bentz, Diğdem Acarel, Kubra Hocaoğlu and Wade Johnson as well as Recai Kartal, Filiz Tuba Kadirioğlu, Taylan Türkmen and Murat Nurlu from AFAD.

I am thankful to my friends who encouraged me during my work with kind as well as critical words, stories and well wishes, especially Lars Houpt who once forwarded me the position announcement leading me to this venture. I am also very grateful for the wise advice from Jonas Lähnemann and Bita Najdahmadi when sectioning this thesis and thankful to Bita Najdahmadi, Felix Blümle, Alison Singer, Octavio Espinosa and Karl Wollin for proofreading its newly written parts.

Special thanks go to my family, my beloved partner Alison Singer and our children Evelyn, Annie and Maren as well as to my parents Karl and Lucia Wollin and my brother Raimund and sister Johanna. Your patience with this work has been beyond endurance. Your love propelled my advancement. I would like to be an oak tree always, but instead I very often feel like an owl during the day time. I am looking forward to where we will grow or fly from here.

Curriculum Vitae

For reasons of data protection, the curriculum vitae is not included in the online version of the dissertation.

For reasons of data protection, the curriculum vitae is not included in the online version of the dissertation.

For reasons of data protection, the curriculum vitae is not included in the online version of the dissertation.